UNIVERSIDADE ESTADUAL PAULISTA
Faculdade de Ciências e Tecnologia
Campus de Presidente Prudente

RAQUEL ALVES DE OLIVEIRA

GENERATION OF HYPERSPECTRAL DIGITAL SURFACE MODEL IN FOREST AREAS USING HYPERSPECTRAL 2D FRAME CAMERA ONBOARD RPAS

PRESIDENTE PRUDENTE
2017

RAQUEL ALVES DE OLIVEIRA

GERAÇÃO DE MODELO DIGITAL DE SUPERFÍCIE HIPERESPECTRAL, EM ÁREAS DE FLORESTA UTILIZANDO CÂMARA HIPERESPECTRAL DE QUADRO EMBARCADA EM VANT

Doctoral dissertation presented to the Post Graduate Program in Cartographic Sciences, Faculty of Science and Technology, São Paulo State University, for the partial fulfillment of the requirements for the grade of Doctor of Sciences.

Advisor: Prof. Dr. Antonio Maria Garcia Tommaselli.
Coadvisor: Eija Honkavaara

PRESIDENTE PRUDENTE
2017

FICHA CATALOGRÁFICA

Oliveira, Raquel Alves de.
O51d Generation of hyperspectral digital surface model in forest areas using hyperspectral 2D frame camera onboard RPAS / Raquel Alves de Oliveira. - Presidente Prudente : [s.n], 2017
157 f. : il.

Orientador: Antonio Maria Garcia Tommaselli
Coorientadora: Eija Honkavaara
Tese (doutorado) - Universidade Estadual Paulista, Faculdade de Ciências e Tecnologia
Inclui bibliografia

1. Correspondência de imagens 2. Modelo digital de superfície hiperespectral. 3. câmara hiperespectral de quadro. 4. nuvem de pontos de floresta. I. Tommaselli, Antonio Maria Garcia. II. Honkavaara, Eija. III. Universidade Estadual Paulista. Faculdade de Ciências e Tecnologia. IV. Título.

unesp

UNIVERSIDADE ESTADUAL PAULISTA

Câmpus de Presidente Prudente

CERTIFICADO DE APROVAÇÃO

TÍTULO DA TESE: Generation of hyperspectral Digital Surface Model for forest areas with hyperspectral 2D frame camera on-board RPAS

AUTORA: RAQUEL ALVES DE OLIVEIRA
ORIENTADOR: ANTONIO MARIA GARCIA TOMMASELLI
COORIENTADORA: EIJA HONKAVAARA

Aprovada como parte das exigências para obtenção do Título de Doutora em CIÊNCIAS CARTOGRÁFICAS, área: AQUISIÇÃO, ANÁLISE E REPRESENTAÇÃO DE INFORMAÇOES ESPACIAIS pela Comissão Examinadora:

Prof. Dr. ANTONIO MARIA GARCIA TOMMASELLI
Departamento de Cartografia / Faculdade de Ciencias e Tecnologia de Presidente Prudente

Prof. Dr. JORGE ANTONIO SILVA CENTENO
Departamento de Geomática / Universidade Federal do Paraná

Prof. Dr. VERALDO LIESENBERG
Centro de Ciências Agroveterinárias / Universidade do Estado de Santa Catarina

Prof. Dr. MAURICIO GALO
Departamento de Cartografia / Faculdade de Ciencias e Tecnologia de Presidente Prudente

Prof. Dr. ALUIR PORFIRIO DAL POZ
Departamento de Cartografia / Faculdade de Ciencias e Tecnologia de Presidente Prudente

Dra. EIJA HONKAVAARA
Finnish Geospatial Research Institute / Finnish Geospatial Research Institute

Presidente Prudente, 29 de junho de 2017

To my parents, Cleide and José Roberto, and my brother, Rafael.

ACKNOWLEDGMENTS

I would like to acknowledge the financial support of FAPESP (Fundação de Amparo à Pesquisa do Estado de São Paulo - grant 2013/14444-0 and 2014/24844-6) and CAPES (Coordenadoria de Aperfeiçoamento de Pessoal de Nível Superior). I would like to thank the PPGCC and UNESP, for all the support and infrastructure to the development of this research.

I would like to acknowledge the Finnish Geospatial Research Institute (FGI) and to all members of FGI for receiving me during one year and collaborate with my research. In special, I sincerely thank Eija Honkavaara, my co-supervisior, who gave me valuable scietific contribution and support during my internship in Finland and after.

I would like to thank my supervisior, Antonio Tommaselli, for providing me support to develop my scientific interests and undertake this reaserch.

I am also thankful to my research group, in particular, Adilson, Mariana, Gabriela, Marcus and Prof. Imai, who helped in data collection and processing.

I would like to express my sincere gratitude to all of my family, relatives and friends, and my boyfriend, Roope. Without their support and help I would never find courage to overcome the difficulties during this work.

Thank you!

ABSTRACT

Recently, miniaturized hyperspectral sensors, operable from small Remotely Piloted Aerial Systems (RPAS), have entered the market and some of these sensors acquire hyperspectral bands in frame geometry. Images of the lightweight hyperspectral 2D frame camera can be used to generate high-resolution hyperspectral digital surface models (HDSMs), without the registration of data from different sensors or different dates of acquisition. HSDMs increase the knowledge about the targets since it allows modeling the target reflectance using data coming from different directions. In this study, the hyperspectral 2D frame camera used does not acquire all bands instantaneously, causing band misalignment due to the platform motion. The main aims of this project were to study and develop techniques for the generation of HDSMs in forest areas, studying and assessing the main steps to process the hyperspectral 2D frame camera images until the HDSM generation. Considering that the camera technology is based on tunable filters, the study have assessed the orientation and DSM generation steps: the self-calibrating bundle adjustment to verify the behaviour of the interior orientation parameters using different spectral bands; the co-registration of the bands using 2D geometric transformation; the exterior orientation parameter estimation. Regarding to the DSM generation, an approach based on object space image matching was developed, adapting the vertical line locus (VLL) method for HDSM generation, and was named as hyperspectral VLL (HVLL). Additionally, the use of image classification data was investigated in order to adapt the image matching parameters and improve the process of image matching for different objects (hyperspectral VLL classes - HVLLC). Further, multiple bands were used and the spectral and multiangular viewing geometry were computed simultaneously to the image matching method. Quality assessment was performed by comparing to DSMs generated to those produced by commercial software and also by Airborne Laser Scanning (ALS) data. This investigation demonstrated that the proposed technique can be used to generate integrated 3D information and multiangular hyperspectral data from hyperspectral 2D frame camera. The assessment of all steps showed that the hyperspectral 2D frame technology can provide accurate geometric and spectral data and the resulting HDSMs have potential for several remote sensing applications.

Keywords: image matching, hyperspectral digital surface model, hyperspectral frame camera, forest point cloud.

RESUMO

Recentemente, os sensores hiperespectrais miniaturizados entraram no mercado e alguns modelos adquirem bandas hiperespectrais com geometria de quadro, com a vantagem de serem também operados em veículos aéreos remotamente pilotados (VARP). As imagens deste tipo de câmara podem ser utilizadas para a geração de modelos digitais de superfície hiperespectral (MDSHs) de alta resolução, usando o VARP, sem a necessidade do registro de dados de diferentes sensores ou diferente datas de aquisição. MDSHs aumentam o conhecimento sobre os alvos, uma vez que permitem modelar a reflectância do alvo utilizando dados provenientes de diferentes direções. Neste trabalho, a câmara hiperespectral de quadro utilizada não adquire todas as bandas instantaneamente, causando um deslocamento entre as bandas devido ao movimento da plataforma. Os principais objetivos deste projeto foram estudar e desenvolver técnicas para a geração de MDSHs em áreas de florestas, investigando e avaliando as principais etapas para o processamento das imagens da câmara hiperespectral de quadro até a geração do MSDH. Considerando que a tecnologia da câmara baseia-se em filtros ajustáveis, o estudo avaliou: a auto-calibração da câmara, verificando o comportamento dos parâmetros de orientação interior em diferentes bandas espectrais; o corregistro das bandas através de transformações geométricas 2D; e a estimativa dos parâmetros de orientação exterior. Em relação à geração do MDS, uma abordagem baseada em correspondência de imagem no espaço do objeto foi desenvolvida, adaptando o método de busca em linha vertical (VLL) para a geração MDSH e foi nomeado como VLL hiperespectral (HVLL). Adicionalmente, o uso de imagens classificadas para a adaptação dos parâmetros de correspondência foi avaliado com o objetivo de melhorar o processo de correspondência para diferentes objetos (HVLLC). Posteriormente, foram utilizadas múltiplas bandas no processo de correspondência de imagens, dados como múltiplos ângulos de visada e informação espectral foram calculados simultaneamente ao processo de correspondência de imagens. A avaliação da qualidade foi realizada comparando-se os MDSs gerados com os produzidos por um software comercial e por dados *Airborne Laser Scanning* (ALS). Esta investigação demonstrou que a técnica proposta pode ser usada para a geração de modelos 3D integrados aos dados hiperespectrais multiangulares da câmara hiperespectral de quadro. A avaliação de todas as etapas demonstrou que esta tecnologia pode fornecer dados geométricos e espectrais precisos e os MDSHs resultantes possuem potencial para várias aplicações de sensoriamento remoto.

Palavras-chave: correspondência de imagens, modelo digital de superfície hiperespectral, câmara hiperespectral de quadro, nuvem de pontos de floresta.

LIST OF FIGURES

LIST OF TABLES

LIST OF ABREVIATIONS AND ACRONOMYS

ABM: Area-based matching

AKA: Academy of Finland

ALS: Airborne Laser Scanning

AOTFs: Acousto-Optic Tuneable Filters

ASIFT: Affine-SIFT

ASPRS: American Society for Photogrammetry and Remote Sensing

AVIRIS: Airborne Visible Infra-Red Imaging Spectrometer

BBA: Bundle Block Adjustment

BGCC: Band Global Correlation Coefficient

BRDF: Bidirectional Reflection Distribution Function

BRF: Bidirectional Reflectance Function

CCD: Charge-Coupled Device

CHM: Canopy Height Model

CMC: Calibration with Multiple Cameras

CMOS: Complimentary Metal-Oxide Semiconductor

C-SIFT: Colored-SIFT

DBH: Diameter at Breast Height

DEM: Digital Elevation Model

DN: Digital Number

DoG: Difference-of-Gaussian

DSM: Digital Surface Model

DTM: Digital Terrain Model

EOP: Exterior Orientation Parameters

ESEC MLP: Estação Ecológica Mico Leão Preto

FBM: Feature Based Matching

FP: Fabry-Pérot

FPGA: Field Programmable Gate Array

FPI: Fabry-Pérot Interferometer

FWHM: Full Width at Half Maximum

GCC: Global Correlation Coefficient

GCP: Ground Control Point

GNSS: Global Navigation Satellite Systems

GPS: Global Positioning System

GPU: Graphics Processing Unit

GSD: Ground Sampling Distance

HDSM: Hyperspectral Digital Surface Model

HFC: Hyperspectral 2D Frame Camera

HRV: High Resolution Visible

HSI: Hue, Saturation and Intensity

IMU: Inertial Measurement Unit

INS: Inertial Navigation System

IOP: Interior Orientation Parameters

ISO: Integrated Sensor Orientation

ISPRS: International Society for Photogrammetry and Remote Sensing

LASER: Light Amplification by Simulated Emission of Radiation

LCTFs: Liquid Crystal Tuneable Filters

LiDAR: Light Detection And Ranging

LSM: Least Squares Matching

MPGC: MultiPhoto Geometrically Constrained Matching

MSS: Landsat Multispectral Scanner

NIR: Near InfraRed

OJC: On-the Job Calibration

PC: Perspective Centre

RADAR: RAdio Detection And Ranging

RANSAC: Random Sample Consensus

RBMC: Rede Brasileira de Monitoramento Contínuo dos Sistemas GNSS

RGB: Red, Green, Blue bands

RMSE: Root Mean Square Error

RPAS: Remotely Piloted Aerial Systems

SAM: Spectral Angle Mapper

SCM: Spectral Correlation Mapper

SfM: Structure from Motion

SGM: Semi-Global Matching

SIFT: Scale Invariant Feature Transform operator

SSD: Sum of Squared Differences

SURF: Speeded Up Robust Features

TIN: Triangulated Irregular Network

UAV: Unmanned Aerial Vehicle

UAV-4D-BIO: Unmanned Airborne Vehicle-based 4D Remote Sensing for Mapping Rain Forest Biodiversity and its Change in Brazil

UPTK: Unesp Photogrammetric ToolKit

VLL: Vertical Line Locus

ZROT: Zero Rotation

CONTENT

1. INTRODUCTION

Vegetation is one of the most important components of ecosystems, since it covers approximately 70% of the continental earth's surface. In Brazil, the Atlantic Forest has one of the highest levels of species richness and endemism rates on the planet, but biome that has suffered the greatest loss of forest (BARBOSA et al., 2014). Information about types of plant species, their form, structure, distribution and phenology, can provide important insights for the monitoring and knowledge of the climatic, geological and topographic characteristics of the forest (BERGEN et al. 2009).

Hyperspectral imaging is a very powerful technology for vegetation applications (CLARK et al., 2005; GOETZ, 2009). Hyperspectral data gives detailed spectral information for each image pixel, and this information can be correlated with quantitative parameters that characterize the targets. Extraction of the biophysical parameters of vegetation from canopies (JACQUEMOUD et al., 1995; HABOUDANE et al., 2004; CLARK et al., 2011) and forest species classification (CLARK et al., 2005; NEVALAINE et al., 2017) are examples of the potential uses of hyperspectral data.

A 3D model of the forest areas is another complementary data for several forestry applications, such as estimating forest biomass and volume (BERGEN et al. 2009). The 3D data can be acquired using laser scanning data (NAESSET, 1997; HYYPÄ et al., 2012; VAUHKONEN et al., 2016), Interferometric Synthetic Aperture Radar (InSAR) (RABUS, et al., 2003; PEDUZZI et al., 2012; SADEGHI, et al. 2016), stereoscopic interactive measurement or by photogrammetric techniques using image matching (BALTSAVIAS, et al. 2008; GUEN, 2012 HAALA and ROTHERMEL, 2012; OLIVEIRA et al., 2015). Many studies use airborne laser scanning (ALS) data to derive forest point clouds, due to the feasibility of also acquiring height data from below the canopy (HYYPPÄ, 2008, KANKARE et al., 2012). Photogrammetric methods using optical images can provide both 3D information with high density and texture data, but it cannot penetrate under the canopy. Generally, the extraction of 3D geometric information from optical images is performed using image matching methods. These

methods can be classified as feature-based (LOWE, 2004), area-based (GRUEN, 1985; GRUEN; STALLMANN, 1993; ZHANG, 2005a) or global methods (BIRCHFIELD and TOMASI, 1999; SCHARSTEIN and SZELISKI, 2002; HIRSCHMÜLLER, 2005). In the last two decades, image matching methods have advanced tremendously through technological innovation, computational power and improvements of photogrammetric and computer vision algorithms (HAALA, 2009; RUBLEE et al., 2011; HIRSCHMMÜLLER; BUDER; ERNST, 2012). Recently, low-cost tools for photogrammetric surveys and remote sensing using remotely piloted aerial systems (RPAS), also known as unmanned airborne vehicles (UAVs) or Drones, have emerged and increased interest in the use of image matching techniques to generate digital surface models (DSMs) in vegetation areas for monitoring, inventory or estimation of forest parameters.

Commonly, images with three wide bandwidth bands in red, green, blue (RGB) and/or near-infrared spectral regions are used in photogrammetric processes. However, hyperspectral imaging technology have emerged new sensors and widened the potential of their applications (GOETZ, 2009; SHAW and BURKE, 2003; HONKAVAARA et al., 2013). Traditional hyperspectral imaging sensors are built with linear sensors (pushbroom) or point (whiskbroom) scanning technologies, which are effective when considering stable platforms (aerial or orbital). RPAS are dynamic platforms, thus a pushbroom or whiskbroom sensor, onboard on it, would require a more precise inertial navigation system. Vision based orientation technologies have also emerged (BÜTTNER and RÖSER, 2014), since then, miniaturized pushbroom hyperspectral sensors have recently been developed and implemented in RPAS (BÜTTNER; RÖSER, 2014; SUOMALAINEN et al., 2014). This requires more studies for a better use.

Another class of lightweight hyperspectral camera has also emerged, the hyperspectral 2D frame cameras. A spectral 2D frame cameras employ mosaic filters or tunable filter technologies to record spectral data in a 2D frame format geometry (similar to traditional RGB frame cameras). The Rikola Hyperspectral Camera (SENOP, 2017), the Cubert UHD 185-Firefly (CUBERT, 2017), or the IMEC SM5X5 (IMEC, 2017) are examples of this type of sensors. Hyperspectral 2D frame cameras can be classified according to their image acquisition system, which can collect registered or unregistered bands (AASEN et al., 2015). Unregistered camera systems, such as the Rikola Hyperspectral Camera, based on the tuneable Fabry-Pérot Interferometer (FPI) (SENOP, 2017), acquire bands time sequence mode. Registered

camera systems use sensors with mosaic filters, which reduce the spatial resolution, and each full resolution band is obtained by applying a demosaicking process. The Cubert UHD 185-Firefly (Cubert, 2017) and the IMEC SM5X5 (Imec, 2017) sensors are examples of this approach. Hyperspectral 2D frame cameras allow an object to be imaged from different viewing angles, generating overlapping hyperspectral cubes. Studies have evidenced that the radiometric and geometric quality of hyperspectral 2D frame cameras are suited to photogrammetric and Remote Sensing applications (HONKAVAARA et al., 2013; AASEN et al., 2015). In addition, RPAS show a great potential especially for applications that require rapid survey or frequent repetitions for temporal analyses of a phenomena (COLOMINA and MOLINA, 2014).

1.1 Motivation of this study

Using new sensors requires experimental studies and assessments and new processing chains. In the case of tuneable hyperspectral 2D frame cameras, the acquisition of images along each cube is performed using a complex and tuneable mechanism. In dense tropical forest, this is rather critical because of the difficulties to find gaps and fit visible ground control points (GCPs) for the photogrammetric process. Therefore, in order to perform accurate 3D measurements using stereoscopic images, the interior geometry of the camera (the interior orientation parameters, IOPs) and the exterior orientation parameters (EOPs) must be assessed.

In the previous studies, the integration of hyperspectral and 3D data has been performed based on feature extraction methods followed by the estimation of 2D transformation parameters between different resolution airborne hyperspectral images and airborne laser scanning (ALS) DSM (DALPONTE et al., 2008; AVBELJ et al., 2015). Another method to integrate spectral and 3D information has been the use of dual or multi-wavelength laser scanning systems, using separate monochromatic laser sources, thus producing limited number of nonregistered spectral point clouds (WEI et al., 2012; MATIKAINEN et al., 2017). Using only passive sensors, spectral images from miniaturized hyperspectral pushbroom (SUOMALAINEN et al., 2014) and 2D frame sensors (NÄSI et al., 2015; NEVALAINEN et al., 2017) have been combined to DSMs generated from RGB images collected during the same flight based on accurate 3D registration process. Despite promising results, the use of data from different sensors, platforms, and/or different times can lead to geometric inaccuracies, difficult

interpretation and wrong association of spectral information to points, which may distorts the target and inferences.

Significant improvements in the technology for capturing geometric and spectral information have been achieved with the development of terrestrial hyperspectral laser scanner (NEVALAINEN et al., 2014; HAKALA et al., 2015) and the hyperspectral 2D frame sensors. Using these technologies, the generation of 3D information integrated with spectral data for each point can be achieved directly from the same sensor. Currently, hyperspectral LiDAR systems are still laboratory-based prototypes and not practical for manned or unmanned flight campaigns. Alternatively, collecting 3D and hyperspectral data by 2D frame cameras is a simple and cost-effective technique. The generation of 3D properly associated with multiangular spectral information directly from hyperspectral images is a topic of interest and open to developments, due the potential such a data in several applications of environmental and agriculture (AASEN et al., 2015, 2012; NEVALAINEN et al. 2017). Existing software packages are not integrating the full spectral data provided by hyperspectral 2D frame cameras into the DSM algorithm and the viewing angle geometry. These integration have been achieved in separated process and software (AASEN et al., 2015; ROOSJEN et al., 2017).

In this context, this study focuses on a technique in which a 2D frame-format hyperspectral sensor is used as a data source for the generation of spectral DSMs, which will be called as hyperspectral digital surface model (HDSM), in dense forested areas. Additionally, this study proposes the use of hyperspectral image classification data to optimize the tuning of the image matching parameters for different classes in an object space-based multi-image matching approach.

1.2 The project UAV-4D-Bio

This doctoral project (FAPESP grant nº 2013/17787-3) is connected to the international project n° 2013/50426-4, entitled “Unmanned Airborne Vehicle-based 4D Remote Sensing for Mapping Rain Forest Biodiversity and its Change in Brazil” (UAV-4D-BIO), jointly funded by FAPESP and the Academy of Finland (AKA). The objective of UAV-4D-BIO is to develop technologies for biodiversity and its change mapping, using UAV as the sensor platform, complete object models, consisting of hyperspectral, 3D geometry and Bidirectional Reflectance Function (BRF) response as features, and time series of complete object models to reveal changes in time to be used

for biodiversity mapping and for developing indicators of environmental change. The methodology is being used in Finland in Evo test forests and in regeneration areas of Atlantic Forest within São Paulo State.

The focus of this doctorate project is concerned with the study and development of an automatic method for generation of DSM, connected with spectral information, in areas of Boreal and Atlantic forests, complying with part of the UAV-4D-BIO objectives.

1.3 Objectives

The general objective is to study, develop, implement and evaluate techniques for the generation of hyperspectral digital surface model (HDSMs) in vegetated areas, using hyperspectral images acquired by a 2D frame camera based on Fabry Perót interferometer (FPI), carried by RPAS. This camera will be referred in this manuscript as FPI camera. The main objective is achieved by carrying out the following tasks:

- To estimate and analyze the behavior of the IOPs of the hyperspectral 2D frame camera and to assess the feasibility of calibrating the hyperspectral 2D frame FPI camera using the self-calibrating bundle adjustment with the Conrad-Brown model for the IOPs;
- To study and assess the registration between the bands of hyperspectral cubes (acquired with the FPI camera) by 2D transformation function;
- Assessment of the EOPs estimation with techniques either direct or integrated;
- To study and develop techniques related to the association of the hyperspectral images classification to the process of image matching;
- To study and develop techniques for integrating spectral information to the DSM.

1.4 Structure of the thesis

This thesis is organized in eight chapters. Chapter 1 gives an introduction of the theme, covering the issues, motivation and the objectives of this research. Chapter 2 presents the theoretical basis necessary to the development of each step of this work,

covering sensor modeling, image registration and georeferencing and the concepts of image matching and DSM generation by integrating spectral information simultaneously. The study areas used are shown in Chapter 3.

As the sensor used in this research acquires image bands in a sequential mode, the Chapter 4 is concerned to the evaluation of band co-registration using 2D transformation functions and drawbacks of this approach compared to other methods. The sensor interior orientation and assessment is discussed in detail in Chapter 5. Chapter 6 shows the different activities developed in the field work campaigns and the external orientation of the image blocks in two different forest scenarios.

Chapter 7 comprises the description and results of the proposed method, hyperspectral VLL (HVLL), to generate a DSM with multiangular geometry and the hyperspectral information. The method is based on dense multi image matching techniques, using hyperspectral 2D frame camera. The method was structured as follows: definition of the search space; determination of the correspondences; identification of viewing geometry and spectral data and generation of the HDSM. Additionally, the use of image classification information to guide the matching process was proposed and evaluated. Experiments were carried out over two study areas of different forest. Moreover, the assessments, discussions and potential of the method are showed in the Chapter 7.

It is worth noting that Chapters 4, 5, 6 and 7 present an overview and in troduction about the objective, data and methods used in the investigation, followed by results, discussion and conclusions.

Finally, Chapter 8 presents the overall conclusions about all studies and results obtained in this research. This chapter concludes with recommendations for future works.

1.5 Contribution of this doctoral dissertation

DSMs can be derived directly from high resolution hyperspectral 2D frame images, since the frame cameras can provide multiple records of the object from different viewing directions, offering the possibility of obtaining redundant stereoscopic measurements and analysing the multidirectional reflectivity characteristics (HONKAVAARA et al., 2013; AASEN et al., 2015).

Studies using multispectral orbital images (ASNER, 2000; LIESENBERG et al., 2007) and RGB-NIR aerial frame camera (KOUKAL and ATZBERGER, 2012; KORPELA et al., 2014) have showed that observations from multiple viewing angles significantly contribute to the assessment of the vegetation structure (KOUKAL and ATZBERGER, 2012; KORPELA et al., 2014). Additionally, the combination of hyperspectral image data and 3D information, from ALS data (DALPONTE et al., 2008; ALONZO et al., 2014; AVBELJ et al., 2015; HAKALA et al., 2015) or from photogrammetric process applied in RGB images (NEVALAINEN et al., 2017) has improved the quality of inferences about the objects in remote sensing applications. However, the registration of data obtained from different sensors and date of acquisition can present errors of alignment.

The integration of spectral data from hyperspectral 2D camera and 3D information have been accomplished by Aasen et al. (2015), using a hyperspectral 2D camera with registered bands and by Roosjen et al. (2017), using a model of the FPI camera. Both authors used a commercial software to generate and export DSM and orthorectified cubes and other tools to link the 3D data generated to the spectral information separated. The lack of information about the software packages models can also cause imperfections of spectral information association with the 3D data.

This study provides new rigorous methodology for generation of the HDSM, contributing to the development of techniques to spread the use of hyperspectral 2D frame sensors in Remote Sensing applications. In the area of DSM generation, the work has showed a method of using reference classes from the hyperspectral image classification in order to improve the tuning of image matching parameter values. The method using pixels image classification information helped to increase the number of points in areas of forest gaps, which can improve the quality of DTM extraction from DSMs. The points were labeled by the classes, which can be used as initial classification of the photogrammetric DSM. The information of gaps location in forest can be used in vegetation analyses (KOUKOULAS and BLACKBUM, 2004; GETZIN et al., 2014).

The well-known Vertical Line Locus (VLL) method, which is an object space-based matching strategy, was adapted to be used with the reference classes. Traditional techniques to improve the quality of area-based matching methods, such as adaptive windows size and shape (KANADE and OKUTOMI, 1991; ZHANG, 2005a) and window rectification (GRUEN, 1985; PAPARODITIS et al., 2002) were also

incorporated in the steps of the method. Object space-based method can be considered simpler than image space based algorithms, since the point's 3D coordinates are directly obtained without disparity map fusion and point cloud merging steps.

In addition, a rigorous study of the FPI camera IOPs was performed using traditional photogrammetric approaches. Due to the difficulty of accessing inside dense tropical forests, the planned flights will be long lines (blocks with one to two strips) and without a homogenous distribution of control points over the image blocks. Therefore, the exterior orientation step of the photogrammetric blocks was also assessed.

2. BACKGROUND

This study involves the use of a new trend in Remote Sensing and Photogrammetric data, the HDSM, which can be generated using a novel technology of hyperspectral sensors, the lightweight hyperspectral 2D frame cameras. The image acquisition with hyperspectral cameras based on FPI technology is achieved in a time-sequential way, which results in bands with different position and orientations. When generating an HDSM, recovering the spectral information for each ground point requires very well coregistered spectral bands. The photogrammetric geometric process is responsible for the accurate projection of the points to the proper pixel along the bands of the hyperspectral cube, through the collinearity equations. Consequently, the study and assessment of the photogrammetric geometric procedures, used to estimate the parameters involved in the HDSM generation, are essential for the quality of this product. In this study, the photogrammetric geometric procedures involved were: the camera calibration, band registration using 2D mapping functions, estimation of the EOPs and the DSM generation using dense image matching techniques.

Thus, this chapter presents major theoretical topics of the photogrammetric processing chain in the proposed method.

2.1 Image acquisition and sensors

2.1.1 Spectral sensor and images

Optical remote sensing systems can be classified according to the number of spectral bands collected from the reflected energy, emitted or backscattered from a given object (JENSEN, 2009). Panchromatic imaging systems have detectors sensitive to radiation within a relatively broad spectral range (usually in the visible region). Multispectral imaging systems have more than one detector channel covering moderate-width spectral bands. Goetz et al. (1985) defined hyperspectral remote sensing systems

as sensors capable of recording hundreds of contiguous spectral bands. Later, Goetz (2009) states that this definition remains, but emphasized that, in comparison with the quantity of spectral bands, the adjacency condition between the spectral bands is more important.

In general, the remote sensing systems for image acquisition have the following formats (SCHOWENGERDT, 2006; JENSEN, 2009):

- ✓ Whiskbroom scanners have a number of detectors aligned linearly in the direction of the platform movement and a mirror that oscillates from side to side by scanning the earth's surface orthogonally in the direction of motion. Examples: Landsat Multispectral Scanner (MSS) and the Airborne Visible Infra-Red Imaging Spectrometer (AVIRIS) of the NASA Jet Propulsion Laboratory (VANE et al., 1993)
- ✓ Linear scanning sensors (pushbroom) have several detectors linearly aligned perpendicular to the direction of the platform movement and the image is formed by the displacement of the platform. Examples: High Resolution Visible (HRV) sensors of SPOT satellites 1, 2 and 3 and the AISA series of airborne and RPAS imaging spectrometers by Specim Ltd (www.specim.fi);
- ✓ Frame sensors have detector elements arranged two-dimensionally and the image is formed in a single instant.

Most hyperspectral imaging sensors used in remote sensing have been based on pushbroom or whiskbroom scanning and mounted on manned airborne (for example, CASI)or satellite platforms (for example, HYPERION). Recently, miniaturized hyperspectral 2D frame sensors have become available, and these stand out because of their performance and the large number of uses to which they can be applied, such as agriculture, environmental monitoring (HONKAVAARA et al., 2013; AASEN et al., 2015; NÄSI et al., 2015; ZHENG et al., 2016). The Cubert UHD 185-Firefly (CUBERT, 2017), the Rikola FPI (RIKOLA, 2017) and the IMEC SM5X5, are examples of camera systems to record hyperspectral information with two spatial dimensions (frame geometry). These new sensors can be transported by RPAS platforms. RPAS have been used in Remote Sensing and Photogrammetric applications in the recent years (COLOMINA; MOLINA, 2014). RPAS have an advantage in temporal analyses since initialization costs of RPAS campaigns are typically lower than those of manned aircrafts. The disadvantages, especially in low cost RPAS, are the operation time, weight limitations and payload size supported, requiring lighter and

smaller sensors. This implies, at present, in images with lower resolution, a greater number of images to cover an area and information and limitations in the devices for direct georeferencing.

Hyperspectral 2D frame imagers that are based on tuneable filter technologies including, for instance, acousto-optic tuneable filters (AOTFs), liquid crystal tuneable filters (LCTFs) (Gupta, 2008; Lapray et al., 2014), mosaic filters (CUBERT, 2017) or Fabry-Pérot (FP) tuneable filters, can acquire a 2D spatial image, and the spectral dimension is acquired as a function of time. The rigid frame geometry is particularly important for cameras mounted on less stable platforms, such as small RPAS. In addition, multiple records of the object can be acquired from different viewing directions, offering the possibility of obtaining stereoscopic measurements and analysing multidirectional reflectivity characteristics (HONKAVAARA et al., 2013; PINTO et al., 2017; ROOSJEN et al., 2017).

2.1.2 FPI CAMERA

The VTT Technical Research Centre of Finland has developed a lightweight hyperspectral 2D frame camera based on the FPI technology, which has been commercialized by the Finnish company, Rikola. A FPI consists of two partially reflective surfaces positioned parallel to each other. The length of the optical path of the cavity formed between these reflective surfaces (the gap) determines the wavelengths that can be transmitted through the interferometer. This is because the light rays passing through the surfaces undergo different multiple reflections according to the gap length (MÄKYNEN et al., 2011). Different wavelengths can be acquired by modifying this gap, making it possible to reconstruct the spectrum for each pixel in the image (SAARI et al., 2009; MÄKYNEN et al., 2011). The FPI camera can be carried by an RPAS and satisfies the requirements of several applications (SAARI et al., 2009; HONKAVAARA et al., 2013).

FPI camera has been built using two different sensor configurations. First models had a CMOS sensor with Bayer mosaic filter with three channels (RGB), allowing to acquire up to three bands at the same time, with single airgap value. An example of this model is the FPI2012b camera model (prototype) shown in Figure 1 (a). In the commercial models, such as the FPI2014 model (Figure 1 (b)), two single-color CMOS sensors (no Bayer filter) and a beam splitting component are used. In this case, each

sensor is responsible for a particular range of the spectrum, with only one channel to receive energy: one of the sensors has been optimised to record the visible bands (500–636 nm), while the other sensor has been optimised for recording the visible and NIR (VNIR) bands (650–900 nm). In the camera internal system, the distance between the interferometer plates is controlled by capacitive electrodes and piezoelectric actuators. The light beam from the object passes through low-pass filters and high-pass filters to the lens, which focuses the light onto the piezo-FPI module, reaching an array sensor (Figure 1 (c) and (d)).

The bands of the hyperspectral data cubes obtained with the FPI camera can be configured by the user according to the spectral range and resolution limits of the camera. The image size can be selected as 2048 x 2048 pixels or 1024 x 648 pixels

As a result of the spectral bands acquisition process in the FPI cameras, the spectral bands of a cube do not overlap perfectly when the camera platform is moving. Due to this feature, each spectral band in same cube exposed to a different air gap value has a different position and attitude, which needs to be considered in the post-processing steps. The resulting data cubes can be seen as a set of sequential bands or, as Aasen et al., (2015) has called, a set of bands in an unregistered band package. The integration time is approximately 0.0333 s in the FPI2014 model. Thus, recording a single cube with 25 bands, for instance, takes up to 0.833 s. If the RPAS is flying with a speed of 3.5 m/s and continuous image acquisition, the horizontal displacement of the platform between the first band and the last band is approximately 2.917 m throughout the acquisition of the entire 25 bands. The misalignment between the sensors and eventual attitude variations of the camera during exposure can also affect the displacement of the bands. However, the frame images have more rigid geometry than the pushbroom images, reducing the need for a high-grade inertial measurement unit.

Figure 1: Two FPI hyperspectral camera models: (a) FPI2012b (Honkavaara et al., 2013) and (b) FPI2014, with irradiance sensors and a GPS antenna. The diagrams depict the inner optical systems of the (c) FPI2012b and (d) FPI2014 camera models (Rikola Ltd., 2015).

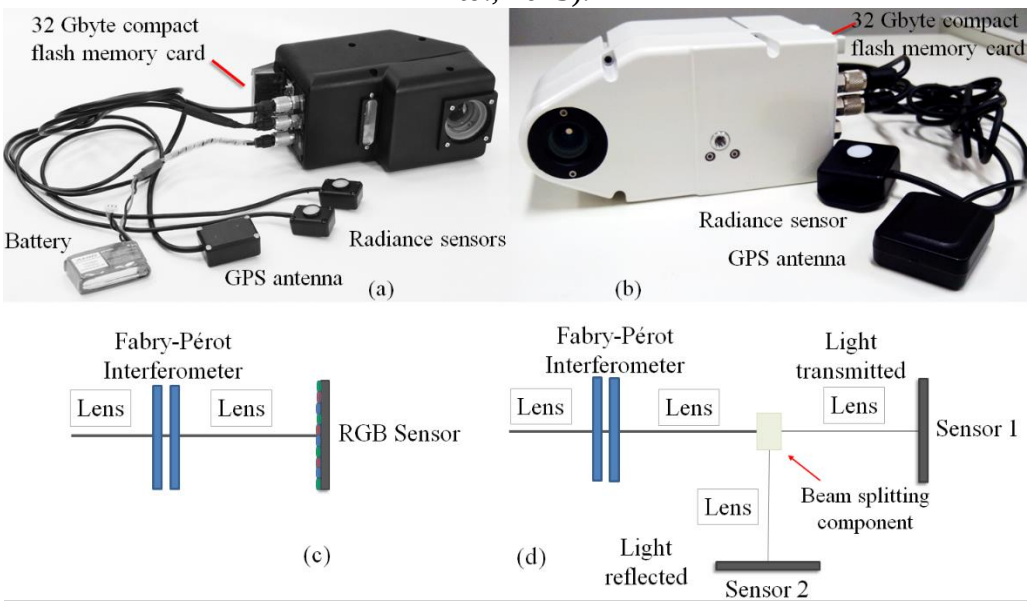

FPI cameras are accompanied by an irradiance sensor and a GPS receiver (single frequency), which records the position and the exact time of the first band of each cube. The irradiance sensor is based on the Intersil ISL29004 photodetector with a spectral sensitivity range of 400-1000 nm. This sensor measures the irradiance during each exposure; because it is not calibrated, relative broadband irradiance intensity values are obtained (HONKAVAARA et al., 2013, 2016). The dark signal is required to be acquired before the starting to acquire the data cubes. Table 1 summarises the main parameters of the FPI2012b and FPI2014 models.

Table 1: Spectral imager specifications for the FPI2012b and FPI2014 models (modified from Honkavaara et al. (2013) and Rikola Ltd (2015)).

Parameter	***FPI2012b***	***FPI2014***
Approximate principal distance	10.9 mm	9 mm
Spectrum	400-900 nm	500-900 nm
Spectral resolution	10 nm, FWHM	10 nm, FWHM
Spectral step	< 1 nm	< 1 nm
F-number	~ 2.8	~ 2.8
Pixel size (Sensor CMV4000)	5.5 x 5.5 µm	5.5 x 5.5 µm.
Sensor size	2048 x 2048 pixels	2048 x 2048 pixels
Image size for maximal spectral resolution	1024 x 648 pixels (2 times binned)	1024 x 1024 pixels
Weight	< 700 g	< 700 g
Dimensions	80 x 92 x 150 mm	75 x 89.5 x 151.5 mm

Due to the camera's peculiar acquisition process, an appropriate calibration design and a suitable analysis of the calibration data are needed. In particular, it is essential to verify and analyze the influence of the variations in the internal elements of the camera (the gap in the interferometer, for instance).

2.2 Image Classification

The classification process has the function of labeling image pixels or objects, using different criteria for the distinction and identification of categories (classes) present in the image. Classes may represent, for instance, soil types, vegetation or buildings (SCHOWENGERDT, 2006). With the identification and classification of homogeneous clusters, it is possible to establish hypotheses about the object or phenomenon under study. Clustering implies grouping pixels in multispectral space. Pixels belonging to a particular cluster are therefore spectrally similar (RICHARDS and JIA, 2006).

Classification methods can be divided as supervised or unsupervised methods and as pixel or region based methods (RICHARDS, 1999; SCHOWENGERDT, 2006). Most of the classifiers perform classification by pixel, which uses only the spectral information of each pixel to find homogeneous regions, using distance measures in multi/hyper-spectral space or probabilities that a pixel belongs to a specific class (MENESES and ALMEIDA, 2012).

Supervised classification requires user iteration for the algorithm training process. The algorithms most used are parallelepiped, minimum distance, mahalanobis distance and maximum likelihood (RICHARDS, 1999; SCHOWENGERDT, 2006). In the unsupervised approach, the user must provide initial parameters and the training is part of the algorithm process. The main non-supervised classification algorithms used in the Remote Sensing community are ISODATA and K-means (RICHARDS, 1999).

Several factors can cause confusion between the spectral signatures of the targets, such as topography, shadows, problems in sensor calibration, and the mixture of target responses (SCHOWENGERDT, 2006; HONKAVAARA et al., 2012b).

Classification processes can be applied to extract only specific classes of interest from the analyst, such as shadow areas. Shadow can cause occlusions in the objects; however, these areas can be treated as a source of geometric and semantic information. Its location can provide clues about the shape and variation of the height of the objects

(POLIDORIO et al., 2003). Considering dense forested areas, a critical factor of the detection and delimitation of trees is the variation of canopy brightness, due to the effect of leaf shadow patterns on the canopy spectral response, which is higher for high-resolution images (KORPELA et al., 2011; HONKAVAARA et al., 2012b).

Spectral Angle Mapper (SAM) is a supervised classification algorithm widely used in the classification of hyperspectral images. SAM compares the similarity between spectra of the image and the reference spectra (KRUSE et al., 1993). Carvalho and Meneses (2000) pointed out some disadvantages found in the SAM similarity metric, such as the impossibility of distinguishing between negative and positive correlations and limitations for some types of curves. Therefore, the authors proposed an adaptation of the SAM, the Spectral Correlation Mapper (SCM). SCM combines Pearson's correlation coefficient, eliminating negative correlation and maintaining the SAM characteristic of minimizing the shadow effect, resulting in better results.

2.3 Geometric processing of frame images

2.3.1 Exterior orientation

Exterior orientation parameters define the position and orientation of the camera at the exposure time, with respect to the coordinate system of the object space. Each image requires six independent parameters, the perspective center coordinates (X_0, Y_0 and Z_0) and the attitude angles (ω, φ, κ) (MIKHAIL et al., 2001). In the case of linear scanning sensors, each line of the scene defines a new beam of rays, with six EOPs.

Image orientations can traditionally be solved via the collinearity model (Equations (1)), in rigorous photogrammetric processing. The estimation of EOPs for single images is called the Space Resection method, and requires at least three non-collinear GCPs. The 3D coordinates of a photogrammetric point in the ground reference system can be determined after estimating the EOPs of at least two images, using the spatial intersection method (MIKHAIL et al., 2001). The collinearity model is given as:

$$\begin{aligned} x - x_0 - \delta x_r - \delta x_d - \delta x_a &= -c\frac{m_{11}(X - X_0) + m_{12}(Y - Y_0) + m_{13}(Z - Z_0)}{m_{31}(X - X_0) + m_{32}(Y - Y_0) + m_{33}(Z - Z_0)} \\ y - y_0 - \delta y_r - \delta y_d - \delta y_a &= -c\frac{m_{21}(X - X_0) + m_{22}(Y - Y_0) + m_{23}(Z - Z_0)}{m_{31}(X - X_0) + m_{32}(Y - Y_0) + m_{33}(Z - Z_0)} \end{aligned} \quad (1)$$

where x and y are the observed image-point coordinates; X, Y and Z are the ground coordinates of the same point; m_{ij} are the elements of the rotation matrix; X_0, Y_0 and Z_0

are the ground coordinates of the camera's perspective centre (PC); x_0 and y_0 are the principal point coordinates; c is the camera's principal distance; δx_r and δy_r are the effects of radial distortion (the coefficients of which are k1, k2, k3); δx_d and δy_d are the effects of decentring lens distortion (P1, P2); and δx_a and δy_a are the effects of affinity error (A, B). The effects of radial and decentring lens distortion have been described by Brown (1971), and affinity effect can be estimated as presented by Habib et al. (2002).

Bundle block adjustment (BBA) is a method largely used in Photogrammetry for the simultaneous orientation of a group of overlapping images, which greatly reduces the number of control points required. The method estimates the image EOPs and the 3D coordinates of photogrammetric points, as well as the accuracy of the least squares optimization. In order to estimate the IOPs of the camera within the adjustment, the procedure requires additional parameters (Section 2.3.2). The BBA can be extended to the Integrated Sensor Orientation (ISO) method, which combines bundle adjustment with more accurate values for EOPs, used as weighted constraints.

EOPs can also be estimated directly using high grade GNSS/inertial system measurements integrated with the imaging sensor (SCHENK, 1999; CRAMER; STALLMANN; HAALA, 2000; CRAMER; STALLMANN, 2001).

A reliable image matching technique to extract photogrammetric points (tie points) is also important. Nowadays, the extraction of points in individual images to be used as tie points by matching can be performed by Feature Based Matching, and one of the most popular techniques of this class is Scale Invariant Feature Transform (SIFT) (LOWE, 2004). Recently, structure from motion (SfM) algorithms have been widely used to estimate the EOPs of images collected with RPAS (ELTNER; SCHNEIDER, 2015; AASEN et al., 2015). SfM works similarly to traditional stereoscopic photogrammetry approaches. In SfM methods, the IOPs and EOPs are estimated simultaneously, by means of a redundant and iterative bundle adjustment procedure using a dense set of features automatically extracted from multiple overlapping images, without the need for GCPs (WESTOBY et al., 2012). GCPs are necessary to transform the coordinates to a reference system.

2.3.2 Camera calibration

The inner orientation parameters (IOPs) define the internal characteristics of the sensor and make it possible to reconstruct the incident bundle of rays that formed the

image at the time of acquisition. The IOPs typically include the principal distance, principal point coordinates, lens distortions (BROWN, 1971) and affinity coefficients (HABIB et al, 2002, 2005). In order to generate reliable and accurate three-dimensional data from imaging systems, accurate knowledge about these internal camera characteristics is necessary (HABIB et al., 2006). The IOPs can be determined through the camera calibration process and different methods can be employed when handling different types of camera systems, such as perspective (BROWN, 1971; GRANSHAW, 1980; FRASER, 1997a; 1997b; CLARKE and FRYER, 1998; REMONDINO and FRASER, 2006) and multi-cameras (TOMMASELLI et al., 2013; HABIB et al., 2014). The technique that is most frequently employed for this purpose is a bundle adjustment with self-calibration. A common mathematical model for self-calibration, based on the collinearity equations with additional parameters, is provided by equations (1).

In the self-calibration process, the IOPs, the EOPs and the ground coordinates of the tie points are estimated simultaneously, using the image coordinates of these points and additional constraints. The estimation process can be performed without GCPs, provided that a minimum of seven constraints are introduced to define an object's reference frame (KENEFICK et al., 1972; MERCHANT, 1979; GRANSHAW, 1980). The frame definition can be done by constraining the six EOPs of one selected image and one or more distances (KENEFICK et al., 1972). Using the observed coordinates for the control points is another way to define the reference frame, but the existing errors in the GCPs will propagate to the network, except if seven absolute constraints are imposed. Free network adjustment is also an alternative that leads to better flexibility, but it still requires scale definition (GRANSHAW, 1980; HAGGRÉN and HEIKKILA, 1989). The IOPs and EOPs are highly correlated, and as a result, the system of linearised equations can be ill-conditioned. To reduce this linear dependence, several methods have been proposed, such as the convergent cameras method (BROWN, 1971; KENEFICK et al., 1972), the mixed-range method (MERCHANT, 1979) and methods based on 3D close-range calibration fields (FRASER, 2013).

The image observations used for the adjustment calculations can be measured either through automatic processes, by applying interest operators followed by an image-matching process, or via manual/interactive measurements. These processes can be troublesome depending on the characteristics of the scene, particularly when homogeneous areas or repetitive patterns are present. To address this problem, specially designed targets that can be automatically located and recognised in the acquired digital

images have been used in the calibration fields (HEIKKILÄ, 2000; FRASER, 1997a; HATTORI et al., 2002; SHORTIS et al., 2003). According to Fraser (1997a), the quality assessment of camera calibration parameters tends to be limited by the accuracy of image coordinate mensuration when analysing the consistency between the *a priori* and a posteriori variance factors. However, in the case of hyperspectral images, differences in the spectral response for each band can lead to false correspondences.

2.3.3 Epipolar geometry

Epipolar geometry is a powerful alternative for reducing the search space for matching homologue points. Figure 2 shows an image stereo pair with perspective centres PC_1 and PC_2, a point P in the object space and the corresponding points p1 and p2 in the images. The plane defined by PC_1, PC_2 and P is known as the epipolar plane. The two lines where this plane intercepts the images are called conjugated epipolar lines. There are infinite epipolar lines corresponding to the set of planes intercepting the images and containing the PC_1-PC_2 baseline (MIKHAIL et al., 2001). The epipolar lines can be determined after the stereopar orientation has been carried out. The advantage of epipolar geometry is that, assuming there is no error in the ray intersection, the image points p1 and p2 must lie in a conjugated epipolar line. The images can be transformed to normalized imagens, where epipolar lines are parallel to the image rows (SCHENK, 1999).Therefore, the search space for matching corresponding points can be restricted to a one-dimensional problem (usually the parallax is in *x* direction).

Figure 2: Epipolar plane and conjugated epipolar lines. Adapted from Mikhail et al. (2001).

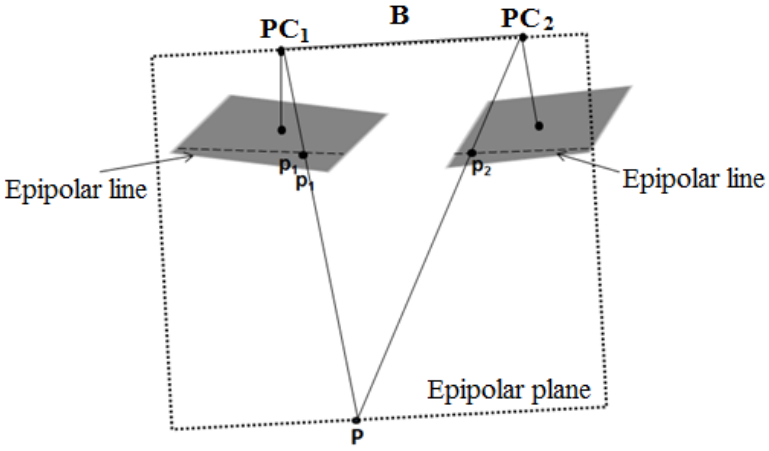

2.3.4 Vertical Line Locus

The Vertical Line Locus (VLL) method performs a geometric constraint in the search space during the image matching process, starting from the object space to the image space. If a point P appears on two images at least, a search interval is established along the vertical axis Z, considering an uncertainty range with minimum (ΔZ_{MIN}) and maximum (ΔZ_{MAX}) altitude values. The lower (Z_{MIN}) and upper (Z_{MAX}) bounds of P are projected to the images following the vertical line, incremented by an accuracy step (dZ), and the correspondence is performed by matching windows centered on points along the projection of a vertical line.

Figure 3 illustrate the concept. Assuming the IOPs and EOPs of each image are known, the main steps for implementing the VLL are:

(1) The planimetric position (X and Y) of a point P is selected. Maximum and minimum values are established ($Z_{MAX} = Z_0 + \Delta Z_{MAX}$ *and* $Z_{MIN} = Z_0 + \Delta Z_{MIN}$) to limit the search range for each vertical line search; also, a *dZ* increment is defined; Z_0 is the approximate height of the point;

(2) The height value is calculated by $Z_i = Z_0 + i \cdot dZ$, $i = 0,\ldots, (Z_{MAX} - Z_{MIN})/dZ$;

(3) The photogrammetric coordinates of the point (x_f, y_f) are calculated for each image, using the collinearity equations; the windows are defined taking these image coordinates as the center;

(4) The similarity measure is calculated at the positions found in (3);

(5) Steps 2, 3 and 4 are repeated until the largest height value Z_{MAX};

(6) Height Z_i, in the vertical line range, having the highest similarity value is selected. This height will be the estimated height of point P.

The correlation coefficient can be used to compute the similarity (KRAUS, 2007). Figure 3 (on the right) displays the similarity profile highlighting the point with the maximum similarity. The search vertical range ($Z_{MAX} - Z_{MIN}$) must be considered according to the characteristics of the region (mountainous, flat, urban buildings, etc.) as it influences the number of correct and false matches. Furthermore, it is essential to check the most appropriate value for the search step (*dZ*), since this value is directly related to the precision and computational efficiency of the method.

The image matching process with VLL was used to recover building heights through the integration of satellite images and IKONOS digital vector maps and images in Lee et al. (2011). Another application in this area is presented in Ji and Yuan (2008).

The authors applied VLL to detect changes in urban buildings from aerial images. Wan et al. (2010) used the method in the process of image matching for inspection of power lines. Oliveira (2013a) implemented the VLL technique with the multiple image matching approach and this method was tested over an urban area achieving accuracy compatible with ALS data (OLIVEIRA and TOMMASELLI, 2013b; 2014a).

Figure 3: Reduction of the search space by the VLL method and correlation profile generated from multi-images.

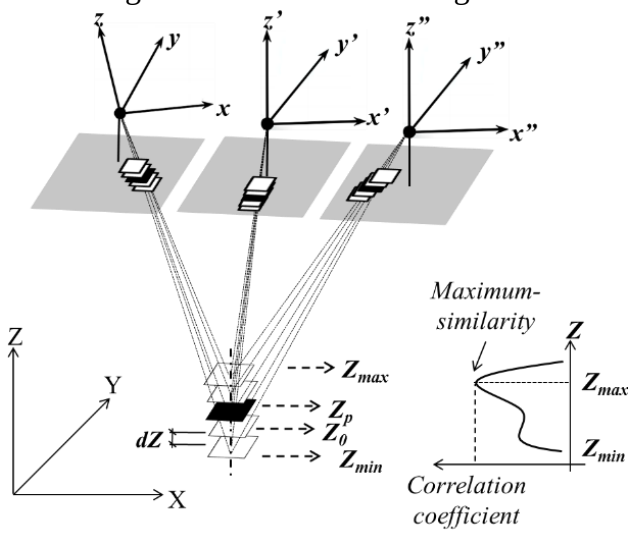

2.3.5 Image registration

Image registration can be defined as the process of establishing a mapping function between pixels of two images acquired under different conditions, such as time gap, difference of viewpoints, and/or by different sensors (BROWN, 1992; ZITOVÁ; FLUSSER, 2003). After the parameters of the mapping function have been estimated, the images can be resampled to the reference image. Image registration is an important preliminary step for many Remote Sensing applications, such as classification, environmental monitoring, change detection or image mosaic construction. Image registration allows a better understanding of the change detection of the scenes. A misleading in this procedure introduces false-rates. In addition, it is a process widely used in the field applications of computer vision and medical image analysis.

Most registration methods follow four steps (ZITOVÁ; FLUSSER, 2003):

- *Feature extraction*: features (corners, edges, etc.) are detected and can be represented by their attributes (gray levels, gradient, etc.) (HARRIS; STEPHENS, 1988; LOWE, 1999);
- *Feature matching*: the correspondence between the extracted features is established, considering the descriptor attributes and similarity measures;
- *Estimation of transformation parameters*: the mapping function parameters between the reference image and the image to be registered can be computed considering a bi-dimensional transformation (for example, affine, polynomial);
- *Image resampling*: the image is transformed through the mapping functions. In this step, one of the images can be resampled, using a suitable interpolation method for DN values, when necessary.

Geometric transformation parameters can be applied over the whole image or they can assume the image in multiple parts and estimate different sets of parameters for each region (BROWN, 1992). Mapping functions are usually geometric transformations, such as similarity transformation, affine, projective or polynomial equations. The transformation parameters can be estimated by Least Squares adjustment.

Similarity transformation is the simplest model consisting of a rotation, two translations and a scale. This model maintains the shape, since it preserves angles and curvatures. Affine transformation has six parameters: a rotation, two translations, two scales and a shearing angle, maintaining line parallelism. The projective transformation presents eight parameters to be estimated using at least four common points. The number of common points for estimating transformation parameters is generally greater than the minimum number required (ZITOVÁ and FLUSSER, 2003). The accuracy of mapping the pixels with a mathematical function is related to the differences of location and orientations of image acquisition, sensor errors and topographical relief variation.

In the case of hyperspectral 2D frame cameras, where each band of a data cube is acquired in a slightly different instant on a moving platform, the positions and orientations are different. The forward movement causes a displacement (d_{bij}) between bands *i* and *j*, which is a function of platform velocity (v) and time difference (dt_b).

$$d_{b_{ij}} = \frac{c}{(H-h)}\, v d_{t_b} \tag{2}$$

where c is the principal distance, H is the flight height, h is the point height and dt_b is the time difference between the bands.

In addition, platform movement can introduce relative orientation differences between the bands. Due to these camera features, a registration process between spectral bands is therefore required.

Vakalopoulou and Karantzalos (2014) analyzed the coregistration and the performance of the descriptors SURF (Speeded Up Robust Features), SIFT and ASIFT (Afine-SIFT) in FPI images. The bands were divided into similar spectral groups, with a reference band for each group. After the registration within the bands of each group, the groups themselves are registered. Affine transformation was applied showing the registration errors using ASIFT had the best result, varying from 0.35 to 1.33 pixels. However, the data sets used were acquired in relatively flat areas.

In Honkavaara et al. (2013), position and attitude are determined for reference bands and this information is then applied to all other bands. However, for large position and attitude differences among the spectral bands of a cube, an approach considering local distortions caused by displacement due to the relief is more suitable. BBA considering all bands would be another alternative (ROOSJEN et al., 2017), but it is not a feasible process in the case of large number of bands.

2.4 Overview on Image Matching

Image matching is a fundamental technique in many tasks in Photogrammetry, and widely applied in the field of computer vision, navigation, surveillance, automated guidance, robotics and medical image analysis (GRUEN, 2012). This technique deals with the identification and measurement of homologous points in two or more overlapping images. In digital Photogrammetry, the important applications of image matching include the generation of DSM, measurement of photogrammetric points and control points for image orientation, and automatic extraction of features (GRUEN, 1985; GRUEN, 2012; SCHENK, 1999).

The correspondences established in the image space generates a parallax (or disparity) map, which represents the depth of the pixels. The quality of this estimation is related to many factors of the algorithm.

According to Schenk (1999) and Gruen (2012) image matching was introduced in the early 1950s. Initially, it emerged as an analogical procedure using electrical circuits to solve matching equations. The totally digital treatment of the matching problem became possible with the advancement of computers in the 1970s (GRUEN, 2012).

Least Squares Matching (LSM) methods were developed in the 1980s, (FORSTNER, 1982; ACKERMANN, 1984; GRUEN, 1985). In the 1990s, multi-view approaches (SEITZ et al., 2006) and matching in the object space were investigated (GRUEN and BALTSAVIAS, 1988; MAAS, 1996).

However, image matching became more competitive with the considerable improvements achieved in algorithms and hardware after the year 2000 (HIRSCHMÜLLER, 2005, 2008; PIERROT-DESEILLIGNY and PAPARODITIS, 2006; HAALA, 2009, 2013; GRUEN, 2012; HAALA and ROTHERMEL, 2012; REMONDINO et al., 2014). Significant recent advancements include the object-space based approaches (ZHANG, 2005a; PIERROT-DESEILLIGNY; PAPARODITIS, 2006; OLIVEIRA and TOMMSELLI, 2014a), global optimization-based matching algorithms, such as the Semi-Global Matching (SGM) method and the developments of specialized hardware devices, including field programmable gate array (FPGA) and graphics processing unit (GPU) (GEHRIG et al., 2009; HIRSCHM et al., 2012).

Image matching methods can be classified as area-based matching (ABM) and feature-based matching (FBM). According to Scharstein and Szeliski (2002), in the field of computer vision algorithms it can be classified as either local or global methods.

2.4.1 Image matching methods

Feature-based methods (FBMs) require the extraction of interest points, edges and regions. Extracted interest elements are characterized by their attributes (descriptors, features), which can be coordinates, gradient magnitude, gradient directions, size and average brightness of regions, length, curvature, etc. Once features (descriptors) have been extracted from two or more images, the next step is to match comparing their attributes (features). The matching methods can use, for instance: the Euclidian distance of the attributes, compared against a threshold; area-based matching; Random Sample Consensus (RANSAC) to fit a geometric model, such as the affine transform; or comparing the hamming distance, when using binary algorithm.

Moravec (1979) developed the first detector of interest points, which was improved by Harris and Stephens (1988). Förstner (1987) detector uses auto-correlation function to classify pixels into categories (interest points, edges or region); the detection and localization stages are separated, into the selection of windows. Further statistics performed locally allow estimating automatically the thresholds for the classification.

Methods for detecting and describing scale-invariant regions (a set of pixels, not the same regions from segmentation) were proposed by LOWE (2004). Mikolajczyk and Schmid (2005) presented a comparison and evaluation of other group of detectors, which are invariant to affine transformations. Recently, binary descriptors have also emerged because of their high speed and low memory requirement (CALONDER et al., 2010; LEUTENEGGER et al., 2011; RUBLEE et al., 2011).

Nowadays, the SIFT algorithm (LOWE, 2004) is one of the most widely used feature detector and descriptor algorithms. SIFT detects a number of interest regions using the Difference-of-Gaussian (DoG) operator. The points are selected as local extrema of the DoG function and the descriptor is based on the gradient distribution in the detected regions. SIFT is invariant to scale, rotation and small geometric distortions (LOWE, 2004). Several adaptations of SIFT have been proposed in the literature (KE and SUKTHANKAR, 2004; MIKOLAJCZYK and SCHMID, 2005; BAY et al., 2008). In addition, extensions of SIFT to hyperspectral images were proposed by DORADO-MUNOZ et al. (2012) and MA et al. (2017).

FBM algorithms provide a sparse set of homologous points and their attributes. There are numerous applications for FBM methods: motion tracking, robot navigation, panorama building, bundle adjustment, image registration and initial points for DSM generation. The points and attributes can be used in object recognition and classification.

Area-based methods (ABM) compare the intensity values of pixels in a small local neighborhood of a reference window (template), with pixels of a target window in another image using a similarity function. The function can be, for instance, cross-correlation, correlation coefficient or sum of squared differences (SSD); and then the result can be refined by the least squares method (GRUEN, 1985). The window defined in the left image I1 (i, j) is assumed to be the reference template, which will traverse the right image I2 (i, j) (search image), comparing the digital number (DN) values to each window offset, using a similarity function. Figure 4 illustrates this process.

Figure 4: Area-based method.

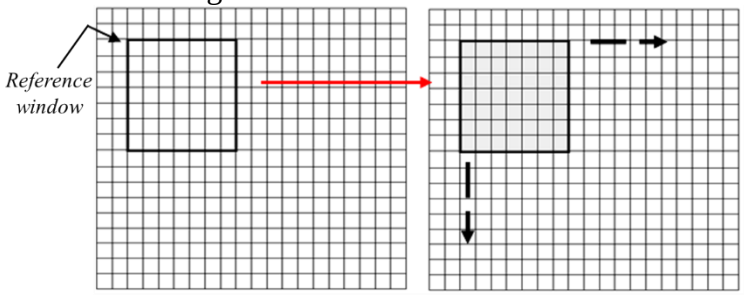

The rigid shape (square or rectangular) and fixed sizes of the correlation window can cause problems in the ABM techniques. If the window is too small and does not have enough intensity variations, the quality of the correspondence estimation is affected by the low signal/noise ratio. On the other hand, when the windows are larger covering a region with suitable DN gradient, the position of the matched point may not be true because of the geometric distortions (ACKERMAN, 1984; KANADE and OKUTOMI, 1991). In order to overcome these difficulties, some methods of correspondence using windows with adaptive sizes or positions (or both) have been proposed (KANADE and OKUTOMI, 1991; FUSIELO et al., 1997; CHAN et al., 2003).

Kanade and Okutomi (1991) proposed a statistical model to select the window size in each image pixel which produces the parallax estimate with the least uncertainty. The technique controls not only the size, but also the shape of the correspondence windows. The window size starts from 3x3, and then, if not enough similarity is achieved, the window size rises by one pixel in one of the four directions (x +, x-, y + or y-). If the expansion increases the uncertainty in the parallax estimation, the template stops increasing in that direction and starts the process in a different direction. The process is performed for each direction and, at the end, the direction with the smallest error is selected.

Other matching methods using windows with adaptive sizes or shapes (or both) were developed by Fusiello et al. (1997), Zhang, (2005b), Chan et al. (2003) and Zhang (2005) or using adaptive windows based on image segmentation (TAO and SAWHNEY, 2000; BLEYER and GELAUTZ, 2005). Additionally, to reduce the effect of projective distortion some authors wrap the image window according to the EOPs of the image and a surface which corresponds to orthorectify the templates (GRUEN, 1985; HARTLEY, 1999; ZHANG, 2005a; BETHMANN; LUHMANN, 2011).

Local and Global matching

According to Scharstein and Szeliski, (2002), the local and global stereo matching algorithms generally have four steps: (1) matching cost computation; (2) cost aggregation; (3) disparity computation/optimization; and (4) disparity refinement.

Local methods compute the disparity (parallax) map of a point based on the intensity values within a finite window. Some of the algorithms can be divided into steps 1, 2 and 3 (SCHARSTEIN and SZELISKI, 2002):

1. Compute the cost of correspondence, in this case, the squares difference of the intensity values in a given parallax;
2. The aggregation is performed by adding costs of correspondences from the square windows with constant parallax;
3. Parallaxes are calculated by selecting the minimum value added to each pixel.

Global methods usually work directly on the disparity calculation step. Initially, a global cost function, which combines data (step 1) and smoothness term need to be defined, then an optimization algorithm is used to find the minimum cost. Examples of optimization algorithms are max-flow, graph-cut and dynamic programming methods (SCHARSTEIN and SZELISKI, 2002). While max-flow, graph cuts and belief propagation work in a two dimensional optimization problem, dynamic programming approaches perform the optimization in independent scanlines in polynomial time. However, commonly it leads to streaking effects. Local methods have a simpler structure and larger efficiency compared to global methods. However, local methods are more problematic in homogenous areas (GU et al., 2008).

Hirschmüller (2005) developed the SGM method, which approximates a two-dimensional global aggregation matching cost constraint by computing the pixel matching cost through several one-dimensional paths in the image. This strategy minimizes the streaking effect problem of the dynamic programing (HIRSCHMÜLLER, 2008). The algorithm achieves similar accuracy to global matching algorithms, but significantly faster than by global methods (HIRSCHMÜLLER, 2008; HIRSCHMÜLLER et al., 2012). SGM has therefore been investigated and improved by several researchers and industries of different fields (GEHRIG et al., 2009; HAALA; ROTHERMEL, 2012).

2.4.2 Image matching problems

The performance of image matching algorithms can be affected by areas of poor texture, occlusion, repetitive texture, difference of illumination and reflectance, foreshortening from different perspectives, discontinuity, which represents the edges of objects (GRUEN, 2012). Noises and reflective properties between the images cause differences in gray levels (VOSSELMAN et al., 2004, p.483). In addition, complications are caused by geometric distortions related to the orientations and relief parameters (SCHENK, 1999):

- Difference in flight height causes different scales and with different rotation angles between two images, the same image pixels correspond to different locations in the object space.
- Effect of sloped surfaces: image pattern shapes corresponding to a sloped planar ground patch in object space are geometrically different. If the slope of the surface reaches a critical angle, it will not be visible in the consecutive image, producing the occlusions.
- 3D discontinuity areas: each pixel of the image matching window represents a surface with different elevations, so the conjugated pixels represent different locations in the object space. This will lead to a smoothing of the surface or to a spatial shift of the 3D structure of one half of the window size. This problem can be solved by using small window sizes or using windows with adaptive shape.

The problems discussed above mainly affect the outcome of area-based matching methods. In general, feature-based methods suffer the effects of geometric distortions much less (SCHENK, 1999). One way to avoid these problems is to restrict the search space and to use good approximations, which can avoid false correspondences and ensure the convergence of the function (SCHENK, 1999).

The precision of 3D reconstruction is affected by precision of IOPs and EOPs, matching precision, intersection angles and by the stereoscopic base-to-height ratio (B/H). Assuming that the baseline (B) and the principal distance (c) have no errors, the precision (σ_Z) of height (H) for a point from a stereo measurement in relation to the image space measurement accuracy (σ_{px}) can be expressed as (KRAUS, 2007):

$$\sigma_z = \frac{H}{B}\frac{H}{c}\sigma_{px} \tag{3}$$

Equation 3 shows that the precision of the photogrammetric measurement is a function of the image scale (1/(H/*c*)) and the base-to-height ratio. The base-to-height ratio (B/H) describes the intersection geometry quality. Small base-to-height ratios result in a weak ray intersection geometry. However, when the ratio increases, the image differences and consequently the matching difficulty increases and the number of points can become lower. The impact of multiple stereo image pairs with different base-to-height ratios on the dense image matching quality was evaluated in (HAALA, 2011; WENZEL et al.,).

2.4.3 Image and Object Space correspondence

The matching methods can be performed directly in the image space or using the projection of the image to the object space. In the case of image space, only the relative orientation between the images is necessary. Usually, images are resampled to the epipolar geometry before calculating the matching function, such that the epipolar lines become parallel. To obtain the three-dimensional positions of the points in the object space the photogrammetric intersection is executed after the determination of the homologous pairs (PAPARODITIS et al., 2002).

Object space correspondence is guided by the projection of points in the object space to the image space. Each cell of the template defined in the object space, with the center at (X, Y) and an approximate height Z_0, is projected to the reference and search images and an intensity value is assigned to each of them. Then, matching is performed in rectified templates. The resolution of the templates is equivalent to the images resolution. The displacement of the windows in the images is given by varying the height of the point, from a minimum to a maximum value (GRUEN; BALTSAVIAS, 1988; MAAS, 1996; PIERROT-DESEILLIGNY; PAPARODITIS, 2006).

Both processes are widely used in photogrammetric applications, such as the generation of DSM, since they help to reduce the effects due to perspective deformation and relative rotation between the planes of the images.

2.4.4 Correspondence of different spectral bands

Image matching algorithms are mostly performed using a single band of the images. Color can be considered an important attribute to distinguish elements present

in an image and for reducing the number of false correspondences, since spectral differences of the targets may help to discriminate them. Some studies can be found in the literature showing the best performance of the correspondence when using information from the RGB bands. Silva et al. (2007) tested the use of RGB and HSI models (hue, saturation and intensity) in image matching and showed that color increases the matching quality. Most of the studies in image matching, using hyperspectral images, are based on FBM algorithms to extract homologous points for the image registration process (ABDEL-HAKIM; FARAG, 2006; BROCKELBANK and YANG, 1989, CHAMBON and CROUZIL, 2005, HAJJDIAB et al., 2012). A few studies have used dense image matching approaches (KOSCHAN, 1993; MUHLMANN et al., 2001; FOOKES et al., 2004).

Originally, SIFT considered only grayscale images, but given the potential of using color information, several color-based SIFT descriptors were developed. For example, Abdel-Hakim and Farag (2006) implemented the technique called C-SIFT (Colored SIFT), in which R, G and B channels are used in constructing of the descriptor. Montesinos et al. (2000) presented an adaptation to the Harris method of detecting points of interest considering colour images. The authors propose a radiometric invariant vector of descriptors. Hajjdiab et al. (2012) created an extension to the method of Montesinos et al. (2000), in which they use a near infrared image (NIR), in addition to the visible images.

Compared to multispectral data, the spectral resolution of hyperspectral data offers greater potential for increasing targets discrimination and the quality of this detection. However, some bands may be discarded due to mutual correlation, sensor problems, and low dynamic range. Mukherjee et al. (2009) used some concepts of the SIFT technique to develop a method of extracting interest points in hyperspectral images. These authors used principal component analysis to reduce computational load and to reduce problems such as artifacts in the image, caused by linear scanning characteristics or sensor defects. In this technique, the process starts by generating a new set of images in which each pixel value is a linear combination of the original values. The generation of space-scale representation (LOWE, 2004) is performed individually on each PC. The stage of detection of extreme local candidates follows Lowe (2004).

Similarly, Dorado-Muñoz et al. (2012) used the idea of the SIFT descriptor to consider directly the vectorial nature of each pixel of the image directly. The proposed

method uses a non-linear diffusion vector to generate the space-scaling of each layer of the hyperspectral image. Vector ordering methods were used for the detection of local extremes and an extension of the Hessian matrix to reject ill-defined points on edges.

The treatment and manipulation of hyperspectral data for DSM generation considering dense correspondence methods is still a challenge to be studied in order to select techniques that enable more optimal use of all the information aggregated from the data, avoiding redundant data and the great computational cost.

2.5 Digital Elevation model

Digital elevation model (DEM) can be defined as a general term for a numerical representation of any type of surface elevation data. DTM refers to a specific type of DEM, which represents the bare soil surface, limited by elevation of the terrain without features above it, such as vegetation or buildings (PAPARODITIS and POLIDORI, 2002; EL-SHEIMY et al., 2005). On the other hand, DSM contains the elevation of points from the ground or above ground area (such as trees and anthropic features) (PAPARODITIS and POLIDORI, 2002).

The main techniques for representing a given surface in a digital form are (EL-SHEIMY et al., 2005):

- Contour lines are lines that represent the same elevation along the surface, respecting a constant interval between them. Since the surface is represented by contour lines, it is possible to use interpolation to determine the elevation of points between the curves (El-SHEIMY et al., 2005).
- Regular grid is an array structure that stores the elevations of regularly spaced points in the X and Y directions (EL-SHEIMY et al., 2005) related to a specified origin.
- Triangulated Irregular Network (TIN): in this data structure type, points are connected to form a set of triangular faces covering the entire surface. The surface is represented by a plane within each triangle. The combinations between the three types of elements (nodes, edges, triangles) form the TIN data structure (EL-SHEIMY et al., 2005). Usually, the most commonly used triangulation is based on the Delaunay criteria. This criterion considers that, for each triangle, the circumference of the three vertices must not contain any other point of the data set.

A set of points with their 3D coordinates (X, Y, Z), and available attributes (color, intensity of the return pulse) can be also referred to as 3D point cloud (REMONDINO and EL-HAKIM, 2006; REMONDINO et al., 2014). 3D point clouds are usually stored in a well-known Lidar Exchange Format (LAS format) (ASPRS, 2017). The LAS file format is a public binary file standard that preserves 3D information and the nature of the LiDAR (Light detection and ranging) data. This format was proposed by the American society for Photogrammetry and Remote Sensing (ASPRS) to the exchange of LiDAR data, but nowadays it is used for any (X,Y,Z) tuplet (ASPRS, 2017).

3D points can be generated from ALS data, photogrammetric methods, RADAR methos or classical surveying methods, using total station and GNSS receivers. These points can be converted after wards to some of the data structures above mentioned. DTMs can be obtained by filtering the non-ground points from DSMs or from field surveys, which give low density compared to images and ALS.

Interpolation is also a fundamental technique for generating DSMs or DTMs, and is used in several steps, such as quality control, surface reconstruction and terrain analysis (LI et al., 2005). Interpolation methods can be used to convert an irregular into a regular sample and resample one grid to another level of resolution. Commonly used interpolation methods include linear interpolation, nearest neighbor, bilinear interpolation, simple mean, weighted average, cubic convolution and kriging (EL-SHEIMY et al., 2005).

2.6 DEM generation using image matching

The development of digital cameras and matching algorithms has increased research and interest in using optical images to acquire spatial data from image matching methods, as emphasized by Haala (2009; 2012), Gruen (2012) and Remondino et al. (2014). The three-dimensional ground coordinates can be calculated from the matched image coordinates using spatial intersection when IOPs and EOPs are known. The collinearity equations (1) represent mapping functions between object space (3D) and image space (2D) as a function of those IOPs, EOPs (ω, φ, κ, X_0, Y_0, Z_0) and 3D point coordinates (X, Y, Z). When using multiple images, it is necessary to know all the parameters involved in the orientation process for each image with a high degree of accuracy to the best interception of the multiple rays in the object space.

Algorithms for DEM generation from optical images usually rely on a search space reduction method, such as epipolar search, either by resampling or by determining the epipolar lines, or using VLL (2.3.4). A coarse-to-fine approach using hierarchical levels of image resolution is also important. According to Gruen (2012), an important aspect of DSM algorithms is correspondence with adaptive determination of the matching parameters (search window, thresholds, etc.) resulting in higher success rates and fewer mismatches. This is done by analyzing the results of the previous levels of the images pyramid.

Multiple image matching methods use all the available images simultaneously to reconstruct 3D objects (GRUEN, 1996; ZHANG, 2005; HAALA, 2011). Multiple image matching combines information redundancy, increasing correspondence success and reliability. Consequently, problems caused by occlusion, multiple solutions, homogeneous areas and surface discontinuities are reduced (GRUEN; BALTSAVIAS, 1988; ZHANG, 2005b; HAALA, 2011). On the other hand, it is important to emphasize that multi image matching techniques significantly increase the computational cost of the algorithm.

Gruen (1985) presented an adaptation of the mathematical model of the least squares correlation method for multi-image least squares correlation. In addition, the collinearity equations were introduced as geometric constraints. Based on Gruen (1985), Baltsavias (1991) developed the MultiPhoto Geometrically Constrained Matching (MPGC) algorithm, which combines intensity matching (gray levels) with geometric constraints derived from the intersection of multiple windows.

Recently, algorithms based on the SGM method have been widely implemented for DSM generation with resolution at GSD level (HAALA, 2013; REMONDINO et al., 2014). In most cases using SGM, dense matching is performed in image space considering all possible pairs of images and the results are combined based on the quality of the intersection rays (HIRSCHMÜLLER, 2008; HAALA; ROTHERMEL, 2012). After the determination of homologous points, image space techniques must execute the photogrammetric intersection process to obtain 3D point coordinates in the object space. This step is not necessary when considering matching methods in the object space because the height of the point is obtained directly by the matching process and the planimetric coordinates are implicit in the process. Zhang et al., (2017) presented a new adaptation of SGM, using the VLL technique to perform the correspondence in the object space.

Oliveira and Tommaselli (2014a) presented and evaluated a methodology for DSM generation using the VLL and area-based method adapted for the use of multiple images. Experiments were performed using an area that presented elements such as trees, repetitive patterns and homogeneous surfaces.

In order to evaluate the potential of different software, a set of reference data was provided by ISPRS/EuroSDR (International Society for Photogrammetry and Remote Sensing) giving rise to the Benchmark on High Density Image Matching for DSM Computation (HAALA, 2014). The datasets included scenes recorded from terrestrial and aerial blocks, acquired with convergent and normal (parallel axes) images, and with different scales. Quality control was performed by analyzing the differences between the DSMs generated by each software and the DSM obtained as the average of all. It is worth noting that the evaluation of the DSMs was not carried out in dense forested areas. Remondino et al., (2014) presented a review and analysis of four dense image-matching software (open-source and commercial), for the generation of dense DSM.

The results showed that research groups as well as commercial institutions provided photogrammetric software capable of generating dense, reliable and accurate 3D point clouds. The major problems were observed in shaded areas around buildings, trees and repetitive patterns.

Other types of the DEM can be generated from DSM and DTM, for example, the Canopy Height Model (CHM). CHM is acquired by the subtraction of DSM and DTM, and can used to extract metrics that are correlated with the vertical structure of the forest (HONKAVAARA et al., 2013, PERSSON et al., 2012). Usually, CHMs are generated using both DSM and DTM from ALS, which provides points from canopy and ground points. The combination of photogrammetric DSM and ALS DTM has also been used (DALPONTE et al., 2008; CLARK et al., 2011).

2.6.1 Hyperspectral DSM

Advances in hyperspectral sensors, mainly in spatial resolution, and in the accuracy of spectral description of targets have extended the interest in combining spectral information and high resolution 3D spatial data.

In remote sensing, radiometric values of the same point vary because of many physical issues, such as atmospheric effects, variable illumination conditions and sensor non-uniformity. Furthermore, values are anisotropic as a function of illumination and

viewing direction. The bidirectional reflectance distribution function (BRDF) has been developed to model this phenomenon (SCHAEPMAN-STRUB et al., 2006).

The bidirectional reflectance factor estimation (BRDF) describes the relationship between geometric characteristics (zenith and azimuth angles) of solar irradiance, and the sensor system viewing geometry (Figure 5) (JENSEN; SCHILL, 2000; JENSEN, 2009). Images of forest canopy make a complex scene due to the multifaceted geometric shapes of the canopy, occlusions, shadows, movements, structural similarities, variations in solar illumination and in viewing angles.

Figure 5: Bidirectional reflectance geometry. θi, θr, φi, and φr are respectively the zenith and azimuth angles of incident (i) and reflected (r) radiance (SUOMALAINEN et al., 2014).

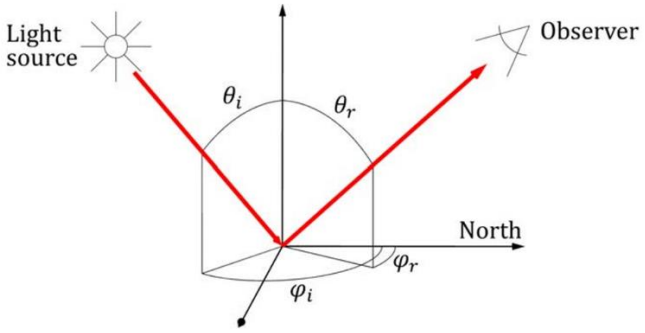

The BRDF can affect the radiometric characteristics of the data, and the effect is higher when the data are acquired off-nadir. Thus, it is important to understand the BRDF to correct radiometric variations and as a source of information for calibrating, validating, and increasing reflectance data accuracy (JENSEN; SCHILL, 2000). An important data for this issue is a DSM with hyperspectral information integrated.

A point in the HDSM is composed of a spectrum of multiple cubes and their angular properties, since the geometric relationship of Sun (azimuth and zenith)-target-sensor are known. The target-sensor relations are computed from EOP, IOP and point coordinates. Thus, the DSM with spectral information can also be used to study the 3D geometric and spectral properties of objects and BRDF. Classification and filtering of objects belonging to the DSM can be improved by the integration of spectral information.

Integration of the spectral information obtained in hyperspectral images into the DSMs has been performed indirectly by fusing data obtained by different sensors, and, in some cases, also at different times. In these cases, the DSM is obtained either by ALS data or by image matching with high resolution RGB images. All the data involved are

re-mapped to the same spatial resolution, and the spectral information is associated with the DSM by a registration process. Avbelj et al. (2014) presented an approach for the fusion of hyperspectral images and DSMs obtained by ALS and using contours of roofs as reference features for data registration. The features extracted from both data were matched and transformation parameters estimated. Dalponte et al. (2008) used a sample of points as features to compute the transformation parameters between hyperspectral imagens and an ALS DSM. The results showed that the integration of ALS and hyperspectral data increased the performance of tree species identification. Other studies have investigated the integration of hyperspectral data and DSMs generated from RGB images (SUOMALAINEN et al., 2014; NEVALAINEN et al., 2017).

Despite promising results, the use of data from different sensors can pose several problems, for instance: (1) degradation of the data with the resampling step, (2) errors resulting from the inaccuracy of georeferencing, orthorectification and the registration process; (3) occlusions due to different viewpoints of each sensor; (4) mismatches and errors due to the different acquisition time. Hyperspectral 2D frame-format images can be used to generate HDSM without the need of integrating DSM and spectral data from different sensors. However, most photogrammetric or SfM software do not support export point clouds with more than up to three DN values (usually intensity or RGB).

Roosjen et al. (2017) has used all bands in the adjustment with Agisoft PhotoScan for estimating the every band EOPs. Aasen et al. (2015) proposed a method to derive 3D hyperspectral information from a lightweight hyperspectral 2D frame camera for RPAs for vegetation monitoring. The hyperspectral 2D frame camera used was a Cubert UHD 185, which acquires registered bands. The first image band of the cube is a gray scale image with 1000 x 990 pixels and the others bands are images with 50 x 50 pixels with wavelengths from 450nm to 950 nm. Aasen et al. (2015) used an SfM technique implemented in a commercial pacakage (Agisoft Photoscan) to estimate the external orientation of the cubes and to generate the DSM. The gray scale band was set as the reference channel to perform the image matching process and the other bands were resampled in advance to the gray scale resolution using nearest neighbor interpolation. Because Photoscan only exports point clouds with up to three bands (in the time of the research until now), the authors exported each orthorectified image cube separately with the same spatial resolution as the DSM. The orthorectified cubes were then imported in ArcGIS software, to combine the pixels containing real data (not interpolated) with the

3D information. The resulting HDSM was used to derive biochemical and biophysical plant parameters, which were compatible with other studies in the area.

In the context of high spectral resolution sensors, the spectral information can contribute to the process of image matching and, consequently, to higher quality 3D model generation. This study presents the first approach to combine simultaneously the DSM generation and the multiangular hyperspectral data generation. The hyperspectral 2D frame sensor time-sequential acquisition mode is considered, thus the bands can have distinct IOPs and EOPs while are related to their respective cube, allowing a proper assignment/projection of spectral information to the 3D points.

3. STUDY AREA AND PROPOSED METHODOLOGY

Different study areas were selected in order to access different tasks of the photogrammetric process. The study areas are located in Brazil and Finland (Figure 6).

Figure 6: Study areas approximation location. (a) Brazil, São Paulo State. (b) Finland. (c) Ponte Branca and Morada de Deus in São Paulo State. (d) Evo and Vesijäko, Finland. (e) Ponte Branca fragment and (b) Morada de Deus.

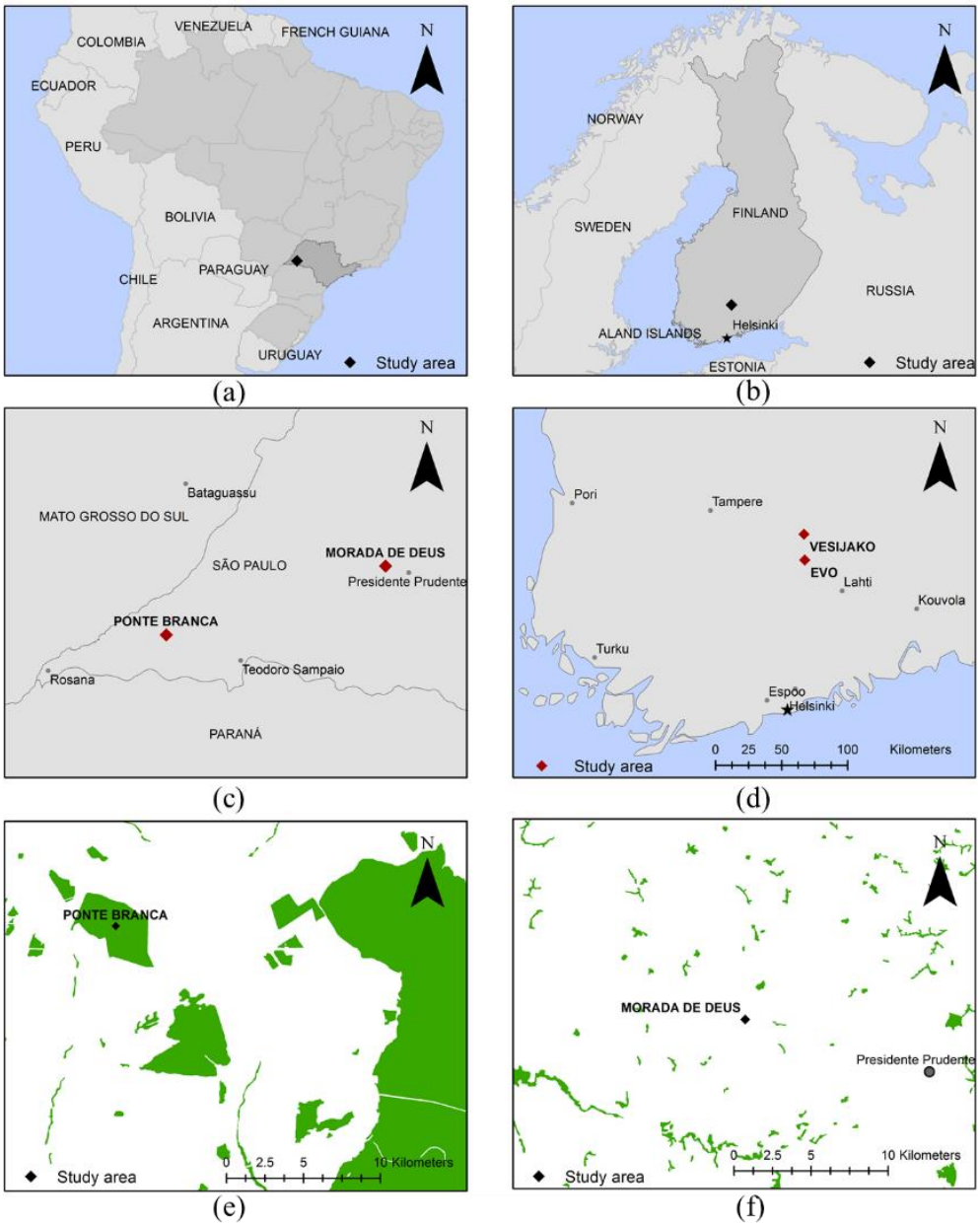

The data set of two areas, collected by the FGI research group, were used from Finland. The first area was in Evo (61°11’10”N, 25°07’10”E), located in southern Finland. The area is a Scots pine forest, with a tree density of 400 stems per hectare. The tree height average is 20 m. The FPI image block was collected with flying height from ground level of 100 m, resulting in a GSD of 10 cm. The flight speed was 3.6 m/s. From this data only one cube was used to perform the assessment of the band co-registration process using 2D transformation functions. The study is described in Chapter 5.

The test area used in the EOP estimation analyzes (Chapter 6) and HDSM generation (Chapter 7) was located in Vesijako, in southern Finland (61°21’40”N, 25°6’4”E). A research forest area in the municipality of Padasjoki. The primary tree species in the image block area was Birch (*Betula pendula*) with an average tree height of 21 m. A detailed description of the area can be found in Nevalainen et al., (2017). The data capture was carried out on 26th of June 2014, using a Tarot 960 hexacopter (Figure 7) and during the full-leaf season.

Figure 7: FGI’s Tarot 960 hexacopter.

In Brazil, a parking area of the Morada de Deus (22°5’44”S, 52°29’48”W), located in Ávares Machado, São Paulo State, Brasil, was used for the first flight experiments with the RPAS acquired by Unesp.

The most part of the original Atlantic forest has been devastated and the remaining areas are spread in small fragments, about which insufficient information is available. The study area is one of these fragments, called Ponte Branca (22°24’51”S, 52°30’50”W), which is part of a Federal Protected Reserve, named Estação Ecológica Mico Leão Preto (ESEC MLP), in Teodoro Sampaio, São Paulo State, Brazil. The forest

structure contains multiple canopies that support a rich vegetation diversity, which can be characterized as alluvial (riparian forest) or sub montane, depending on the altitude, which ranges from 350 to 450 m. The fragment is a dense tropical forest composed of native tree species within an area of approximately 13 km^2 (BERVEGLIERI et al., 2016).

Tropical and boreal forest have many differences in the vegetation and landscape. Evo and Vesijäko forest has more separated high trees, and the ground is visible in many areas, as can be seen in Figure 8. On the other hand, Ponte Branca fragment has a dense canopy with many tree species, varying in shape and height (Figure 9).

Figure 8: Evo forest area (a) terrestrial and (b) perspective view (HONKAVAARA et al. 2014).

Figure 9: Ponte Branca fragment (a) terrestrial and (b) perspective view.

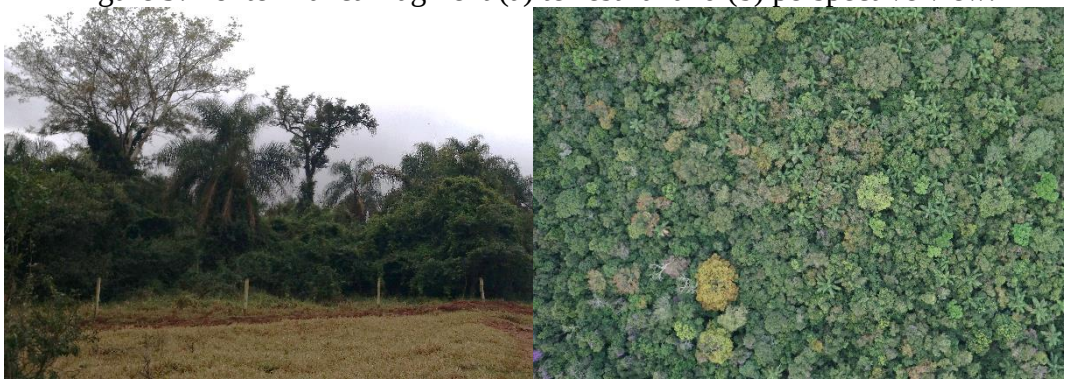

The proposed methodology of hyperspectral DSM generation using a lightweight hyperspectral 2D frame camera based on tuneable FPI is described in the following chapters. The processing chain was organized as follows: camera calibration; pre-marked target positioning and flying survey; bundle block adjustment of selected bands; and DSM generation using multiple bands.

Before starting the process of DSM generation, it is necessary to provide accurate IOP and EOP of the images and an approximate DSM that must be a regular grid. The

thresholds used in the correspondence must be defined beforehand and can be changed at each level of the image pyramid, due to the different resolutions. The DSM generated at each level of the pyramid is interpolated and used as the initial model for the subsequent level.

The basic steps of the DSM generation process are represented in the workflow of Figure 10 and are detailed in the following sections. Two techniques for HDSM generation can be seleted: (1) hyperspectral VLL (HVLL) - without classification information; or (2) hyperspectral VLL classes (HVLLC) - using classification information.

Figure 10: Workflow of the proposed method.

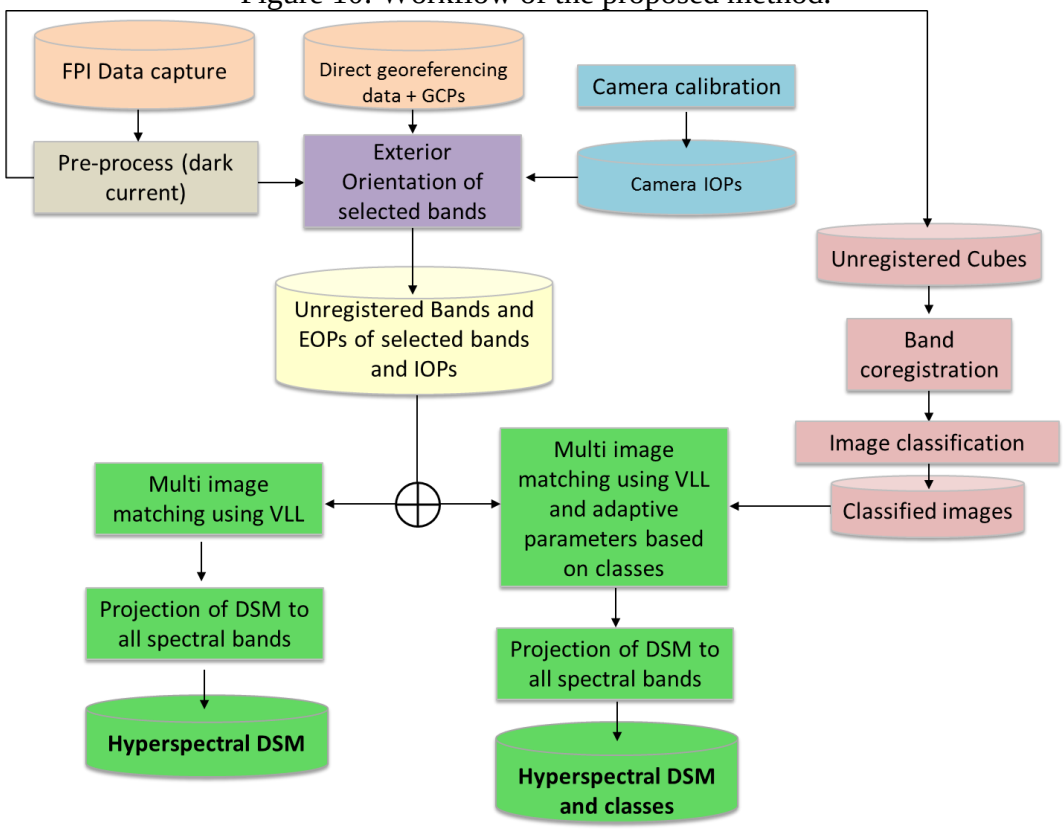

4. GEOMETRIC HYPERSPECTRAL FRAME CAMERA CALIBRATION

Hyperspectral 2D frame cameras using FPI filter, such as FPI camera, have a complex system to acquire images along each cube. IOPs can exhibit variations due to differences in the internal camera elements and the environmental conditions (JACOBSEN and WEGMANN, 2002). Špiclin et al. (2010) have highlighted that optical aberrations can vary among different spectral ranges of hyperspectral images, potentially leading to inaccurate geometric calibrations. Bowmaker et al. (2011) have shown that the principal point can exhibit fluctuations due to the effects of variations in the refractive index with respect to wavelength.

The majority of investigations involving the geometric calibration of hyperspectral systems have not estimated the rigorous physical IOPs using photogrammetric methods. Once the UNESP's FPI camera has not only the FPI technology, but also two single-colour CMOS image sensors to acquire a sequence of spectral images, it is important to investigate whether only one group of IOPs is sufficient for representing the internal geometry of the camera.

This chapter is based on the investigation presented by OLIVEIRA et al. (2016a). In this study, the first comprehensive analysis of the geometric calibration of a novel kind of a FPI-based hyperspectral 2D frame camera was performed. The objectives of this investigation were to estimate and analyze the behavior of the IOPs of the hyperspectral 2D frame camera; to assess the feasibility of calibrating the FPI camera using the self-calibrating bundle adjustment with the Conrad-Brown model for the IOPs; and to assess the feasibility of coded targets in the case of this camera.

It is worth noting, that in addition to the different bands selected here, the camera has also small differences compared to Oliveira et al. (2016a), since the company has made some upgrades on the camera. Additionally, images were not collected in the 3D terrestrial calibration field, but using a flat panel and some improvements in the image measurement were done. The panel was used to verify if the differences found in the previous work was related with acquisition problems, such as movements of the camera.

4.1 Camera Configuration and Image Acquisition

In this study, the sequence of the bands to be acquired for the calibration process was selected based on the spectral characteristics of the Atlantic forest tree species of the study area. The sequence was formed by 25 bands with 1017 × 648 pixels, with 15 bands being recorded by Sensor 1 and 10 bands recorded by Sensor 2 (see Table 2).

The calibration was performed using a camera-calibration panel containing coded targets with the ArUco codification (GARRIDO-JURADO et al., 2014; SILVA et al., 2014; TOMMASELLI et al., 2014). Each target was 7 cm × 7 cm in size and consisted of a rectangular external "crown" and a 5 × 5 internal array of squares arranged in five rows and five columns (Figure 11 (a)). In order to reduce possible errors due to the quality of the object borders definition in the bands, after the corners of a given ArUco target were located, the centroid of the targets were computed by averaging the image coordinates of the corners, differing from experiments developed in Oliveira et al. (2016a), in which corners were used. Because of the narrow dynamic range of some images, the automatic target detection failed for some corners even after applying contrast enhancement.

Table 2: Air gaps, wavelengths and full width of half maximum (FWHM) of the cubes.

Sensor 2			**Sensor 1**		
Gap (nm)	λ (nm)	FWHM (nm)	Gap (nm)	λ (nm)	FWHM (nm)
337	506.2	12.4	814	650.96	14.4
603	519.9	17.4	498	659.72	16.8
628	535.09	16.8	509	669.75	19.8
653	550.39	16.5	519	679.84	20.5
678	565.1	17.3	530	690.28	18.87
703	580.16	15.9	541	700.28	18.95
722	591.9	16.6	551	710.06	19.7
750	609	15.1	561	720.168	19.3
768	620.2	16.3	571	729.57	19
782	628.7	15.3	583	740.42	17.97
			593	750.16	17.97
			613	769.89	18.7
			625	780.49	17.4
			635	790.3	17.4
			666	819.66	17.85

In this study, the authors will refer to the set of bands for each acquisition as a cube, since the camera remained static during each exposure.

Twenty cubes were acquired, resulting in a set of 500 images. Cubes were acquired with different positions and rotations to minimise the linear dependency between some IOPs and EOPs. Figure 11(a) presents the target panel and the points (P1, P2 and P3) that were used to define the reference system. Figure 11(b) shows a sample image after target corner detection. The approximated distance between the main stations is 2 m.

Figure 11: (a) Example of a target in the 3D calibration field at UNESP and the stations for data acquisition, the dimensions in the calibration field, (b) the schema for the image acquisition.

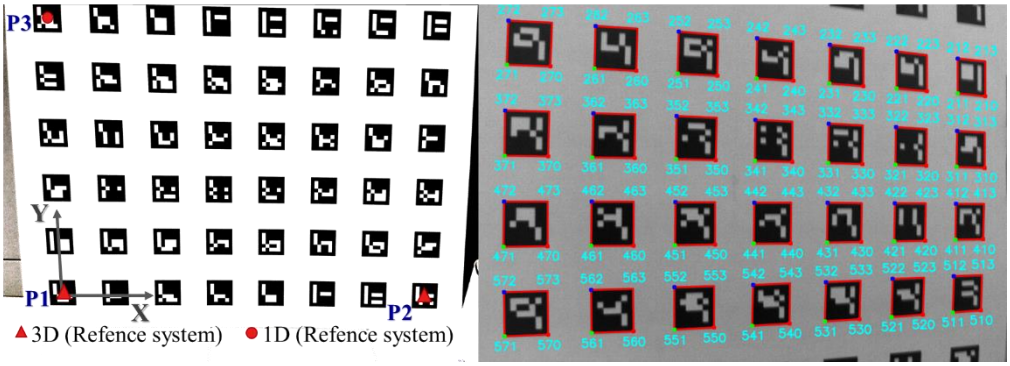

(a) (b)

4.2 Self-calibration of FPI Camera

Three points were used to establish the object's reference frame, providing the minimum of seven absolute constraints to perform the self-calibrating bundle adjustment. Point P1 was selected as the origin of the system. The distance between the points P1 and P2 was accurately measured using a caliper with a precision of $\sigma = 0.2$ mm to define the scale of the photogrammetric network. The Y coordinate of point P2 was set to be the same as that of point P1, and thus the distance defines accurately the X coordinate of P2. The coordinates of the remaining GCPs were introduced into the bundle adjustment calculation as weighted constraints with a standard deviation of 3 cm, which effectively made them free unknowns. With this approach, possible errors in the control point coordinates do not affect the IOP estimates. Therefore, the IOPs, EOPs and object coordinates of the tie points were simultaneously estimated in the adjustment based only on internal information, with the exception of the distance in object space.

The self-calibration adjustment was performed using an in-house software termed Calibration with Multiple Cameras (CMC) (TOMMASELLI et al., 2013), which uses a

least-squares combined model with constraints (unified approach as defined by Mikhail, 1976, p. 133). Three experiments were performed similarly to those described in Oliveira et al. (2016a):

(1) Calibration 1: Individual calibration for each band. This experiment consisted of 25 independent calibration trials of 20 images each, resulting in 25 sets of IOPs, one set for each band

(2) Calibration 2: Individual calibration for each sensor. This experiment consisted of one calibration trial using all of the images to estimate two IOP sets: (a) one for Sensor 1, with the bands corresponding to this sensor, and (b) one for Sensor 2, with the corresponding bands.

(3) Calibration 3: All images were combined in a single calibration process to produce a single set of IOPs.

The standard deviations of the automatic image observations (σ_{x_auto}, σ_{y_auto}) were considered to be $\sigma x_{auto} = \sigma y_{auto} = 0.5$ pixels. The same initial values for the EOPs and the respective weights ($\sigma_{X0} = \sigma_{Y0} = \sigma_{Z0} = 0.10$ m and $\sigma_{\omega} = \sigma_{\varphi} = \sigma_{\kappa} = 10°$) were used in all experiments.

Quality control

The quality of the estimated parameters was assessed based on estimated standard deviations for each parameter and the a posteriori variances (standard error of the unit weight), which represents the global quality of the adjustment. Statistical tests were applied to verify whether the IOP values obtained in different calibration trials were significantly different at a given significance level (SHORTIS and HARVEY, 1998; HABIB et al., 2002). According Shortis and Harvey (1998) the statistical significance of the changes in each IOP from different calibration sessions can be computed by Equation 4.

$$Significance_i = \frac{|\text{parameter}_{i,n+1} - \text{parameter}_{i,n}|}{\sqrt{\sigma^2_{i,n+1} + \sigma^2_{i,n}}} \sim Student's\ t \quad (4)$$

In which *parameter* corresponds to one of the i parameters from the set of estimated IOPs, n and $n + 1$ represent the calibration experiment and σ_n^2 is the variance associated with the parameter used in calibration experiment n. The significance value can be tested against the *Student's t* distribution, where the degree of freedom is the same of the calibration adjustment.

Afterwards, the Zero Rotation (ZROT) method proposed by Habib et al. (2006) was applied to assess the impact of each IOP set in the image space using data extracted from the calibration trials. The method does not allow for spatial and rotational offsets with respect to the bundles, which is quite compatible with the setup used in this investigation. First, a synthetic regular grid is defined in the image space. The two compared sets of IOPs were applied to the simulated grid vertices to remove the distortions, thereby generating two distortion-free grids. Since the principal distances were different, the resulting coordinates for the new grids were projected onto the same plane (image plane of the first IOPs set). Finally, the similarity is assessed by computing the root mean square errors (RMSEs) of differences between the two distortion-free grid coordinates. If the differences were within the expected standard deviation of the image coordinate measurements, then the IOPs set could be considered to be equivalent (HABIB et al., 2006).

4.3 Experiments and results: camera calibration

The self-calibration adjustment for each experimental configuration was performed using ten IOPs (c, x_0, y_0, k_1, k_2, k_3, P_1, P_2, A and B), eight (c, x_0, y_0, k_1, k_2, k_3, P_1 and P_2), six (c, x_0, y_0, k_1, k_2, k_3) and without k_2, and k_3. The analysis of the results showed that the affine parameters did not exhibit significant effects in the image coordinates. In most cases, the elimination of the k_3 did not result in considerable differences from the results obtained with eight IOPs. However, the image coordinates residuals increased for some bands of Sensor 2 when neglecting k_3 , which means that k_3 should be maintained to have the same set of parameters. The elimination of k_2 and k_3 increased the standard deviation of the estimated parameters and the *a posteriori* variance factor. Thus, since using k_2 and k_3 was beneficial for most of the bands and did not decrease significantly the results for the other bands, the set of eight IOPs was selected to be used in all experiments in order to have the same set of parameters for the sake of comparison.

Figure 12 presents the RMSE values of the residuals in the estimated image x and y coordinates for each self-calibrating bundle adjustment using the IOPs: c, x_0, y_0, k_1, k_2, k_3, P_1 and P_2. All values were less than 0.15 pixel, consequently smaller than the precision of automatic measurement, which indicated that the used sensor model fitted well with the data. The RMSE values were higher for the bands 506.22 nm (Sensor 2)

and 650.96 nm (Sensor 1), which are the first bands acquired on each sensor. The quality of these bands was poorer in comparison to the others, having more noise. This is probably due to the smaller FWHM (Table 2). The results for the combined calibration (Calibration 2) of S1 and S2 were similar to the results for the individual bands, suggesting that combined calibration for each sensor is just as good as the individual calibrations for each band. Calibration 3 provided the highest error, suggesting that a single calibration was not sufficient.

Figure 12: RMSE of the image coordinates residuals in the x (columns)) and y (rows) directions for Calibration 1, Calibration 2 Sensor 1 (C2(S1)), Calibration 2 Sensor 2 (C2(S2)) and Calibration 3 (C3).

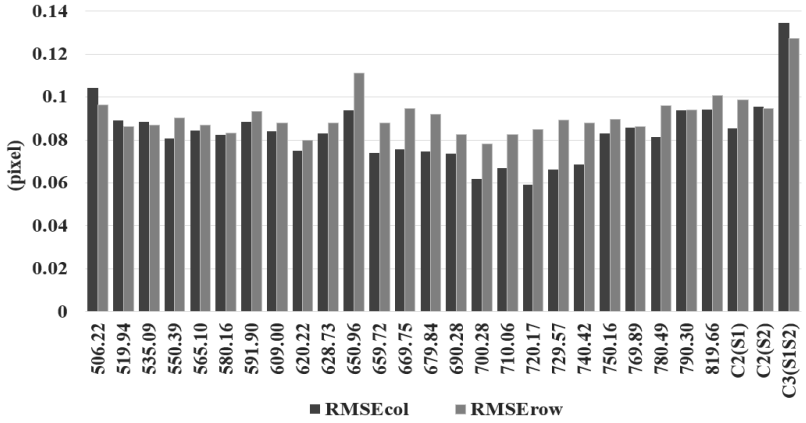

Figure 13 shows the principal distance (c) estimated for each experimental configuration (Calibrations 1, 2 and 3) and the standard deviations of the estimated values. The differences between the maximum and minimum principal distance in Calibration 1 were 0.02 mm (20 μm) for the Sensor 1 bands and 0.012 mm (12 μm) for the Sensor 2 bands and the standard deviation of principal distance among the bands were 0.006 mm (6 μm) and 0.004 mm (4 μm), for the Sensor 1 and Sensor 2 bands, respectively. The principal distance standard deviations estimated for Sensor 1 and Sensor 2 in Calibrations 2 were 0.00015 mm (0.15 μm) and 0.00017 mm (0.17 μm) and in Calibrations 3 was 0.001 mm (1 μm).

Figure 13: Estimated values and standard deviations (error bars) for the principal distance estimated for Calibration 1 (C1), Calibration 2 Sensor 1 (C2(S1); upper line), Calibration 2 Sensor 2 (C2(S2); lower line) and Calibration 3 (C3; middle line).

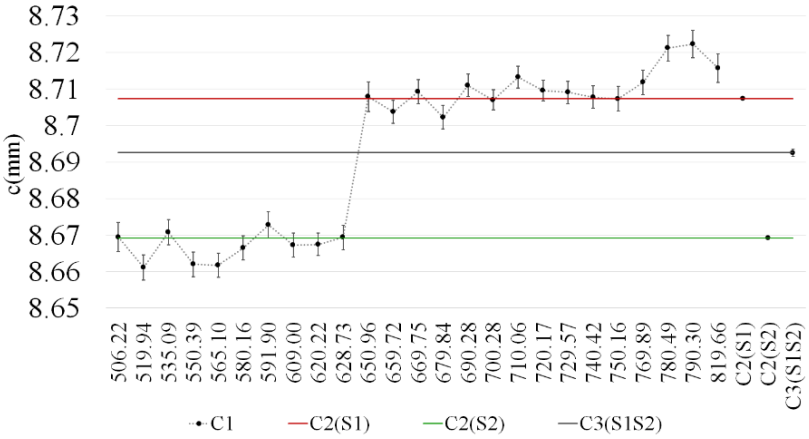

Figure 14 presents the corresponding values and standard deviations for the principal point coordinates. A diagram of the estimated principal point coordinates for each experiment (Figure 15) confirms the clustering of principal point locations and the proximity of the points among the bands of each sensor. For the Calibration 2 and Calibration 3, the corresponding error ellipses are also shown in (Figure 15).

Figure 14: Estimated values and standard deviations for the principal point x_0 (a) and y_0 (b) obtained during Calibration 1 (C1), Calibration 2 Sensor 1 (C2(S1)), Calibration 2 Sensor 2 (C2(S2)) and Calibration 3 (C3).

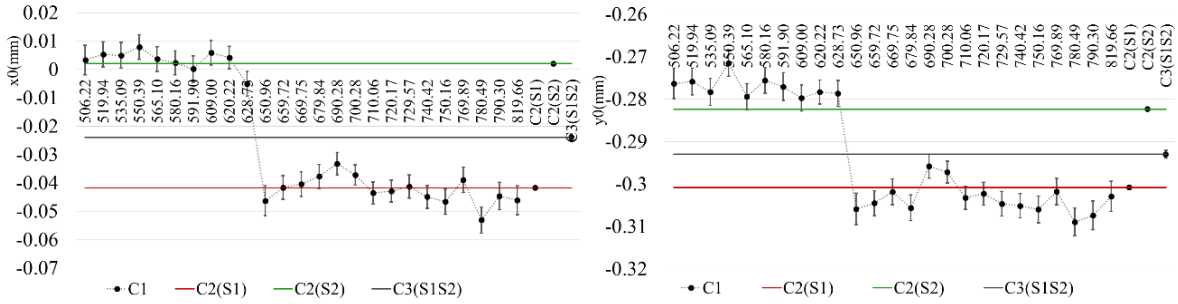

Figure 15: Principal point location for Calibration 1 (C1), Calibration 2 Sensor 1 (C2(S1)), Calibration 2 Sensor 2 (C2(S2)) and Calibration 3 (C3) as well as error ellipses for the principal point in Calibrations 2 and 3.

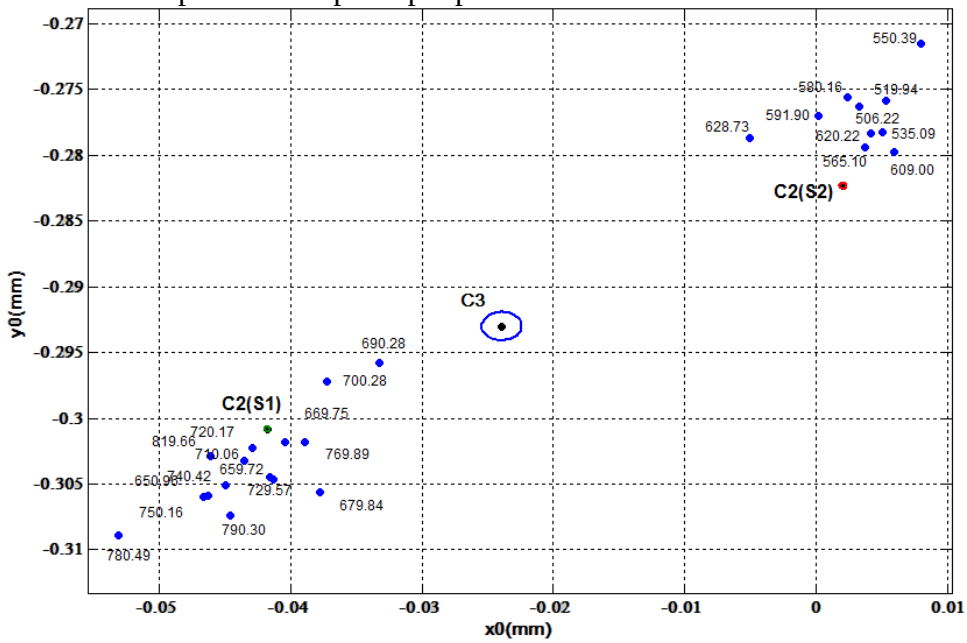

The radial distortion parameters obtained for Calibration 3 and for each sensor during Calibration 2 were used to calculate the sensors radial distortion curve and the differences between them (Figure 16). The combined effect of these parameters led to greater radial distortion for Sensor 1. The radial distortion at a radius of 3.1 mm was -0.14 mm and -0.126 mm for Sensor 1 and Sensor 2, respectively.

Figure 16: Radial distortion obtained in Calibration 2 Sensor 1 (C2-S1) and Calibration 2 Sensor 2 (C2-S2) and the difference obtained for C2(S1) – C2(S2).

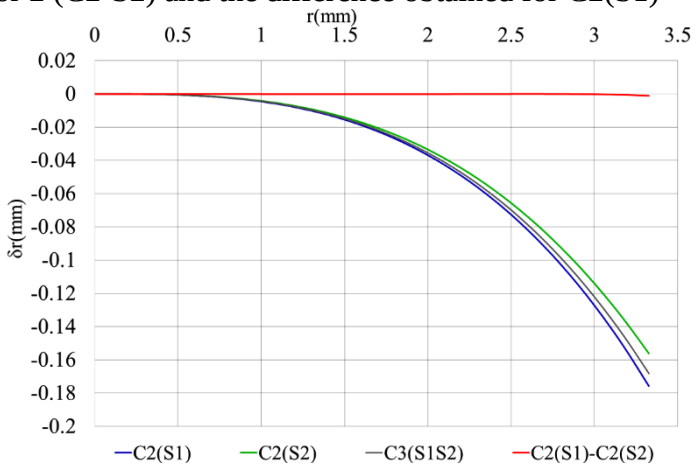

The effect of the decentring distortion parameters P_1 and P_2 were larger for Sensor 1 than for Sensor 2 (Figure 17). This can be due to the different optical path for the two sensors as illustrated in Figure 1 (d). The parameter variation among individual bands of

both sensors was very small. One outlier was observed (band 11, λ = 650.96 nm, first of sensor 1); its reason was not identified, but it can be related with image quality.

Figure 17: Decentring distortion obtained in Calibration 2 Sensor 1 (C2(S1)) and Calibration 2 Sensor 2 (C2(S2)) and the difference obtained for C2(S1) – C2(S2).

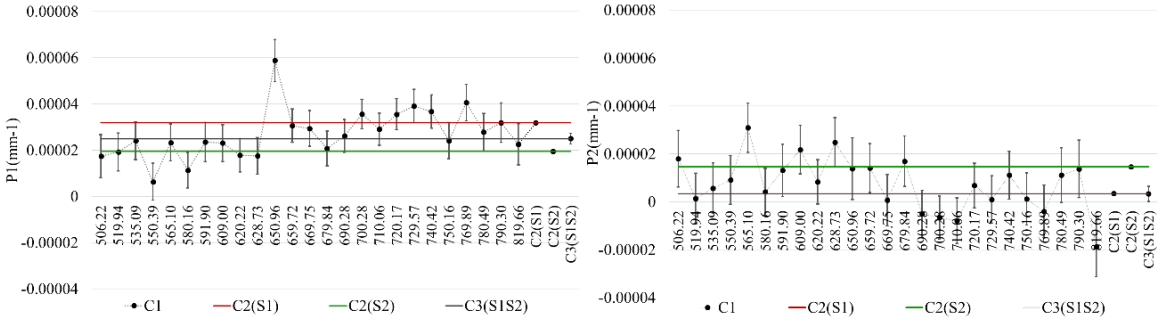

(a) (b)

Table 3 shows the minimum and maximum values as well as the average and standard deviation of the IOPs estimated for Calibration 1, separated according to each sensor. As can be seen, Sensor 1 presented the largest variations in the estimated values.

Table 3: Statistics for the 25 sets of IOPs estimated for Calibration 1, split by sensor: minimum and maximum values and the averages and standard deviations for each group of IOPs.

	Bands of Sensor 2				*Bands of Sensor 1*			
	Min	*Max*	*Average*	*σ*	*Min*	*Max*	*Average*	*σ*
c(mm)	8.6611	8.6727	8.6668	0.0040	8.7022	8.7223	8.7106	0.0056
x_0(mm)	-0.0051	0.0079	0.0033	0.0036	-0.0531	-0.0332	-0.0425	0.0048
y_0(mm)	-0.2797	-0.2715	-0.2771	0.0024	-0.3089	-0.2958	-0.3035	0.0035
k_1(mm^{-2})	-0.004265	-0.004066	-0.004139	6.032E-05	-0.004654	-0.004279	-0.004546	9.879E-5
k_2(mm^{-4})	-1.9635E-5	1.5422E-5	-6.9947E-6	1.105E-5	-6.3901E-5	1.2535E-5	-1.2333E-5	2.147E-5
k_3(mm^{-6})	-1.3968E-6	8.2658E-7	-2.3269E-7	6.479E-7	-2.5363E-6	3.0092E-6	-7.105E-7	1.531E-6
P_1(mm^{-1})	6.3253E-6	2.4049E-5	1.8362E-5	5.797E-6	2.0705E-5	5.8764E-5	3.2582E-5	9.383E-6
P_2(mm^{-1})	1.3723E-6	3.091E-5	1.3711E-5	9.796E-6	-1.8805E-5	1.6952E-5	3.2154E-6	1.036E-5

The similarities between the IOPs from the different calibrations were assessed by considering the IOP sets for each sensor (the results from Calibration 2) and their respective bands (the results from Calibration 1) using statistical testing (Equation 2). For a 95% confidence level and degrees of freedom higher than 1500, the critical value for Student's t distribution is approximately 2. Thus, significance values higher than 2 (approximately) indicated a rejection of the null hypothesis (H_0: $parameter_{BAND} = parameter_{SENSOR}$), which means that the value for the parameter under analysis, estimated for a certain band in Calibration 1, was statistically different from the

corresponding value for parameter estimated for the sensor in the experiment Calibration 2.

Figure 18 (a) shows that, for Sensor 2, the significance values were higher than 2 for parameters c and y_0, for two bands (550.39 nm and 565.10 nm; 550.39 nm and 580.16 nm). Significance values achieved for Sensor 1, were higher than 2 for the following parameters and respective bands: (1) c parameter, for the last three bands; (2) x_0 parameter, for 690.28 nm and 780.49 nm bands and (3) y_0 parameter for 780.49 nm band. The first band of Sensor 1 obtained significance value higher than 2 for the three radial distortion parameters.

Figure 18: Significance (Student's t statistics) of the parameter differences obtained for (a) the IOPs for the Sensor 2 bands estimated for Calibration 1 (C1), and the IOPs for Sensor 2 (C2(S2)); (b) the IOPs for the Sensor 1 bands estimated for Calibration 1 (C1), and the IOPs for Sensor 1 (C2(S1)).

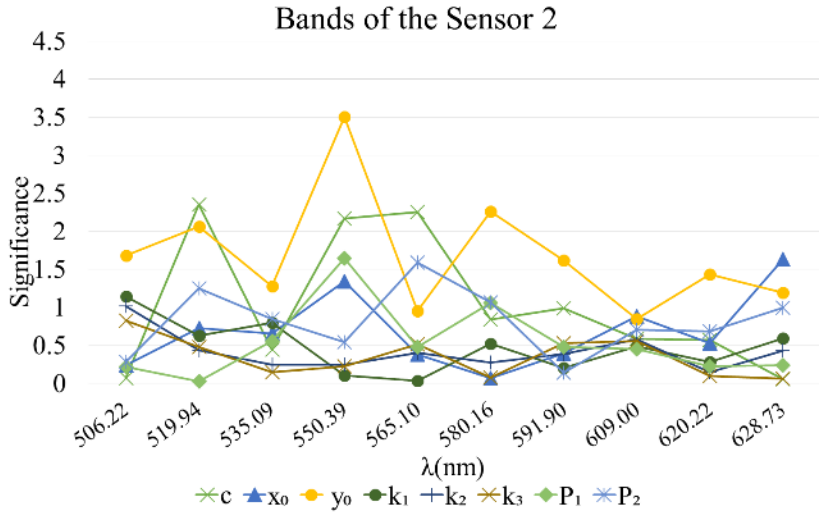

(a)

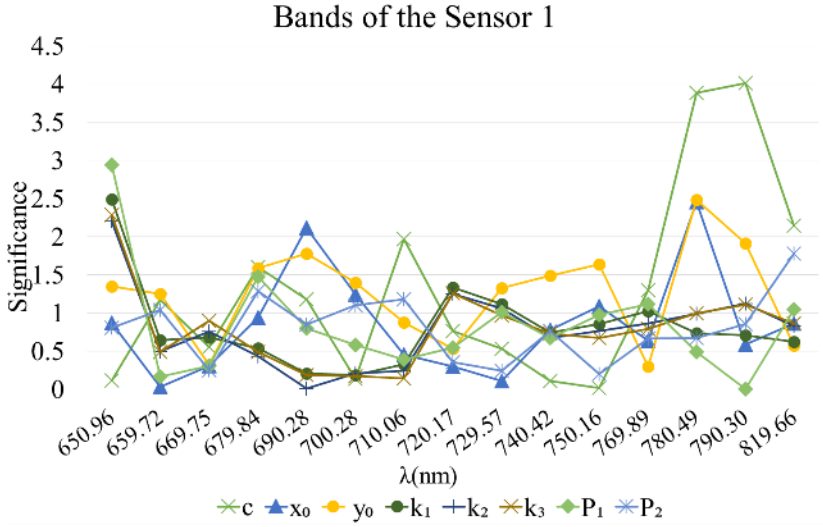

(b)

The statistical test applied for the IOP sets estimated for each sensor in Calibration 2 resulted in significance values from 12 to 163 for the parameters, excepted for k_2 with significance of 0.89, indicating that the IOPs for Sensors 1 and 2 were statistically different. Exceptions were minor, thus the result suggests that the sensor-related calibrations provided IOP which were suitable for the individual bands.

The ZROT method was used to assess the similarity of estimated IOPs of the individual bands with IOPs for each sensor (1 and 2). The RMSE values for Sensor 2 (Figure 19 (a)) ranged from 0.48 to 7.4 μm in the x direction and ranged from 2.67 μm to 10.93 μm in the y direction, with five bands having RMSEs smaller than one pixel in both directions. The $RMSE_{ZROT}$ values for Sensor 1 (Figure 19 (b)) ranged from 0.51 μm to 12.19 μm in the x direction and from 1.02 to 8.01 μm in the y direction, where twelve bands obtained RMSE in x and y equal or smaller than one pixel x and y. The largest $RMSE_{ZROT}$ values for both sensors occurred in the bands 550.39 nm and 780.49 nm, same bands as the rejected null-hypothesis in the IOP c and x_0 of the statistical test.

Furthermore, the $RMSE_{ZROT}$ for the IOPs obtained for each sensor in Calibration 2 were 45.79 μm in the x direction and 18.97 μm in the y direction. Regarding the IOPs estimated for Calibration 3, the $RMSE_{ZROT}$ obtained by comparing the Calibration 2 (S1) were 18.58 μm in x and 7.98 μm in y, with Calibration 2 (S2) the $RMSE_{ZROT}$ was 27.13 μm in x and 10.96 μm in y (not shown in Fig. 10).

The results of ZROT method thus presented discrepancies larger than the expected image measurement errors (1/2 - 1 pixel), as suggested by Habib et al. (2006), for most bands. Fixing both the IOPs and EOPs caused these discrepancies in the ZROT. They could be caused by residuals errors and correlations in the IOP and EOP determination, or they could be due to physical differences of IOPs of different bands, caused by sensors misalignment and small changes in the optical paths caused by the FPI.

Figure 19: Results when using the ZROT method. RMSEs obtained for: (a) the IOPs for Sensor 2 bands estimated in Calibration 1 (C1) and IOPs for Sensor 2 (C2(S2)); (b) the IOPs for the Sensor 1 bands estimated in Calibration 1 (C1) and the IOPs for Sensor 1 (C2(S1)).

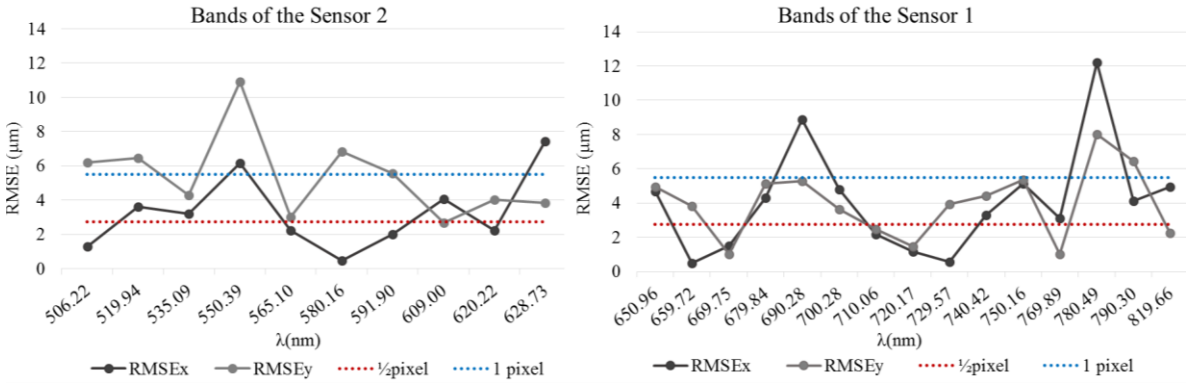

(a) (b)

The similarities between the sets of IOPs related to Sensor 2 (C2(S2)) were assessed considering the IOP sets for the bands of the Sensor 1 and the IOPs of the Sensor 1 (C2(S1)) were compared with the bands of the Sensor 2 (the results from Calibration 1) using statistical testing (Figure 20) and the ZROT method (Figure 21). Regarding the statistical testing, the parameters c, x_0, y_0, and k_1 of the bands were statistically different from the parameters estimated for the different sensors. However, the distortion parameters k_2, k_3, P_1 and P_2 presented significance values smaller or slightly higher than 2. Considering ZROT test, RMSEs vary from 36.8 mm to 57.6 mm, in x direction and from 13.8 mm to 29.9 mm, in y direction, which indicates a high difference between the IOPs.

Figure 20: Significance (Student's t statistics) of the parameter differences obtained for (a) the IOPs for the Sensor 2 bands estimated for Calibration 1 (C1), and the IOPs for Sensor 1 (C2(S1)); (b) the IOPs for the Sensor 1 bands estimated for Calibration 1 (C1), and the IOPs for Sensor 2 (C2(S2)).

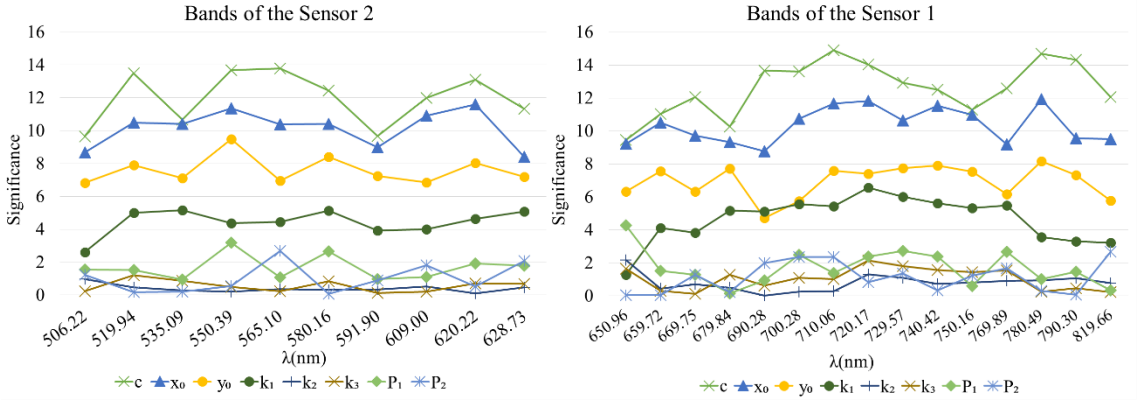

(a) (b)

Figure 21: Results when using the ZROT method. RMSEs obtained for: (a) the IOPs for Sensor 2 bands estimated in Calibration 1 (C1) and IOPs for Sensor 2 (C2(S2)); (b) the IOPs for the Sensor 1 bands estimated in Calibration 1 (C1) and the IOPs for Sensor 1 (C2(S1)).

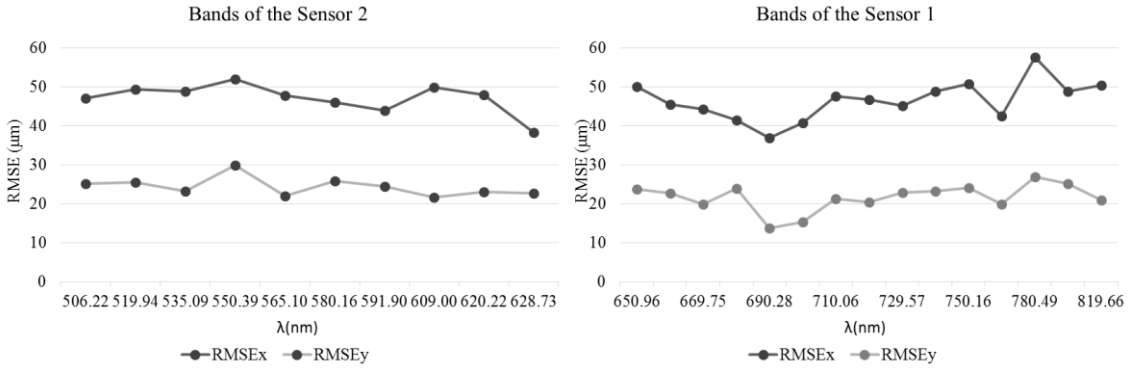

(a) (b)

The results indicate two predominant and distinct sets of IOPs for Sensor 1 and Sensor 2. In addition, slight variations in the values for each band in the same sensor can be observed. The values of the IOPs obtained for Calibration 2 were similar to the sensor-related average values calculated during Calibration 1; Calibration 3 yielded values similar to the overall average for Calibrations 1 and 2.

4.4 Discussions and conclusions

Comparing the results of the previous experiments with those presented in Oliveira et al. (2016a) the RMSEs on the residuals of the image coordinates (Figure 12) have decrease for all experiments and mainly for the bands of Sensor 2. This reduction can be related to the corner detection process, which can vary along the bands due to differences in saturation and contrast, depending on the illumination used. The use of the centroid of the corner points instead of corner points has probable reduced this effect for the presented results.

ZROT method simulates the situation when using the camera indirect georeferencing mode. The results suggested that using sensor-wise IOPs instead of band-wise IOPs could cause discrepancies on the level of 0.09–2 pixels. These results suggest that a per-band adjustment based approach is necessary in order to obtain the highest accuracy, but, depending on the project type, using two sets of IOP, one for each sensor, would suffice.

The FPI camera can be accurately calibrated via self-calibrating bundle adjustment with the Conrad-Brown distortion model, which is the most common approach for distortion modelling implemented in commonly used photogrammetric software. The different experiments were conducted to analyze the IOPs similarity along different bands and sensors and the results showed that the variations in the spectral sensitivity caused by the air gap of the FPI did not significantly affect the IOP values. Thus, a single set of IOPs can be used for each sensor because differences in the IOPs for each sensor were found to be significant, and consequently, it can be concluded that it is more suitable to determine the IOPs individually for each sensor.

The analysis of the standard deviations for the estimated IOPs indicated that the panel with Aruco targets provided suitable accuracy for the sensor calibration since a suitable geometric configuration is used for images acquisition.

5. ASSESSEMENT OF BAND 2D CO-REGISTRATION PERFORMANCE

Acquisition of different wavelengths is performed by changing the air gap of the FPI. Because of the acquisition principle, in the FPI camera system, the spectral bands of the cube do not overlap perfectly when the system is moving. In other words, images corresponding to different spectral bands of the same data cube have different positions and orientations, thus a registration process among the bands is required. This chapter is based on conference papers presented by Oliveira and Tommaselli (2014b) and Tommaselli et al. (2015) and deals with the problem of band registration.

2D co-registration of the bands was used to perform the image classification, to be used as information for tuning the parameters of the image matching techniques presented in Chapter 7.

5.1 Experimental assessment

The aim of this set of experiments is to analyze the impact of two-dimensional geometric transformations on the co-registration of spectral bands from the same hypercube acquired with the FPI camera. The transformations were performed using Helmert, affine, projective and second order polynomials. Two data sets from different cameras and configurations were used. The first data cube was acquired with the FPI camera prototype 2012b, carried by an octocopter RPAS helicopter from FGI (HONKAVAARA et al., 2013). The area of the flight was located in Evo, Finland and the approximated GSD was of 15 cm. The images used in this case study have 1024x648 pixels and 27 bands, but only 16 bands were selected and only one band was used as reference in this study.

The second data set was acquired by the FPI camera 2014 in the 3D terrestrial calibration test field at Unesp, Presidente Prudente - Brazil. The FPI camera was installed over a pallet carrier and distance from the camera to the wall with coded targets was 6.9 m. The platform was moved at 0.16 m/s and 0.55 m/s, in order to

produce apparent speeds comparable to flights with RPAS speeds of 3.4 m/s and 11 m/s, respectively, for a flying height of 150 m. The camera was configured to acquire 25 bands (1023x648 pixels), and five bands were selected for the registration assessment, taking one as reference band (band 13). Three conditions were analyzed: (1) camera static; (2) camera moving over flat terrain; (3) camera moving over terrain with height variations.

Figure 22 shows the displacement among the bands, due to the camera acquisition movement, for the two scenarios (a) Finnish forest Evo and (b) Unesp's 3D terrestrial calibration field. The difference between the pixels of the same object in (a) can be greater than 60 pixels, which corresponds to more than 9 m in the field.

The effect of platform movement in the band registration, with different camera versions, can be seen in Figure 22 (a) and (b), the former being acquired by an RPAS in Finland and the latter in a terrestrial calibration field in Brazil. This effect is highly dependent on platform speed, distance to the object and relief displacement.

Figure 22: Band misregistration due to platform movement: (a) spectral aerial image collected by an RPAS and: (b) terrestrial images of a calibration field with coded targets, collected with a moving platform simulating the same apparent speed of an RPAS.

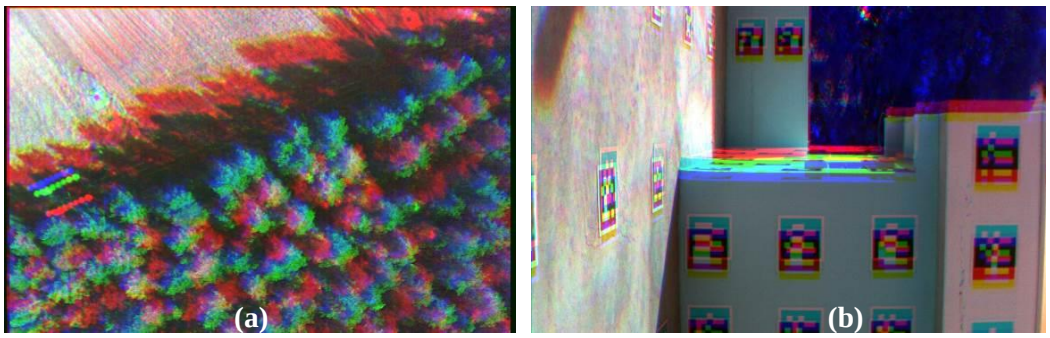

For the two data sets, extraction of the interest points for the calculation of the transformation parameters was carried out using Förstner operator. Distribution of points, presence of spurious points and correctness of point detection and matching in all bands were carefully verified during this step. Only the central band of the cube was used as a reference, to minimize the time/position difference between bands. The parameters of the geometric transformations were estimated and results were assessed with 9 independent check points.

5.2 Experiments and results of 2D co-registration

Table 4 shows the 16 spectral bands used for the Evo data set, the time and space difference for acquisition between each band and the reference band (band number 6). Based on the average platform speed of 5 m/s, for example, the displacement between the camera centers from the reference band 6 to band 18 was 3.75 m.

Table 4: Band number and temporal and spatial differences in Evo forest data set.

n. Bands	13	14	15	16	17	3	4	24	***(Ref) 6***	8	11	7	10	23	5	18
Gap (nm)	591	611	631	652	836	409	434	1225	447	525	545	466	538	1204	441	884
dt to Ref(s)	-0.83	-0.75	-0.68	-0.6	-0.53	-0.15	-0.08	-0.08	0	0.075	0.15	0.3	0.45	0.45	0.6	0.75
ds to Ref(m)	-4.125	-3.75	-3.375	-3	-2.625	-0.75	-0.375	-0.375	0	0.375	0.75	1.5	2.25	2.25	3	3.75
ds pixels	41.25	37.5	33.75	30	26.25	7.5	3.75	3.75	0	3.75	7.5	15	22.5	22.5	30	37.5

Image coordinates of 24 points were used to estimate the corresponding parameters of the four 2D geometric transformations (Helmert, affine, projective and 2nd order polynomial), for each pair formed between the reference band and the other 15 bands. The estimated parameters were used to calculate the inverse transformation, back-transforming the image coordinates of the checkpoints. Figure 23 shows the distribution of the control and check points. Table 5 shows the RMSE of the residuals in the column and row coordinates obtained in all bands, with each transformation, for: (a) the 24 points used in the calculation of the parameters and (b) the RMSE resulting from the differences between 9 check points in each band after performing the inverse transformation. The highest RMSE values in the differences occurred when using the 2D Helmert transformation, with RMSE over 4 pixels in the resultant of column and row components, for the bands more spatially distant from each other. The smallest RMSEs were obtained in 2D projective and 2nd order polynomial, and were smaller than 3 pixels.

Figure 23: Image of band 447. (a) Location of control points and (b) check points.

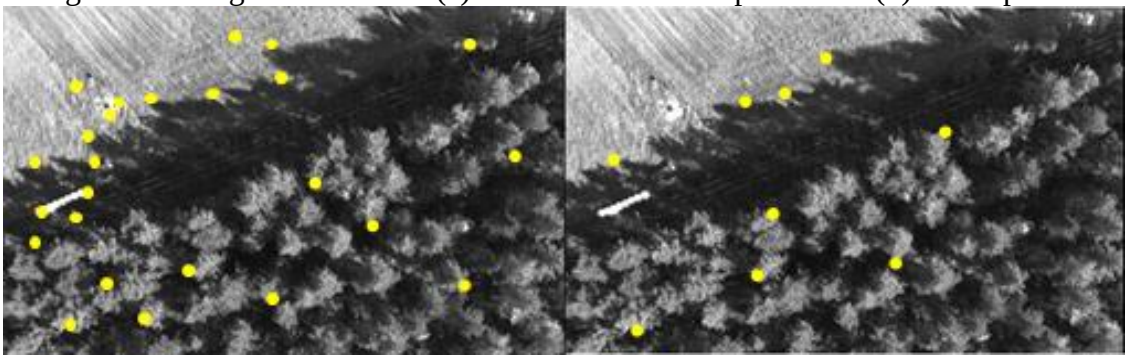

Table 5: RMSE of the transformation (a) control points and (b) check points.

a. Control Points

Transformation	*RMSE COL(pixel)*	*RMSE ROW(pixel)*	*RMSE Resultant(pixel)*
Helmert	1.773	1.669	2.435
Affine	0.843	0.955	1.274
Projective	0.657	0.924	1.134
Polynomial 2nd order	0.601	0.788	0.991

b. Check Points

Transformation	*RMSE COL(pixel)*	*RMSE ROW(pixel)*	*RMSE Resultant(pixel)*
Helmert	2.158	2.251	3.119
Affine	1.139	1.474	1.863
Projective	0.990	1.386	1.703
Polynomial 2nd order	0.947	1.089	1.444

In order to observe the behaviour of the registration along the bands, Figure 24 shows the RMSE of the differences in column and row of the 9 check points for each band, after performing the inverse transformation of (a) the Helmert and (b) the polynomial transformation. The largest RMSEs were obtained in the row coordinates, which occurs due to the effect of parallax caused by the combined effect of the aircraft movement during band acquisition and relief displacement. The difference in spectral response between the bands also influenced the registration process and not only the different acquisition time. This may occur due to the radiometric differences between the bands, making the precise measurement of homologous points more difficult. In this camera model, the bands n. 24 (1225 nm) and n. 4 (434 nm), for example, were acquired at the same time, however, due to the radiometric differences from the reference band, the discrepancies were higher for band n. 24.

Figure 24: RMSE for all bands (a) Helmert and (b) polynomial *2nd order* transformation.

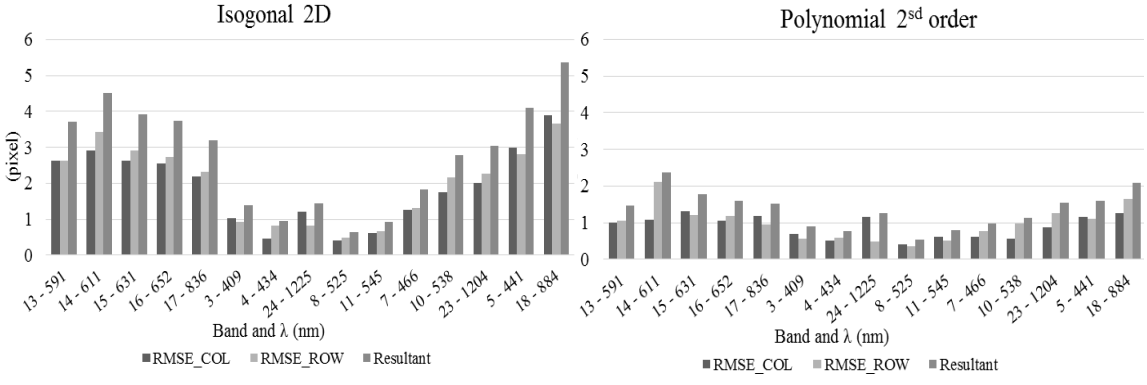

(a) (b)

Table 6 presents the bands selected in the 3D terrestrial field data set, where Bands 1 and 7 were acquired by sensor 2 while bands 13, 19 and 25 were acquired by sensor 1. In this case, the parameter transformations were estimated only with the affine transformation and second order polynomial. The experiments were performed considering: (a) static camera; (b) low speed (0.16 m/s) and higher speed (0.55 m/s). The configuration of control points was variable and three scenarios were considered: (a) control points over a flat area; (b) control points with depth variations of 1 m, 10% of the camera distance; and (c) depth variation of 3 m, 30% of the camera distance.

Table 6: Selected bands of RIKOLA DT camera and their differences in position (ds) and time of acquisition (dt) with respect to a reference band (13).

Band n°		**1**	**7**	**(Ref) 13**	**19**	**25**
λ (nm)		506.07	592.78	669.96	729.56	819.74
dt to RefBand (s)		-0.4	-0.17	0	0.17	0.4
ds to RefBand v = 0.55 m/s	cm	- 22.00	-9.35	0.00	9.35	22.00
	pixels	-54.24	-23.05	0.00	23.05	54.24
ds to RefBand v= 0.16 m/s	cm	-6.40	-2.72	0.00	2.72	6.40
	pixels	-16.13	-6.86	0.00	6.86	16.13

Table 7 presents the RMSE of the image coordinate residuals in the control points. RMSEs were computed separately for points located in flat area and in an elevated area. The differences between affine and polynomial transformations for the flat area were smaller for bands taken by the same sensor of the reference band (19 and 25). The polynomial function was more suitable when considering bands of sensor 2 (1 and 7) to band 13 (sensor 1), probably because it can absorb the misalignment between the two sensors and other distortions. In general, the magnitudes of residuals is still subpixel when the control points are over a flat surface.

Bearing in mind that the camera is moving, the parallax effect can be seen in the RMSE of the control points with depth variations. For instance, when the camera is moving at 0.16 m/s (Table 7 (b)), the registration of bands acquired at the beginning and end of the cube (1 and 25) produced an RMSE larger than 1 pixel for affine transformation, but they were still near 1 pixel for the polynomial model. The results with the camera moving at 0.55 m/s (Table 7 (c)) showed that, in flat areas, the bands can be co-registered with sub-pixel accuracy. However, in areas with slope variations around 30% of the camera distance (3 m), the parallax effect produced RMSE from 5.6

to 12.5 pixels with affine transformation and from 2.0 to 3.6 pixels for polynomial transformation.

Table 7: RMSE (in pixels) in control points in a flat area and controls points with 1 m of depth variation (a) for band pairs with static camera, (b) with camera moving at 0.16 m/s and (c) (b) with camera moving at 0.55 m/s.

a. Camera static

	Flat area				10 % of depth variation			
Transformation\Bands	**1**	**7**	**19**	**25**	**1**	**7**	**19**	**25**
Affine	0.45	0.43	0.20	0.30	0.74	0.72	0.33	0.38
2nd order Polynomial	0.36	0.36	0.19	0.28	0.64	0.60	0.33	0.34

b. Camera moving at 0.16 m/s

	Flat area				10 % of depth variation			
Transformation\Bands	**1**	**7**	**19**	**25**	**1**	**7**	**19**	**25**
Affine	0.54	0.57	0.33	0.37	1.21	0.98	0.70	1.63
2nd order Polynomial	0.38	0.36	0.27	0.29	0.76	0.72	0.48	0.90

c. Camera moving at 0.55 m/s

	Flat area				30 % of depth variation			
Transformation\Bands	**1**	**7**	**19**	**25**	**1**	**7**	**19**	**25**
Affine	0.43	0.72	0.41	0.43	11.0	5.60	6.18	12.50
2nd order Polynomial	0.19	0.22	0.30	0.19	3.60	2.08	1.88	3.33

5.3 Discussions and conclusions

The results considering both aerial and laboratory/terrestrial image data sets showed that several problems can be expected in the band co-registration of spectral frame cameras with tuneable FPI. As expected, the experiments revealed that camera displacements during bands acquisition, cause significant parallax effects, depending on the relief variations, and, in some cases, the co-registration with 2D transformations will be unreliable. Other effects in this process are caused, for instance, by the difficult to find homologous point due to the different spectral responses of the targets.

Possible solutions are reducing the flight speed depending on the object height variations or adjusting the GSD output to meet the registration accuracy. A potential alternative is the use of pixel to pixel discrete mapping, based on 3D models and relative orientation, which can be compared to orthorectification.

6. GEOMETRIC PROCESSING OF HYPERSPECTRAL IMAGES

This chapter presents the image orientation experiments and the results of different photogrammetric image blocks, acquired by hyperspectral 2D frame cameras in tropical forest areas (Ponte Branca, Brazil) and a boreal forest area (Vesijako, Finland). Surveying of control points and BBA of images to obtain the EOP were carried out for the completion of the experiments. It is important to emphasize that the quality of the EOP is fundamental for the whole process of DSM generation. Processing was performed using a commercial software Agisoft Photoscan (Agisoft Photoscan, 2017), based on SfM, and the in-house software CMC, which is based on least-squares adjustment (combined model) with constraints.

6.1 Material

6.1.1 Carrier platform and imaging system

The platform SX8 is an RPAS hexacopter multi-rotor, designed and assembled by the Sensormap company, Brazil. This multi-rotor SX8 was equipped with an FPI camera model 2015 (subsection 2.1.2), a Sony Nex7 (RGB) camera and a dual-frequency GNSS receiver (Novatel SPAN-IGM) (Figure 25). The total weight of this payload is approximately 4 kg. The flight time can vary from 15 to 30 min depending on the batteries and the payload weight.

Camera triggering and event recording was implemented with an on-board system, which is a light version of an existing aerial acquisition system SAAPI (RUY et al., 2009). This system was simplified to have less payload weight. GNSS-INS is synchronized to record positions and attitude angles in every exposure of the FPI camera (georeferencing every band of the cube) and RGB camera.

Figure 25: The hexacopter SX8 with INS system, RGB and FPI camera.

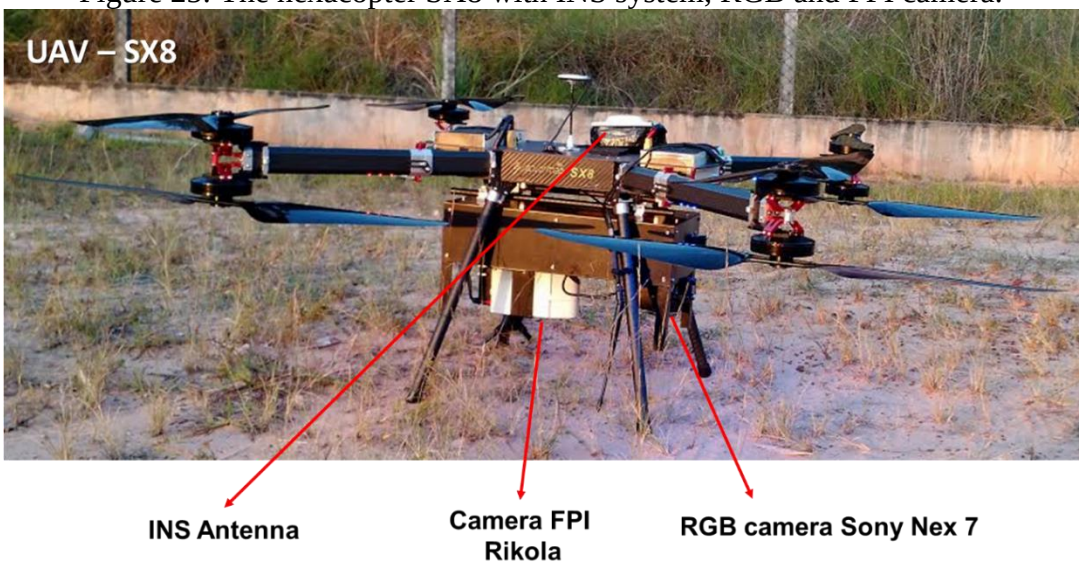

6.2 Field work

Data collection in environments such as the Brazilian rainforest is not a simple task. It is hard to enter and walk through the forest due to the high density of plants, branches and lianas, as shown in Figure 26 (a) and (b). In addition, there are wild animals such as Brazilian jaguars, wild pigs and poisonous snakes. The large number of tree species hampers the process of measuring the heights of individual trees using conventional field measurement tools.

The field works can be divided into two types of campaign: inside and outside the forest. Inside the forest, the field works were conducted to collect data in sample areas that can characterized successional stages of the Ponte Branca fragment. Six sample areas (or plots) of 40 by 40 meters and one transect (450 m x 10 m) were surveyed (Figure 27). All trees with trunk diameter greater than 3.8 cm (or circumference ≥ 12 cm) were identified and had their species scientific name and their diameter at breast height (DBH) recorded. The plot corners were also surveyed using a dual frequency GNSS receiver. It is at best difficult but usually quite impractical to establish GCPs inside dense forests that are visible from aerial images. Figure 26 (c) shows an example of the view above ground in such environment. The lack of open areas reduces the viability of using GNSS receivers to collect control points (due to loss of cycle and multipath). However, some points were surveyed, whenever possible, within the study area Figure 26 (d) with at least one hour of recording GNSS signals.

The campaigns outside the forest involved the establishment of GCPs for the image block orientations, which were signalized with artificial targets. In the areas of Plots 4, 5 and 6 and Plot 1 and 3 (Figure 27), land marks were installed (Figure 26 (e)).

Figure 26: Field work conditions in Ponte Branca forest area (a) and (b) characteristics of the dense vegetation between trees, (c) view of the sky, (d) GNSS surveying of points within the forest, (e) land mark installed outside the forest and (f) reference station outside forest.

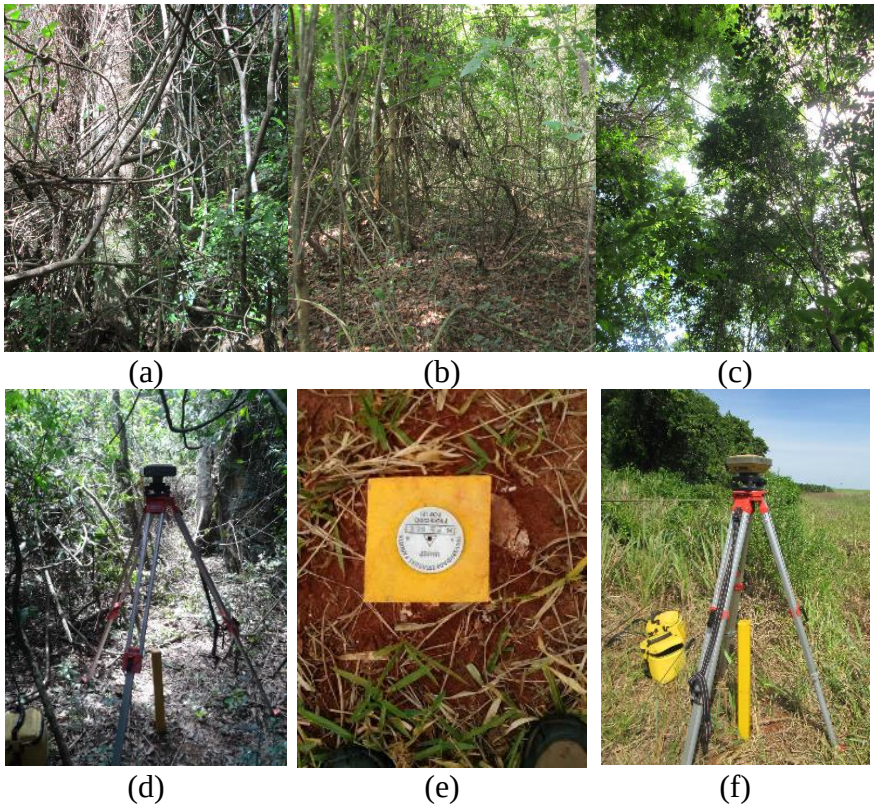

(a) (b) (c)

(d) (e) (f)

In each campaign, a base station receiver was set at a point outside the forest (Figure 26 (f)) to collect data throughout the survey time inside the forest and during the RPAS flight. This point was used as a reference station for the relative GNSS data processing. Dual frequency Hiper GGD and Hiper SR GNSS receivers were used for the survey. The collection rate was 5 seconds and 10° elevation mask. The points were processed using the relative positioning method and the Inertial Explorer® software. The points used as reference were processed using an RBMC-IBGE (*Rede Brasileira de Monitoramento Contínuo dos Sistemas GNSS*) database, obtaining a millimeter estimated precision. Points surveyed within the forest have lower quality (σ = 0.5 m or higher), even with the collection lasting more than an hour in some cases.

Figure 27 presents the approximate location of the measured sample areas and the set of control points. It is worth noting that the fieldwork campaigns were strictly

related to the UAV-4D-Bio project, with several project members working. In addition, a local forest inhabitant was essential to prepare possible access and paths inside the forest and to identify the popular name of the trees species. Only the GNSS data was used because detailed description of tree species was not subject of this study. Details of the data collected within the plots are better described in Berveglieri et al. (2016).

Figure 27: Approximate location and distribution of sample areas and ground control points in Ponte Branca, Brazil. Source: Google Earth.

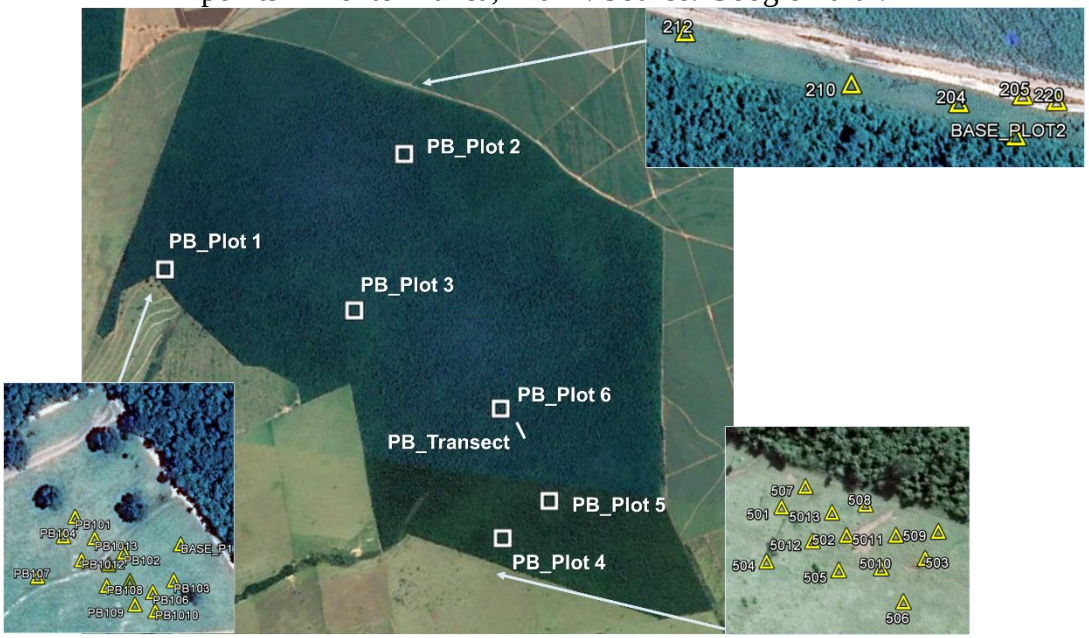

6.3 Flight campaigns

The SX8 RPAS (Figure 25) was equipped with the RGB and FPI camera and a dual-frequency GNSS receiver (Integrated to a Novatel SPAN-IGM Inertial Navigation System) to acquire the image blocks with two strips. The FPI camera was configured with the spectral bands presented in Table 2, and integration time of 10 ms. This integration time can vary depending on weather conditions and illumination. Before carrying out the flight, artificial targets were positioned along the border of the test area, some of them over the surveyed GCPs. A preprogrammed flight plan was flown autonomously using autopilot DJI, but takeoff and landing were carried out manually for safety reasons.

Image blocks were collected in three areas of the Ponte Branca fragment, and covered six plots and the transect (Figure 27). The three flight missions were carried out with a flight speed of 4 m/s and at height of 160 m, which generated spectral images

with a GSD of approximately 9 cm. Forward overlap was approximately 80% and side overlap was 50%. The image blocks PB1 (covering Plots 4, 5 and 6) and PB3 (covering Plots 1 and 3) consisted of two flight lines while the block PB2 (Plot 2) had only one. The resulting GSD was about 9 cm for the FPI camera. For the RGB camera, the GSD was about 3 cm. Ground points arranged in each block were surveyed with double frequency GNSS receivers. A reference station was settled in the area and a double frequency receiver collected data during the flight mission.

The FPI camera 2015 was configured with the same parameters used for the calibration experiments (Table 2). The time difference between each band acquisition in is showed in Figure 28. This information can be precisely computed using a spreadsheet (SequenceInfoTool), supplied by the FPI camera manufacturer, Rikola, which provides the time difference between spectral bands. The difference from the first to the last band is about 0.899 s, which corresponds to a shift of 3.6 m, for a flight speed of 4 m/s. It can also be seen that the highest difference of acquisition time, between two bands, is found in the last band of Sensor 2 and the first band of Sensor 1.

Figure 28: Time difference (ds) in seconds between the bands of a cube in FPI camera 2015 for a flight speed of 4 m/s. Red line indicates the ending of Sensor 2.

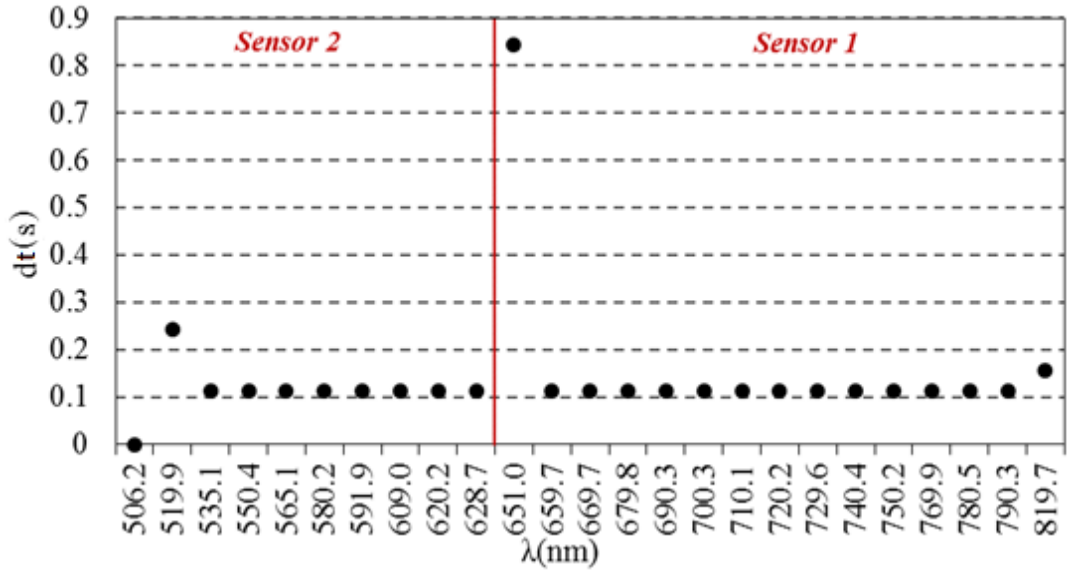

The test area located in Vesijako, Finland (N 61°21’40”, E 25°6’4”) was flown using a Tarot 960 hexacopter during the full-leaf season. The FPI camera prototype 2012b was used. The camera was configured with 36 bands of 1024 × 648 pixels and the details of the band configuration are shown in Table 8. An image block with six image strips and 97 hyperspectral data cubes was captured at the flight height of 88 m

above ground level; at tree tops the object distance was an average 67 m. The average GSD varied from 6.7 to 8.8 cm and the forward and side overlaps were 65% and 57% at ground level. The flight speed was 4.6 m/s and the resulting distance between first and last exposures of a single cube was 8.3 m. The spatial difference between each band of Vesijako data, considering the speed of 4.6 m/s, is presented in Figure 29. It can be seen that some bands are acquired at the same time, because of the type of sensor and filter used in this camera (Section 2.1.2).

Table 8: Air gaps, central wavelengths, full width of half maximum (FWHM) and time difference of the bands used in the FPI camera prototype 2012b for Vesijko flight.

λ(nm)	507.6	509.5	514.5	520.8	529	537.4	545.8	554.4	562.7	574.2	583.6	590.4	598.8
	605.7	617.5	630.7	644.2	657.2	670.1	677.8	691.1	698.4	705.3	711.1	717.9	731.3
	738.5	751.5	763.7	778.5	794	806.3	819.7	833.7	845.8	859.1	872.8	885.6	
FWHM (nm)	11.2	13.6	19.4	21.8	22.6	20.7	22	22.2	22.1	21.6	18	19.8	22.7
	27.8	29.3	29.9	26.9	30.3	28.5	27.8	30.7	28.3	25.4	26.6	27.5	28.2
	27.4	27.5	30.5	29.5	25.9	27.3	29.9	28	28.9	32	30.8	27.9	
dt(s)	0.9	0.975	1.05	1.125	1.2	1.275	1.35	1.425	1.5	1.575	1.65	1.725	1.8
	0	0.075	0.15	0.225	0.3	0.375	0.45	0.525	0.6	0.675	0.75	0.825	0.9
	0.975	1.05	1.125	1.2	1.275	1.35	1.425	1.5	1.575	1.65	1.725	1.8	

Figure 29: Spatial difference (ds) in meters between the bands of a cube in the FPI camera prototype 2012b (FGI).

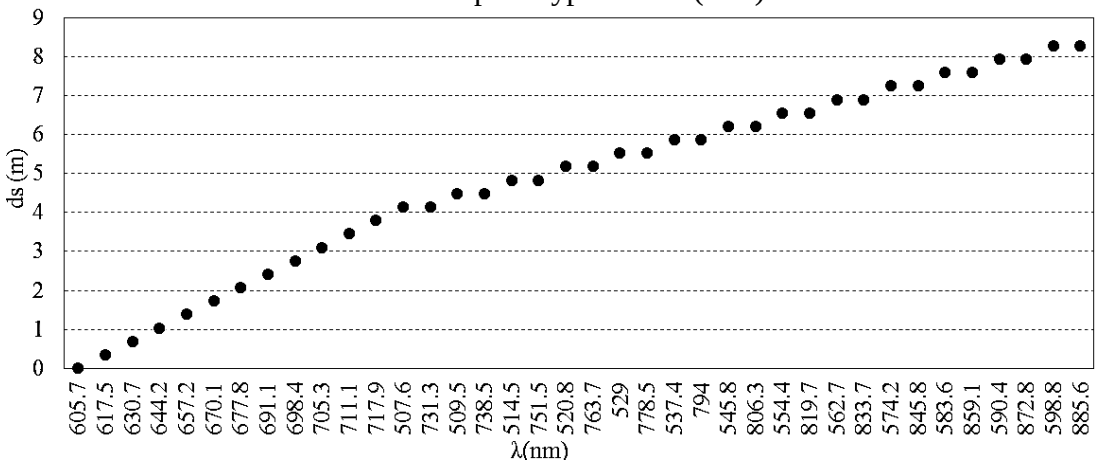

The flight lines and location of the image blocks in Ponte Branca and in Vesijako are presented in Figure 30. The forward and side overlaps of FPI images in Ponte Branca were 80% and 50%, respectively (Table 9). The PB2 flight had almost no side overlaps, because it was intended to cover two plots using the same flight, for safety and time slot reasons.

Table 9: Information of the flights over the Ponte Branca and Vesijako areas.

	Date	Overlaps	Flight height	Weather	Coverage area km²
PB1 (Plot 5 and 6)	08.09.2016	80%;50%	160 m	Cloudy	0.236
PB2 (Plot 2)	08.16.2016	80%; 0%	160 m	Sunny	0.39
PB1 (Plot 1 and 3)	08.16.2016	80%; 50%	160 m	Sunny	0.238
Vesijako	06.26.2014	53%;43%	88 m	Sunny	

Figure 30: Flight lines and image blocks (a) PB1 (Plots 5 and 6), (b) PB3 (Plots 1 and 3), (c) PB2 (Plot 2) and (d) Vesijako, Finland.

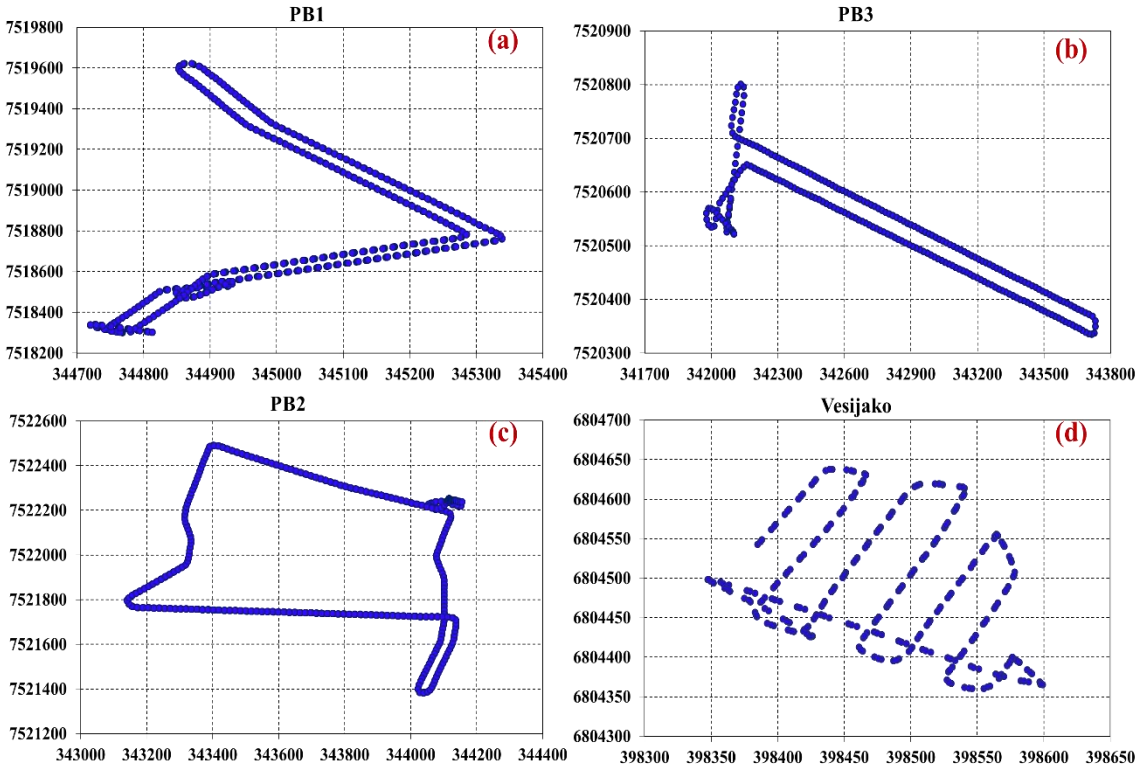

6.4 Image orientation

The determination of exterior orientation of images from hyperspectral 2D frame cameras can be made by techniques similar to those used for images coming from frame format cameras. When the image cube is formed by a set of non-registered spectral frame bands, the bands can be oriented separately, as single frame images. The determination of orientation parameters becomes more complex with non-registered hyperspectral image blocks in forest areas because each band will have 6 EOPs. A further problem is that acquisition of GCPs is not easily feasible or assessable in tropical forest scenarios due to dense vegetation and only a few presignalized targets or natural points outside the forest or in clearings can be used as control points. In addition

to that, considering the RPAS operation time and the length of the forest area, the flight has to be designed as “two-strip”, taking-off and landing in the same area. As can be seen in Figure 31, the control points in the Ponte Branca image blocks are concentrated only on one side of the area, which is not the best geometry for photogrammetric blocks.

Figure 31: Geometry of image blocks and GCPs location.

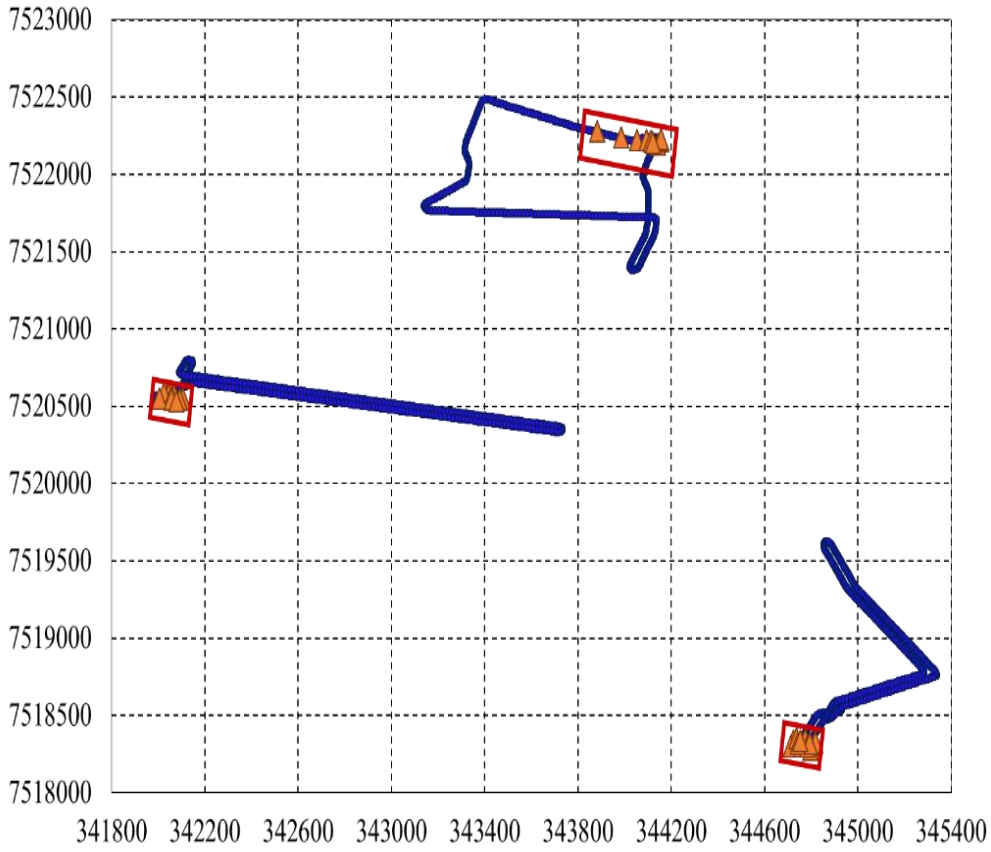

Considering these real scenarios, the importance of rigorous modelling of IOP, direct georeferencing and good block geometry is clear. Several software packages are available to perform 3D reconstruction based on SIFT correspondence and SfM algorithms (REMONDINO et al., 2014).

A preliminary study showed that the FPI camera could provide accurate data when using more flight lines, rigorous model for IOP, GNSS data from direct georeferencing and GCPs. This study was performed with FPI camera data collected in a parking area called Morada de Deus, in Álvares Machado, São Paulo State. The FPI image block was collected with a flying height of 100 m, forward overlap of approximately 60% and side overlap from 10% to 20%. The commercial Agisoft

PhotoScan (AgiSoft LLC, St. Petersburg, Russia) software was used to estimate image orientation and generate 3D point clouds for the FPI blocks. The use of this software has been validated in previous studies (REMONDINO et al., 2014; NÄSI et al., 2015). This software performs 3D reconstruction SfM and dense image matching based on the SGM method.

The double frequency GNSS receiver of the Novatel SPAN-IGM-S1 on-board the RPAS recorded raw data with a frequency of 1 Hz. A reference station in the area was collecting data during the flight using a double frequency receiver. The trajectory was computed with Inertial Explorer software. In this flight, the INS (Inertial Navigation System) system was not yet synchronized with the camera acquisition events. Thus, the position of each band was interpolated using the time difference between the bands computed by the Rikola SequenceInfoTool and the GPS time of the first band grabbed by the Rikola GPS. The interpolated coordinates of the perspective centers could be used as observations in the bundle adjustment, but the attitude angles provided by the INS could not be inserted, except as approximated values, because the boresight misalignment angles had not be previously determined. A total of twenty-four ground points were surveyed with double frequency GNSS receivers; ten of these points were used as control and fourteen as check points.

Figure 32 presents the RMSEs in the GCPs and check points coordinates obtained in the on-the-job calibration process, using one band and using three bands (not coregistered). The results indicated larger RMSEs for the adjustment using three bands, excepted for the RMSE in Z for the check points. The high number of rays when using three bands with shorter baselines can impose a solution that did not fit well for all the object space points, because intersection angles are too acute.

Figure 32: RMSEs of GCPs and check points (CKP) from the Morada de Deus data.

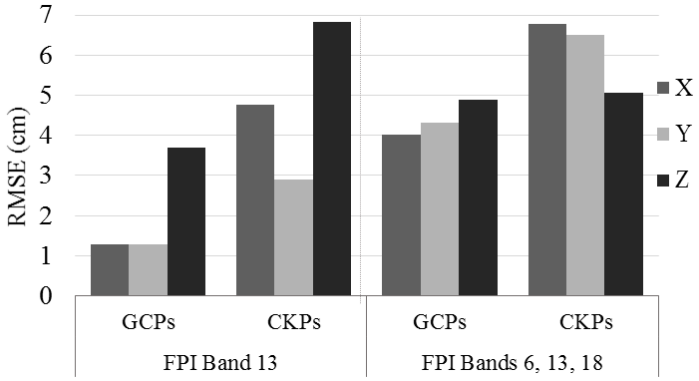

The low overlaps and the characteristics of the parking area, such as homogeneous and repetitive patterns, contributed to problems in the detection of tie points. Figure 33 shows the generated point clouds by using (a) one band and (b) three bands, camera perspective centers and error estimates. Although the planimetric RMSEs of the GCPs and check points were higher when using three bands, the sequential band acquisition system of the FPI camera has an advantage for point cloud generation because the use of more than one band has increased the forward overlaps and, consequently, has decreased the occluded areas (white areas).

Figure 33: DSMs using (a) one band and (b) three bands.

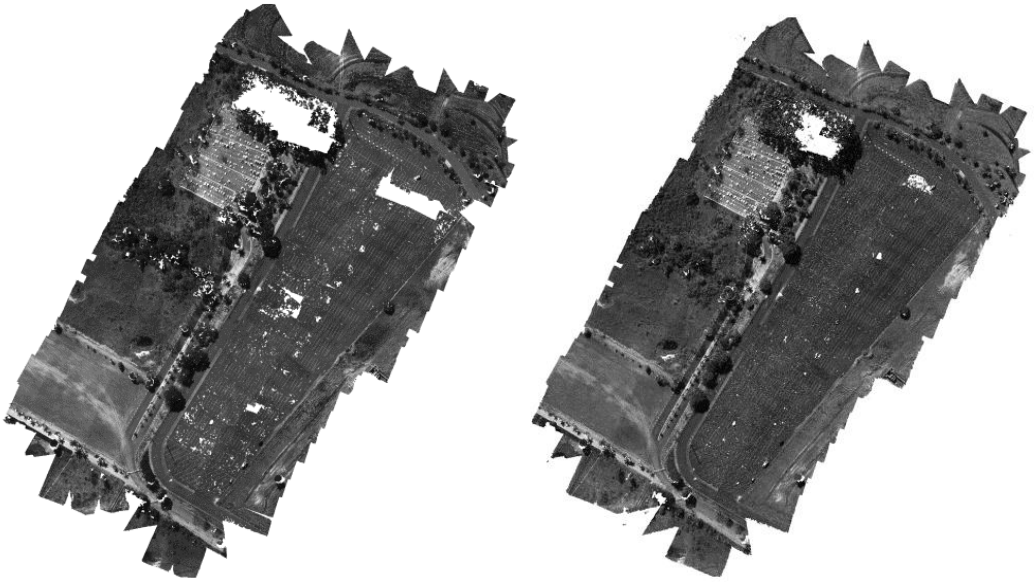

These first trials were fundamental to understanding the behavior of the overall system and data processing which would later be used for the forest data set studies. The next topics describes the experiments and assessment of BBA, using IOPs estimated by close range calibration, and on-the-job calibration, using software based on SfM, with FPI camera data collected both in Ponte Branca and Vesijako.

a) Ponte Branca and Vesijako FPI image data processing with Agisoft PhotoScan:

Table 10 shows details of the three blocks collected in Ponte Branca (Brazil) and the block collected in Vesijako (Finland) processed with Agisoft PhotoScan. For each PhotoScan project in Ponte Branca, four bands of each cube were used as independent images, in order to estimate their EOPs simultaneously in the processing. From the four bands, two bands were acquired by Sensor 1 (NIR) and two bands by Sensor 2 (VIS).

The bands correspond to the first and the last band acquired by each sensor. For the Vesijako data set, three bands were used and only one set of IOPs as the camera model used has only one CMOS sensor (FPI prototype 2012b, Table 1).

A GNSS/inertial system recorded data for each event of band acquisition of the Ponte Branca blocks. The raw data was processed using Inertial Explorer® software. The perspective centres coordinates directly computed for each band were inserted as approximate values with 0.5m of standard deviation. GCP coordinates were inserted as weighted constraints with a standard deviation of 2 cm.

The bands were separated into two groups with IOPs estimated for Sensor 1 and Sensor 2 (see chapter 4). These sets were introduced into PhotoScan as pre-calibrated values (initial, not fixed). It is unclear whether PhotoScan keeps the original values of IOPs inserted as Australis file format, because it was noted that some parameters inserted as equaling zero, received different values after they had been loaded.

The EOPs were estimated using image with full image resolution (option "high" in "Align" mode of PhotoScan, Align being the Bundle Adjustment). The settings for the number of key points per image were used as default values. The tie point outlier removal step was performed using the automatic tools of the software, based on re-projection error (residuals) and the standard deviations of the tie point 3D coordinates. Also, some outlier points were manually removed. The number of tie points used in the adjustment for each block is presented in Table 10. The automated camera calibration was performed simultaneously with image orientation (self-calibration). As a result of this process, image EOPs, sensors IOPs and tie point coordinates were estimated.

Table 10: Agisoft PhotoScan photogrammetric block details.

	Total of images	Spectral Bands*	N. of tie points	GSD	Number of GCPs	Number of CkPs	Direct geo. sensors	Coverage area (km²)
PB1(Plot 5, 6)	1000	1,10,11,25	338553	0.10	9	4	L1L2 and IMU	0.236
PB2(Plot 2)	1148	1,10,11,25	432784	0.10	8	3	L1L2 and IMU	0.39
PB3(Plot 1, 3)	1100	1,10,11,25	374887	0.10	5	3	L1L2 and IMU	0.238
Vesijako	293	4,12,16	141335	0.08	4	0	L1	0.076

*Band characteristics are presented in Table 2 (PB1, PB2, PB3) and Table 8 (Vesijako).

Figure 34 shows the blocks from Ponte Branca and Vesijako. The image blocks PB1 and PB3 (Figure 34 (a) and Figure 34 (d)) consisted of two flight lines while block PB2 had only one (Figure 34 (f)). The control points were measured manually. The

RMSE of residuals in image coordinate (reprojection errors) estimated for blocks PB1, PB2 and PB3 were 0.53 pixel, 0.44 pixel and 0.34 pixel, respectively.

Figure 34: Schematic views of the image blocks collected with the FPI camera (estimation of POEs and point clouds). (a) PB1 (Plots 5 and 6), (b) PB1 (Plots 5 and 6) photogrammetric points, (c) PB1 (Plots 5 and 6) control points, (d) PB3 (Plots 1 and 3) (e) PB3 (Plots 1 and 3) control points, (f) PB2 (Plot 2), (g) PB2 (Plot 2) control points and (h) Vesijako block.

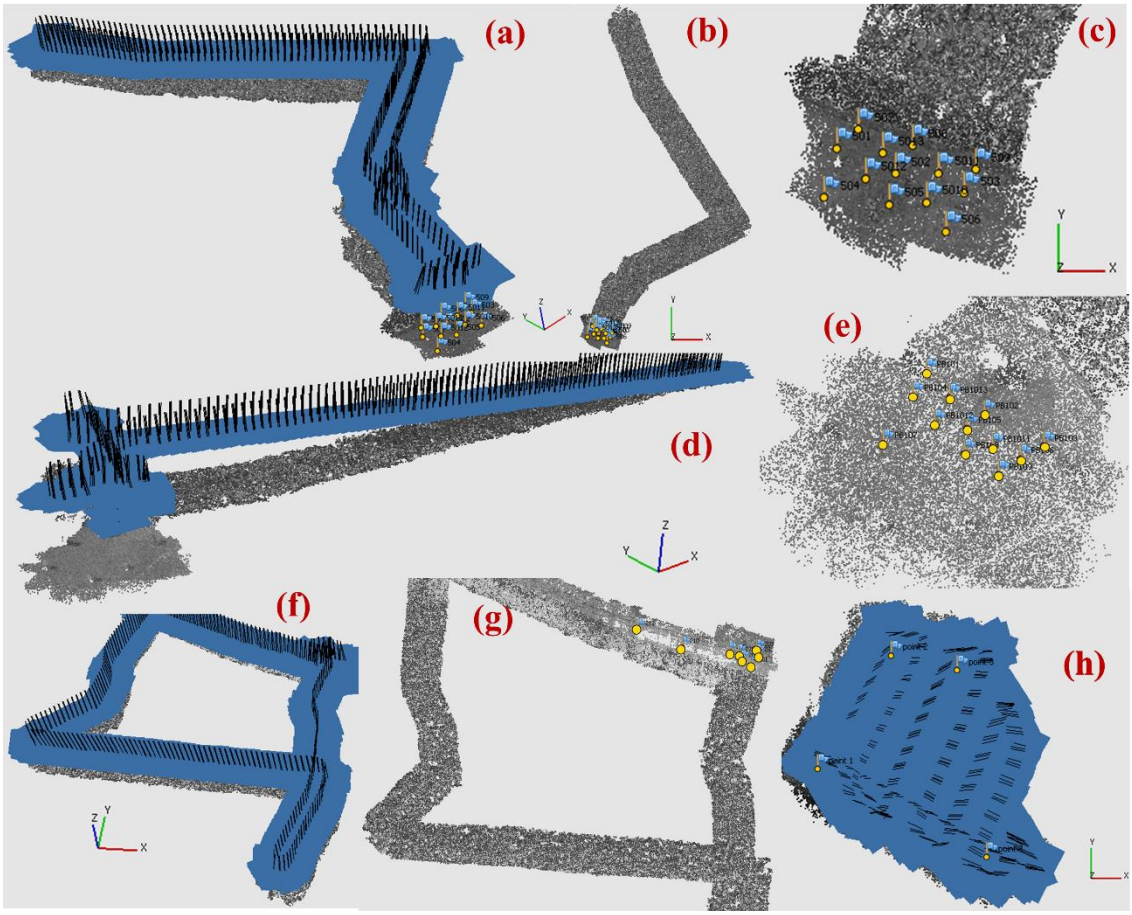

The RMSEs of the discrepancies at GCPs for blocks PB1, PB2 and PB3 varied between 1.4 cm and 8.3 cm in X, between 1.3 cm and 2.7 cm in Y. For check points, RMSEs varied between 1.14 cm and 6.7 cm in X, between 0.8 cm and 2.6 cm in Y. These values are presented in Figure 35. Thus, planimetric errors at GCPs and checkpoints were smaller than one GSD for all blocks. However, the RMSEs of the Z coordinate varied between 10.9 cm and 40.5 cm at the GCPs, and between 9.2 cm and 37.2 cm at the checkpoints. The larger errors presented in Z were found in the block PB2 (RMSEs > 0.35 cm). This is probably due to the block geometry which has only one strip, long flight line and GCPs concentrated in the beginning of the strips (Figure

34 (f)). Even so, these results could be considered as acceptable for the aims of the project.

Figure 35: RMSEs in PB1, PB2 and PB3.

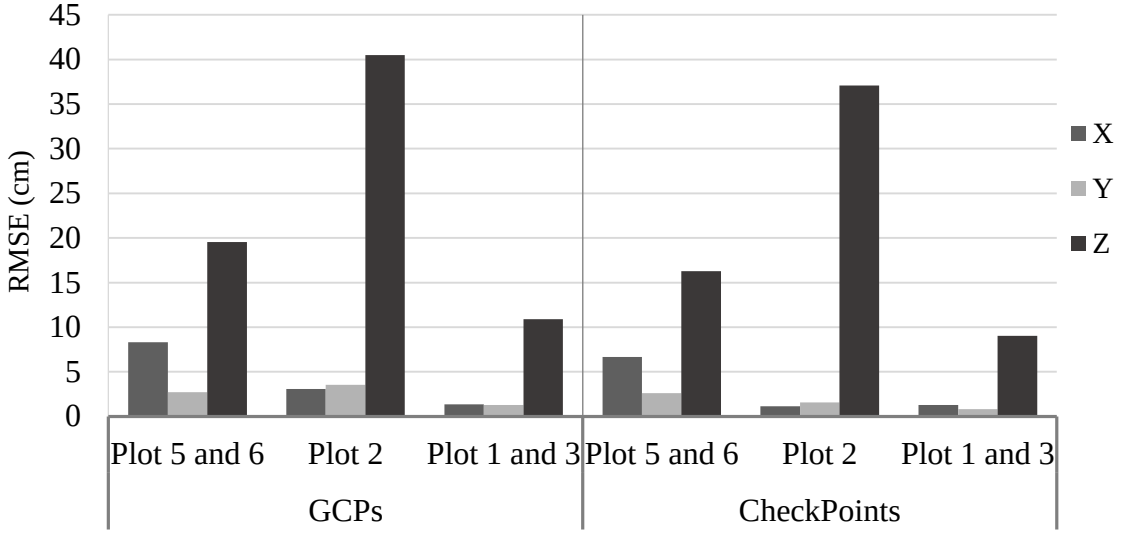

The FPI Vesijako image block was acquired with relatively small overlaps, which is not ideal for PhotoScan processing since its algorithm is based on the SfM technique, requiring small baselines (high overlap with many images). However, the use of three bands of each cube as independent images increased the overlaps and the RMSE of the residuals was 0.6 pixels. Only GCPs were used, due to the low number of points available. The RMSEs of the GCPs were 0.008 mm in X, 0.006 mm in Y and 0.057 mm in Z coordinates. In the PhotoScan project, the initial values for camera position were based on data collected by an on-board navigation GNSS receiver; attitude angles were considered as unknowns; IOPs were based on the nominal values and inserted as approximate values to be estimated during the bundle adjustment (on-the-job calibration).

PhotoScan was also used to generate DSMs of all blocks (PB1, PB2, PB3 and Vesijako). Dense reconstruction was performed using the "ultra-high resolution" option. The DSMs were very representative and dense and will be used for comparison with the proposed approach.

b) Processing sub-blocks of PB1 FPI data, using CMC in-house software

Access to strategies and models implemented in commercial software can be limited for commercial reasons and changing internal algorithms is quite difficult unless

a development Kit is available. This can hamper the integration of data acquired by non-standard sensors with different processes. In order to use compatible algorithms and models, a subset (Figure 36) was selected from PB1 (Plots 5 and 6) image block and the image orientations were estimated using BBA combined by direct georeferencing (Integrated Sensor Orientation) to assess the calibrated IOPs estimated in Chapter 4.

The BBA was performed using the in-house developed software CMC (the same software that was used to estimate the IOPs (Chapter 4). The sub block from PB1 (Plots 5 and 6) was selected outside the forest due to the large number of GCPs (Figure 36). The following configuration was used in CMC:

- Initial positions of the camera PC were based on data collected with a GNSS receiver and attitude angles from INS. Position and orientation values were weighted using standard deviations 0.8 m and 4 degrees, respectively;
- Two sets of calibrated IOPs (c, x_0, y_0, k_1, k_2, k_3, P_1 and P_2), for Sensor 1 and Sensor 2, were considered as absolute constraints;
- A Matlab script for selecting and reducing the number of photogrammetric points (tie-points) measured with PhotoScan to be used in CMC format was implemented. Image coordinates were extracted from the PhotoScan project and used with a standard deviation of 1 pixel;
- GCPs were used with a standard deviation of 2 cm.

Table 11 presents the total number of images used. Thus, in the case of the subset Calib_PB1, the number of images per band was 22. The table also shows the amount of control, check and tie points; and the type of data used as approximate values of EOPs.

Table 11: Information of the sub blocks processed with CMC.

Sub blocks: case studies					
	Number of images	Number of GCPs	Number of CkPs	Number of tie points	Direct geo. sensors
Calib_PB1 Plot 5 and 6	88 (22 per band)	9	4	317	GNSS_L1L2 and IMU
DSM_PB1 Plot 5 and 6	124 (32 per band)	0	0	510	GNSS_L1L2 and IMU

Table 12 presents the RMSEs of GCPs and checkpoints resulting from the BBA performed with CMC. The results indicate that the two sets of IOPs estimated in terrestrial calibration achieved good accuracy with the RPAS data from FPI camera.

The RMSE of image coordinate residuals was 0.38 pixel. The standard deviation of the perspective center coordinates was 0.21 m in X and Y and 0.05 m in Z.

Table 12: RMSEs of GCPs and checkpoints using CMC in IOP assessment.

Sub block PB5-plot-5-and-6		
	GCPs	CKPs
N points	4	9
RMSE X (m)	0.019	0.106
RMSE Y (m)	0.011	0.044
RMSE Z (m)	0.004	0.109

A second sub block was located in Plot 6 as shown in Figure 36. The data was processed using the same configuration of the first sub block, but without GCPs. The RMSE of image coordinate residuals was 0.58 pixels. The standard deviations of perspective center coordinates were 0.15 m in X and Y and 0.07 m in Z, and were considered appropriate for the next step. The adequate quality obtained in the results are related with the use of direct georeferencing data, as good approximations for the adjustment. The purpose of adjusting this sub area was to estimate the EOPs of the images used for DSM generation in chapter 7 with exactly the same models used in the camera calibration.

Figure 36: Sub areas selected from PB1 for study cases.

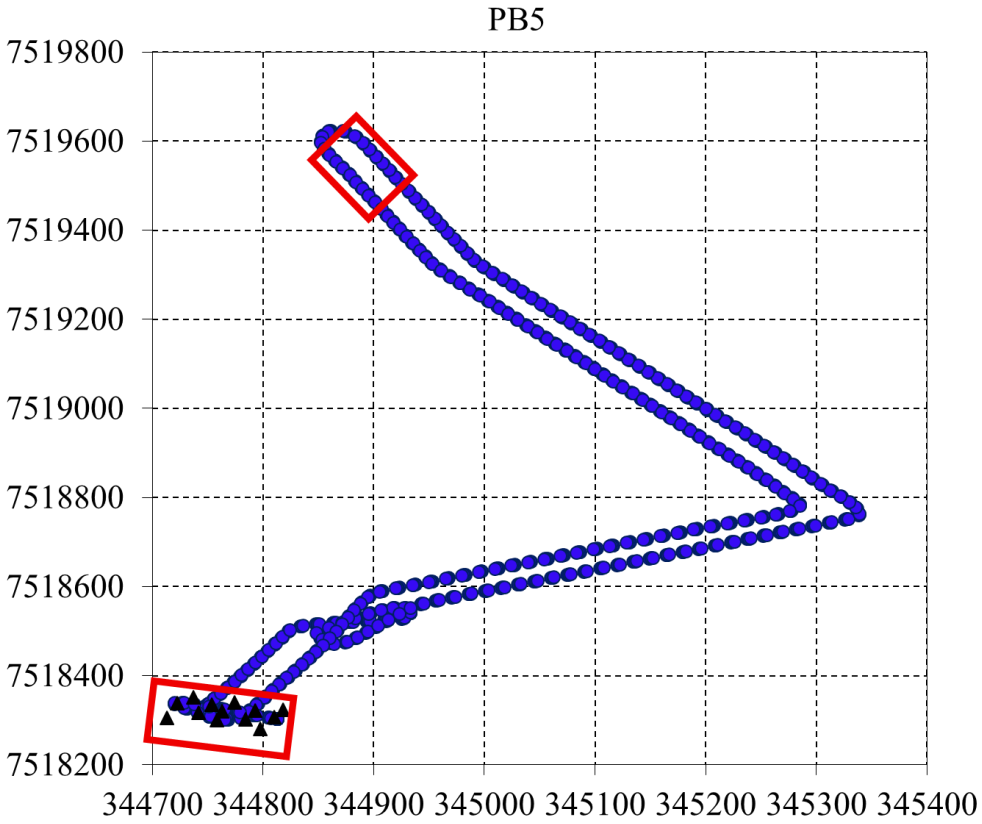

6.4.1 Assessment of cube exterior orientation parameters

Aiming at the generation of a hyperspectral DSM (HDSM), where each point has DN values corresponding to each band of the cube, it is very important to have an accurate estimation of the EOP and IOP. The DN values can then be attributed to a point based on the backprojection process (MIKHAIL et al. 2001), using the collinearity model and object 3D information, which is similar to the indirect technique for orthorectification. In the case of non-aligned spectral bands, the bands should be registered using a 2D mapping function, or the EOPs should be estimated for every band to obtain the 3D transformation from object space to image space. Differences caused by relief displacements appearing as image coordinate errors in bands of a same cube can be reduced using 3D transformations.

The FPI camera internal parameters were studied and estimated in Chapter 4 and the estimation of EOPs for selected bands have been described in this section. However, the EOPs of the reamaining bands also needed to be determined.

The exterior parameters for the unoriented bands can be estimated by interpolation (using reference bands), using BBA of all bands or by direct georeferencing.

Honkavaara et al. (2017) have developed a method where bands without orientation are matched to oriented bands, considering the 3D information and a rigorous approach based on the collinearity model (resection method, MIKHAIL et al., 2001).

An investigation was performed in order to assess the quality of the EOPs estimated for all bands from different methods. Table 13 shows the details of each EOP set used. In test A, linear interpolation was used to compute EOPs (X_0, Y_0, Z_0, ω, φ, κ) for 21 bands, from the EOPs of four bands, estimated by self-calibration with PhotoScan. The same process was used to compute EOPs in G, but the EOPs of the four bands were obtained with the CMC software. From B to E, the 3D band matching (3DBandMatch_, HONKAVAARA et al., 2017) approach was used. In B, the EOPs were estimated using only band 10 as reference band (r10) for the other twenty-four. The EOPs of C, D and E experiments were estimated using one reference band for the bands of the same sensor. The results simulate the use of two bands as reference, one for each sensor. The EOPs of the reference bands were estimated using Photoscan software.

Table 13: Experiment data and details.

ID	EOP source	Description
A	Interpolation PhotoScan	4 bands with EOP estimated by BBA and interpolation of other bands
B	3DBandMatch_r10_all	One reference band with EOP estimated by BBA and other bands are estimated by band matching
C	3DBandMatch_r10_1-9	One reference band with EOP estimated by BBA and bands 1 to 9 Sensor 2 are estimated by band matching
D	3DBandMatch_r1_2-10	One reference band with EOP estimated by BBA and bands 2 to 10 from Sensor 2 are estimated by band matching
E	3DBandMatch_r11_12-25	One reference band with EOP estimated by BBA and bands 12 to 25 from Sensor 1 are estimated by band matching
F	3DBandMatch_r25_11-24	One reference band with EOP estimated by BBA and bands 11 to 24 from Sensor 1 are estimated by band matching
G	Interpolation CMC	4 bands with EOP estimated by BBA and interpolation of other bands

For these experiments, four cubes covering the area with GCPs were selected from PB5. The image coordinates of the GCPs were manually measured in all bands of the four cubes. The image coordinates of each point in each band were calculated by the collinearity equations (Equation 1), using GCP ground coordinates, sensor IOPs and the different sets of EOPs (Table 13). The estimated image coordinates were compared with

the values measured manually. Averages and RMSEs of the differences are presented in Figure 37.

The EOPs computed using linear interpolation from EOP values estimated with PhotoScan and CMC, in A and G, respectively, achieved similar averages and RMSEs. In both cases, the RMSEs varied from 5.89 to 5.96 pixels in column and 6.26 to 6.62 pixels in row and were the highest RMSEs compared to 3D band registration using resection (B to F). The RMSEs of the resection method varied from 1.67 pixels in column and 2.12 pixels in row, when using only band 10 as reference for all other bands. Using one band for each sensor gave subpixel RMSE values (0.27-0.91 pixels), except for experiment F, where band 25 was used as the reference. In this case, it could be seen that two bands (12 and 13) from two cubes had the highest residual values (> 10 pixels for some points). If these bands were excluded the result would have been 0.8 pixels in column and 0.23 pixels in row. The same was observed in B, where bands 24 and 25 presented the largest values of residuals. This fact is due to the spatial distance of the bands to the reference band and some movements of the platform.

Figure 37: Average and RMSE of image coordinate residuals for all bands and different EOP.

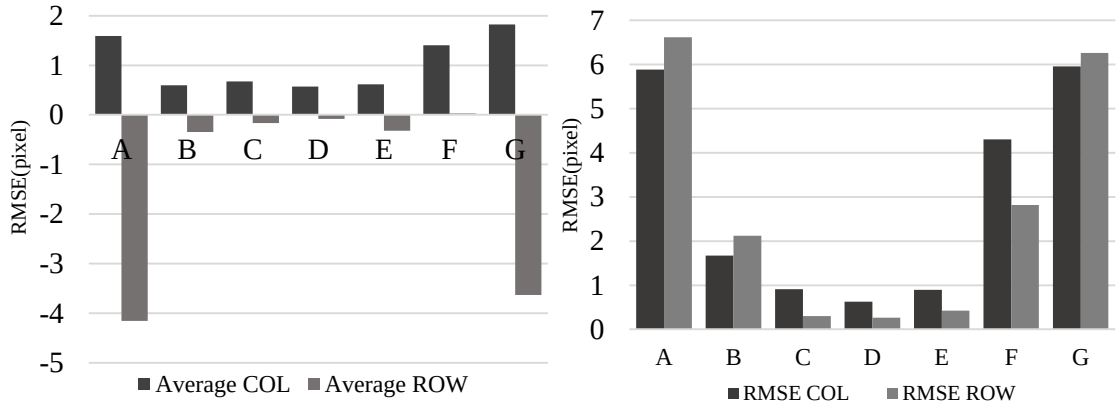

The effect of EOP interpolation in the image residuals of one cube is presented in Figure 38. It can be seen that residuals were smaller in some bands near to the adjusted bands. This also indicates that the temporal variations of the EOPs cannot be modelled by a linear model.

Figure 38: Image coordinate residuals for one cube using EOPs estimated by linear interpolation.

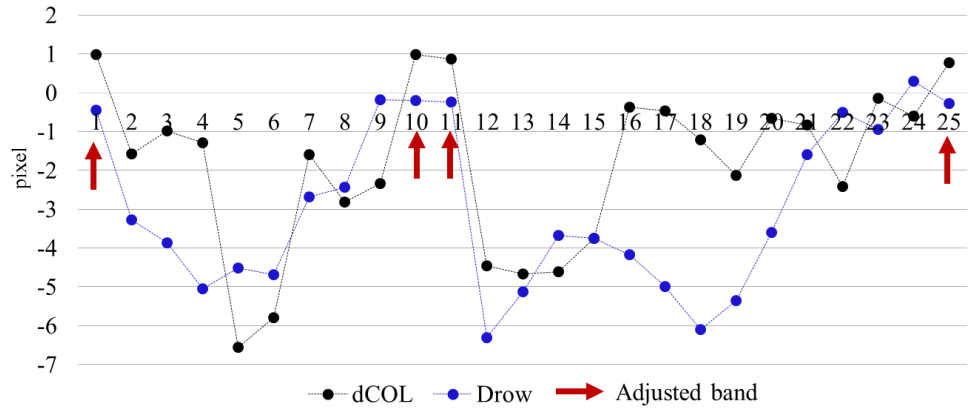

Figure 39 shows the image residuals of the same cube featured in Figure 38, but resulting from experiment B (3DBMatch_r10_all). The residuals show a good fit of the EOPs for most bands (less than 1 pixel for bands 1 to 24). As mentioned before, the highest residuals are in band 25, which is further apart (spatially) from the reference band 10.

Figure 39: Image coordinate residuals for one cube using EOPs from 3D band registration using the resection approach.

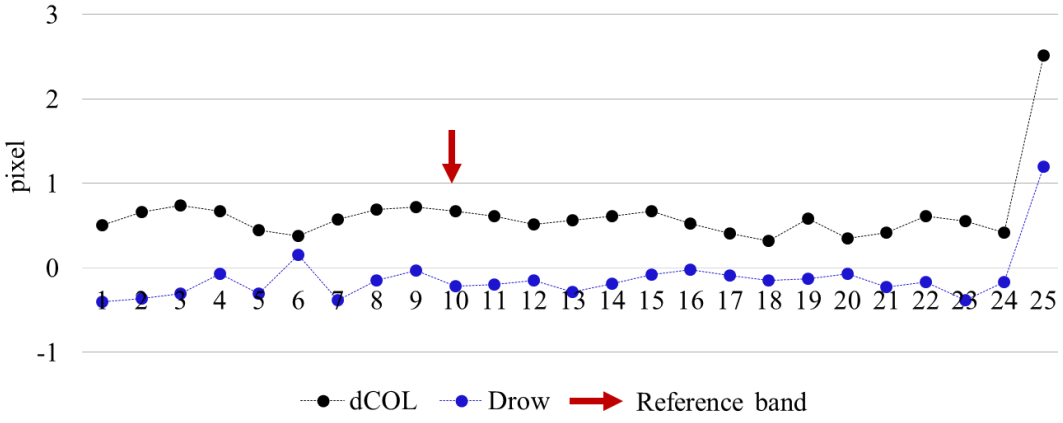

6.5 Discussions and conclusions

Experiments were performed with the orientation of image blocks in two forest areas using FPI cameras. The assessment of the blocks in the Brazilian forest was based on RMSEs in the X, Y and Z coordinates of GCPs and check points outside the forest. The results showed that, despite the weak geometry of the blocks and control points, the RMSEs in X and Y were smaller than 0.10 m (one GSD) for the three blocks, and in Z the RMSEs varied from 0.09 m to 0.37 m. The lowest RMSEs in Z were obtained in

block PB2, probably caused by the weak geometry of the image block, when using only one strip. The camera perspective center coordinates collected by a dual-frequency GNSS and used as approximate values have significantly contributed to the quality of the estimated values. In general, the results present enough accuracy for the generation of DSM.

The IOPs estimated in the terrestrial calibration step were assessed with data collected using an RPAS and the results showed that these IOPs were accurate enough for the BBA of aerial images collected in complex forest areas.

The EOPs, from bundle adjustment, of reference FPI bands were used to estimate the EOPs of remain bands by interpolation and by using the 3D band matching approach developed by Honkavaara et al. (2017). The results were assessed using the image coordinates of a pre-signalized control points. The RMSEs of the differences in image coordinates have shown that the linear interpolation of EOPs provide higher errors (in some bands up to 7 pixels). However, the FPI bands can be accurately registered with residuals smaller than 1 pixel using the 3D band matching method. The EOPs generated by this process can therefore be used for the hyperspectral DSM generation. As concluded in chapter 4, the 2D registration of the FPI camera bands can achieve subpixel results in flat areas, but has disadvantages for non-flat areas. The 3D band matching method, based on the collinearity model and 3D information of the object can be a more accurate alternative and reduce errors caused by relief displacement and image acquisition. The selection of one these methods should taking into account the accuracy and the complexity of the processes. Although more accurate, the 3D method requires more steps and processing cost. Thus, if the error of the interpolation is acceptable, this will be probably the easiest option.

7. DSM GENERATION USING HYPERSPECTRAL 2D FRAME CAMERA

7.1 Introduction

3D point clouds of forest areas are being used increasingly as a means of acquiring complementary data for several forestry applications, such as the retrieval of the vertical structure, estimation of forest biomass and volume. ALS data usually have two or more pulse returns associated with the same emitted pulse and some pulses can penetrate below the canopy (HYYPPÄ et al., 2008). This feature enables them to be separated at ground and above-ground points, making the generation of DTMs and CHMs feasible. Acquisition of points under the canopy by optical images and photogrammetric techniques depends on the visibility of the ground or bare soil in the images, as the point cloud generation is based on stereoscopy and image matching. Since each point in the ground should be visible in at least two images (BALTSAVIAS et al., 2008; OLIVEIRA et al., 2015; OLIVEIRA et al., 2016b). Boreal forests often present sparse trees, making the bare soil visible in many areas when viewed from aerial images. When the forest is not too dense, the objects can be separated into classes, such as trees, shrubs and ground. However, bare soil in dense forests is hardly visible from aerial images, hence these objects can be separated into classes such as shadow areas and trees and these basic classes can also be used as cues for DSM generation.

Hyperspectral data has been used in forest applications, such as tree species classification and estimation of biophysical properties. DSMs can be derived directly from high resolution hyperspectral 2D frame images, since the frame cameras can provide multiple records of the object from different viewing directions, offering the possibility of obtaining redundant stereoscopic measurements and analysing the multidirectional reflectivity characteristics (HONKAVAARA et al., 2013; AASEN et al., 2015). The combination of hyperspectral information from different viewing angles and DSMs can increase the quality and the possibilities of remote sensing applications for forests (NÄSI et al., 2015; OLIVEIRA et al., 2016a; NEVALAINEN et al., 2017).

However, existing software packages for DSM generation do not allow the generation of DSMs directly with multiangular spectral observations. Instead, a common DSM is generated and both the spectral and angular information are missed.

The use of spectral information in the matching process is potentially valuable with novel imaging systems with multi- or hyperspectral 2D frame sensors, but this has rarely been utilized. This study applied image matching in hyperspectral images both in boreal and tropical forest environments. The objective of this investigation is to obtain an object model, consisting of 3D geometry and multiangular spectral data, as features of forest areas. Additionally, the study proposes the use of spectral information to optimize the selection of the image matching parameters (window size, search space, similarity threshold) for different objects (ground and tree tops) in an object space-based multi-image matching approach.

The DSM algorithm was implemented using dense image matching based on classes and using a data structure which allows the assignment of the hyperspectral reflectance signature for all matched points, as well as the multiples viewing angle information.

7.2 Proposed methodology for DSM generation

The proposed method, called the hyperspectral VLL (HVLL), was implemented using the C/C++ programming language and UPTK library modules (Unesp Photogrammetric ToolKit), which was developed by the photogrammetry research group of the Cartography Department of FCT-UNESP. UPTK has implemented photogrammetric and image digital processing algorithms. In some cases, the functions have been adapted according to the process. Additionally, an extension to HVLL was proposed, using image classification information to adapt matching parameters (HVLLC). The in-house DSM software was implemented to use the FPI camera data in the original format (12 bits, float precision).

7.2.1 Search space reduction – object space correspondence

The VLL technique was implemented with multiple image matching and hierarchical search. The process starts with the generation of an image pyramid for each image provided, with as many levels as desired. The convolution of the image is

performed by a Gaussian filter at each level of the pyramid and the image is then downsampled to half the image size of the previous level. The image pyramid enables a hierarchical search with variation of the parameters at each level and, thus the reduction of processing time and false correspondences.

The VLL approach (section 2.3.4) is the main technique for the next steps. For each point of the approximate surface entered as a regular grid, the planimetric coordinates are used and initial height for the algorithm is calculated by subtracting the ΔZ_{MIN} (provided *a priori*) from the approximate height value ($Z_{MIN} = Z_0 - \Delta Z_{MIN}$). The point is projected from the object space to all images in which this point appears, using collinearity equations. Matching windows are defined and the similarity function is computed for the multiple pairs. These windows are generated by rectification procedure over the original images (Section 7.2.2). Then, the altitude Z_{MIN} is incremented by dZ (provided *a priori*) until it achieves the Z_{MAX} ($Z_{MAX} = Z_0 + \Delta Z_{MAX}$) and the correspondences among the new windows are calculated and recorded for each new Z_i coordinate. Multiple images and multi bands can also be used (Section 7.2.3). The height assignment to the point is completed by analyzing the largest overall value obtained from the correlation coefficient vector, for each Z_i within the search interval. The point cloud generated at each level of the pyramid is interpolated and used as the initial model for the subsequent level.

The basic parameters and thresholds to be provided for each hierarchical level are:

- window size;
- minimum threshold to accept the correlation coefficient;
- size of the vertical search interval (ΔZ_{MAX} and ΔZ_{MIN});
- increment value (dZ) at each iteration of height;
- resolution of the grid;
- maximum distance to search for the points to be used in the DSM interpolation process.

The VLL method limits the search space into the vertical range ($[Z_{MIN}\text{-}Z_{MAX}]$). Considering a high resolution image, for example with the GSD of 7 cm, a vertical search interval of 20 m and an increment for altitude variation of dZ = 7 cm, 286 repetitions are required for each point of the DSM grid. However, with the use of hierarchical resolution levels, the amount of processing is reduced at each level, since it is possible to have a higher dZ variation for the lower resolution levels and the vertical

range can be reduced and the increments can be smaller for the higher resolution levels. Knowledge of the area can also help to establish better parameters. Moreover, in the proposed method, these parameters can change adaptively (Section 7.2.3) according to the object class. The matching calculation is performed from the object space to the image space, and the best matches give the estimate of an elevation for an (X, Y) point being analyzed, thus giving the 3D positions directly.

7.2.2 Resampling windows for matching

Given the IOPs and EOPs, the image coordinates of each image corner are calculated using inverse collinearity equations (MIKHAIL et al., 2001) in the ground reference system. As a result, it is possible to verify whether a certain point of the DSM area is part of the images. When the point appears in less than two cubes, the process stops and jumps to the next grid cell. After verifying the images in which a point is appearing, the matching windows are determined to search for homologous points.

In order to reduce scale problems and variations in viewing angle, the windows are rectified before computing the similarity function. For each point, a patch centered at this point (X, Y) is defined in the object space. This patch has a pre-defined size (n x m) and the cell size is equivalent to the average GSD of the images. All points of the object space patch are projected into all possible images, and the intensity values are assigned by interpolation, creating rectified windows. The rectification uses the height value Z_i of each vertical search step in the range $[Z_{MIN}\text{-}Z_{MAX}]$. This process is important for reducing the effects of perspective distortion, relative rotation between the planes of the images.

The projection of the point position in object space to the images is made by the collinearity equations (Equations 1), obtaining the coordinates in the photogrammetric system (x_f, y_f), and performing the inverse procedure for lens distortion. After the photogrammetric coordinates of a point (x_f, y_f) have been calculated, it is necessary to add distortion effects and to convert them to the image system (column, row). The projection of the X, Y, Z coordinates leads to sub pixel coordinates within the images, thus the DN value of each pixel in the rectified window is determined using bilinear interpolation. The photogrammetric coordinates are computed in each height increment (dZ) for all points of the grid. In order to optimize the calculation of the

photogrammetric coordinates, the collinearity equations (Equation 1) were separated into three parts to pre-store constant values (OLIVEIRA, 2013, p. 69-70).

7.2.3 Matching of multiple adaptive windows

The correspondence method used is ABM method and the correlation coefficient (Equation 12) is the similarity measurement function. The correlation coefficient is calculated for each possible pair between the reference and search images. If one point appears in five images, five rectified windows are created, and four correlation coefficients are calculated. These correlation coefficients are compared to a minimum acceptable value, defined empirically, which can change for each pyramid level. The average of values greater than this threshold is assumed as a single coefficient, here called global correlation coefficient (GCC). At the end of the vertical scanning, for each value of Z_i there is a global correlation coefficient and its standard deviation. The point height is assigned by verifying which Z_i has the highest global coefficient and the smallest acceptable standard deviation.

A fundamental issue of ABM techniques is the use of an appropriate matching window size. The texture information within each window needs to be considered. If none of the correlation coefficients reaches the acceptance threshold, an iterative process to change the window size and shape was used following the approach proposed by Kanade and Okutomi (1994) and Zhang (2005).

The process starts from a small window (nxm, with n = m) centered at the point (X, Y); (2) compute the GCC for each Z_i along the vertical search line [Z_{MIN}-Z_{MAX}], as described above; (3) exclude the candidates smaller than the threshold; (4) when no GCC is higher than the threshold, the process starts again with a different size and shape of window; (5) otherwise, continue the procedure jumping to the next grid cell.

The window is increased by 2 pixels in one of its four directions (right, left, up and down) and the GCC are calculated again for each Z_i along the vertical line [Z_{MIN} - Z_{MAX}]. If this expansion decreases the GCC value, the direction is not suitable and another direction is selected for further expansion (2 pixels). The same process is repeated for each of the four directions, until the GCC achieves sufficient value or until the window size reaches a size limit (here was used 45 pixels). Figure 40 illustrates this process.

Figure 40: Window expansion. Adapted from Kanade and Okutomi (1991).

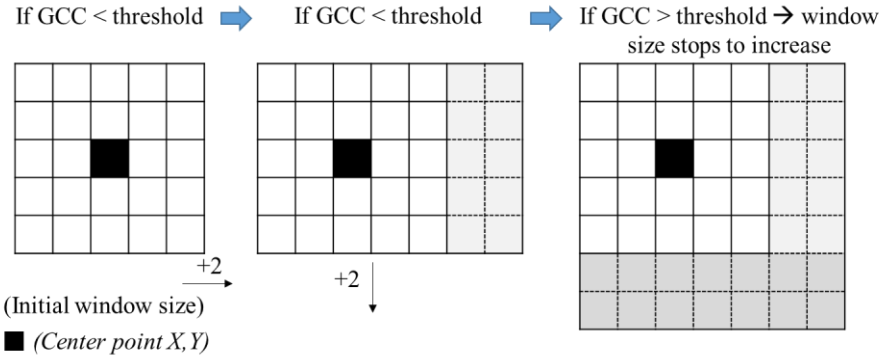

7.2.4 Matching using multiple bands

As discussed in this study, EOPs change according to the band when the acquisition with the FPI camera is not instantaneous, resulting in non-registered bands. Additionally, the need for different sets of IOPs was verified for the camera with two sensors (Chapter 4). The existing commercial software packages are not prepared to treat the hyperspectral 2D frame cube with nonregistered bands as individual images with different IOPs and EOPs, when the bands are in the same data cube. The possibilities when using these software packages are: register the cubes in advance and estimate the same EOPs for all bands; or split the bands into separated image files and input the bands as independent images estimating different EOPs for each band.

In order to cope with this problem, the proposed approach implements a different structure, considering each cube as having independent bands with its own EOPs and IOPs (one set for each sensor) and taking into account the spectral differences of the bands for the matching process.

The technique of image matching using multiple bands, selects the reference cube (most nadir) and computes the correlation coefficients between bands of different cubes for a given point. In addition, the correlation coefficient threshold between bands of the same cube is weighted according to the spectral differences to reflect the impact in the similarity measurement. The weight value is given *a priori*, and it is used to reduce the threshold. If the minimum value of correlation coefficient threshold is equal to 0.9 and the weight is 0.9 (90%), the minimum correlation coefficient acceptable is 0.81.

Figure 41 illustrates the method of window comparisons among the cubes and bands. In this example, correspondence of a point P (a window) is searched over two bands (VIS, NIR) of three cubes. Cube 2 is the closest to nadir and is then selected as

the reference cube. Band 20-Cube 2 can be the reference band, because it offers the best contrast, for instance. The total number of correlation coefficients calculated is seven. Four correlation coefficients are calculated using the reference cube (Cube 2) and the correspondent bands in different cubes (B20_Cube 2*(Ref)* x B20_Cube 1; B20_Cube 2*(Ref)* x B20_Cube 3; B1_Cube 2*(Ref)* x B1_Cube 1; B1_Cube 2*(Ref)* x B1_Cube 3); and three correlation coefficients are obtained comparing bands from the same cube (B20 x B1, Cube 1; B20 x B1, Cube 2 and B20 x B1, Cube 3), as indicated by the arrows in Figure 41. The correlation coefficients resulting from different bands of the same cube have weak geometric, due to the small baseline, and the spectral similarity can be small, depending on the object. On the other hand, the geometric distortions are smaller than higher baselines.

Figure 41: Image matching window comparisons.

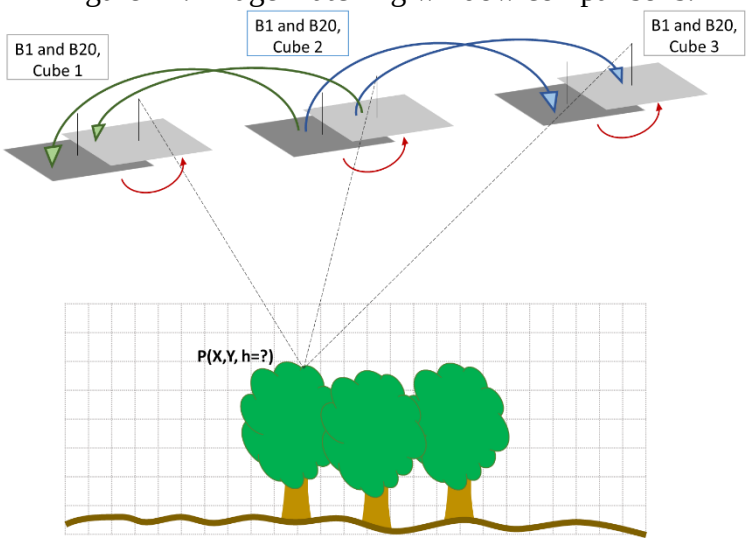

These correlation coefficients (CC_i) are divided into two groups: from the same bands in different cubes and from different bands in a cube. As mentioned in section 7.2.3, the values are compared with a minimum acceptable value for the correlation coefficient, and the average is taken as the GCC. The average of the coefficients between different spectral bands of the same cube which are greater than the threshold are also computed and assumed as a band global correlation coefficient (BGCC). Figure 42 illustrates the average of the two groups of CC_i from Figure 41. "B20_Cube_2(Ref)" means band 20 of cube 2, where cube 2 is the reference cube, because it is the closest cube of the point in object space. The point height is assigned by verifying which value Z_i: $Z \in [Z_0-\Delta Z_{MAX}, Z_0+\Delta Z_{MIN}]$ maximizes the values of GCC and BGCC.

Figure 42: Representation of global correlation coefficients calculation.

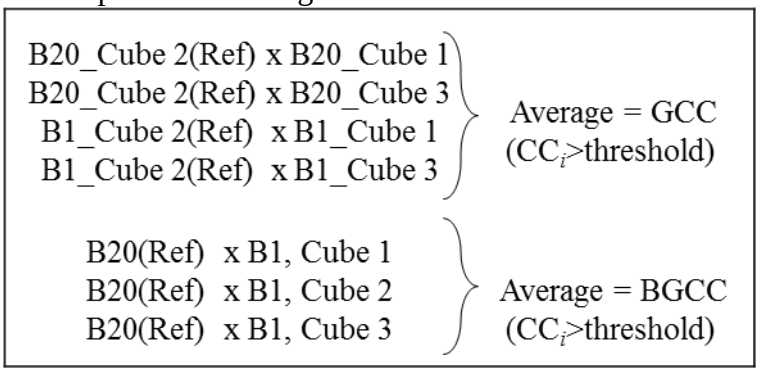

*B = band, Ref. = Reference

7.2.5 Matching with adaptive parameters based on image classification

Hyperspectral images give detailed spectral information for each pixel in an image, which assists the classification process. Classified images can improve the process of image matching, supporting the selection of parameters, such as window size, thresholds and search space limits, for different objects (classes). For example, if a pixel is classified as soil, the height range for the VLL method is smaller than for pixels classified as top of a tree. In addition, the resulting point cloud can be classified based on the image pixel classes from the image classification process. The objective of the following strategy was to use information extracted from image classification to adapt the image matching parameters (Figure 52 and Figure 74).

The proposed method starts with the 2D registration of the cubes. This registration can pose some problems mainly because of parallaxes caused by differences in object heights and viewpoints, but for the purpose of this study this preliminary registration is considered sufficient to provide accuracy adequate for the classification of the images. The registered cubes are classified in generic classes (for instance, shadow, top of the trees and ground). Several classification techniques (supervised and un-supervised) were tested, but k-means presented the more suitable results for this application, and, additionally, it is a less complex method.

The image matching parameters mentioned can be defined based on the selected classes and the matches are labelled with the corresponding class. If the class represents homogenous area, the window size is higher and the coefficient correlation threshold is smaller. These values are given *a priori*.

At the highest resolution level of the hierarchical matching process, with full resolution images, the parameters (window size, vertical range, average height and thresholds) for the point under analysis change according to the class of the point in the reference image. Computing correlation coefficients of templates with different sizes along the vertical line would generate heterogeneous correlation values for every step along the same vertical line and this could produce false matches. The strategy keeps the same window size for all steps (dZ) in the vertical line. Thus, it is used only at the highest resolution level, selecting the parameters based on the approximated height from the previous level, which is a better approximation when compared to the first levels.

7.2.6 HDSM strategy

In the last level of the hierarchical process, the spectral information is assigned and recorded for each point. Following the image matching steps described, the height value in the vertical line search that maximizes the correlation between the reference cube (most Nadir) and other cubes, is assigned to a given point. The image pairs with valid matching (higher than a threshold) have their viewing geometry attributes computed (azimuth and zenith viewing angles) and stored for each band. The DN values of the point on each band is stored as well. The target-sensor geometry parameters and DN value are also computed for bands that were not used in the image matching process, using their EOPs, IOPs and point coordinates.

Thus, the HDSM is built with a spectrum of multiple cubes and their viewing angle values (zenith and azimuth angles of point to sensor), the geometric relationship among Sun (azimuth and zenith) - target-sensor are known. The viewing geometry information is very important in order to model the anisotropy phenomena of the object. The geometry angles (see Figure 5), with respect to each image used to estimated the matching score, are recorded in the resulting HDSM (BURKART et al., 2015; PINTO et al., 2017; ROOSJEN et al., 2017).

7.2.7 Quality assessment

The evaluation of the DSM quality by the applied techniques was performed by visual analysis and comparing with DSM results from a commercial software. Visual

analyses of the point clouds were performed using three-dimensional visualization and profile extraction to verify the aspects of the elements of the scene, the dispersion (presence of spurious points) and the density of points.

The difference between the DSM generated using the proposed method and the DSM from the commercial software were calculated. For the DSM in the Finnish boreal forest, ALS data was available and was also used in the assessment of the results.

7.3 Study areas and data sets

The experiments were performed using two different forest environments, one representing the Atlantic (tropical) forest and other representing the Boreal forest. The tropical forest area was selected within the PB1 block, in the Ponte Branca fragment. The area has the dimensions 60 m x 45 m, covering Plot 6 (Figure 43). This plot represents an advanced stage of the forest, having a high density of high secondary trees at 3 to 4 well defined canopy layers (BERVEGLIERI et al., 2016). The second area is located in Vesijako, Finland, covering an area of 60 m x 55 m. The primary tree species in the area was Birch (*Betula pendula*).

The two areas are sub-sets of the image blocks processed and discussed in Chapter 7. A set of twelve cubes in two strips was selected from PB1 data. Fourteen cubes were chosen from the Vesijako image data. In addition, ALS data from the National Land Survey of Finland, acquired in 13 May 2012 were used as the reference DTM for the assessment of the results of the Finnish data. The minimum point density of the NLS's ALS data is 0.5 point/m^2, with elevation accuracy of 15 cm, for points of well-defined surfaces, and horizontal accuracy of 60 cm. ALS data from Finland is freely distributed by NLS (http://www.maanmittauslaitos.fi/en/maps-and-spatial-data/expert-users/topographic-data-and-how-acquire-it/national-land-survey-open).
Figure 43 (b) shows the selected areas and Figure 44 presents the ALS data.

IOPs and EOPs of the Vesijako images and a reference photogrammetric DSM were determined using Agisoft PhotoScan software (Section 6.4). For the PB1-Plot6 data, the EOPs and IOPs estimated by the in-house software CMC were used.

Figure 43: DSMs of whole blocks generated using PhotoScan (a) Ponte Branca data set PB1 and (d) Vesijako. Yellow squares represent the study area for DSM generation.

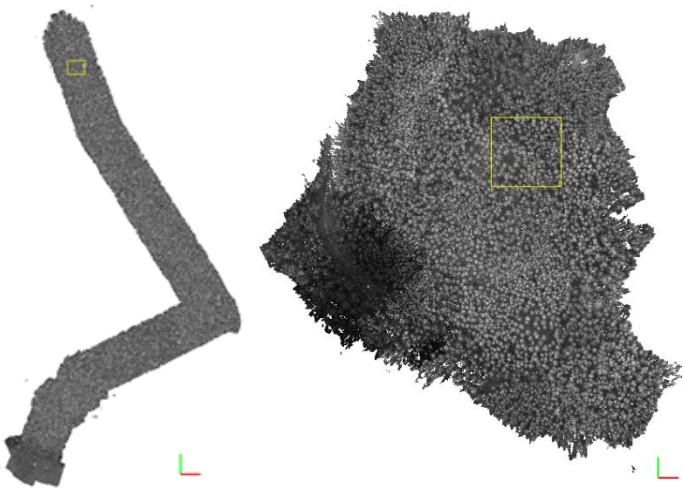

(a) (b)

Figure 44: ALS data from NLS and a box covering the study area.

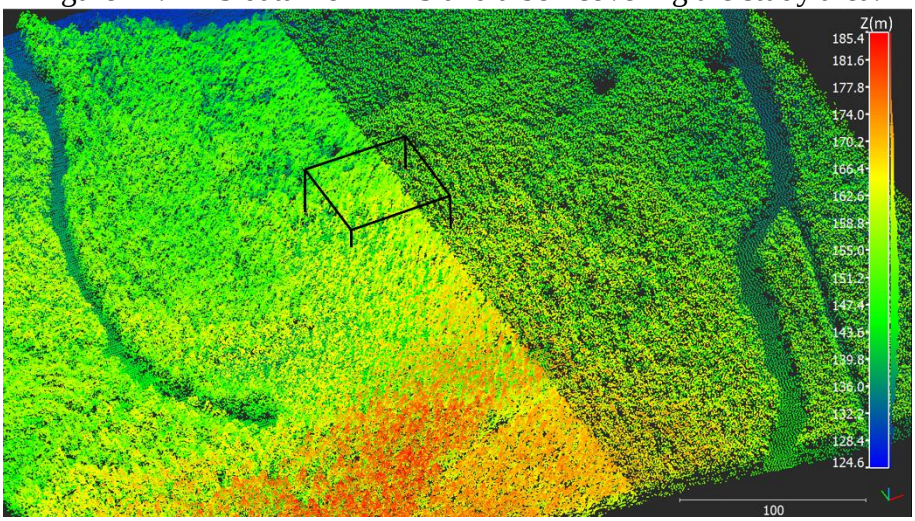

7.2 Experiments and results

In this section, the experiments and results obtained with the HVLL and HVLLC are presented. For the execution of the experiments, the IOPs and EOPs estimated in Chapters 4 and 6 were used. Tests were performed changing the parameter settings in two areas with different characteristics: tropical forest and boreal forest. Section 7.2.1 presents the results obtained using Vesijako data set. The purpose of these experiments was to analyse the contribution of the addition of the classification information (see subsection 7.2.5) to the matching process. The reference data were a DSM generated with PhotoScan and ALS data from NLS survey. Section 7.2.1 presents the results of

the method described using data from the tropical forest, located in Ponte Branca fragment, São Paulo State, Brazil. The results were compared with a DSM generated with the Photoscan software.

7.2.1 Using Hyperspectral Frame Images from Unmanned Airborne Vehicle for Detailed Measurement of Boreal Forest 3D Structure

The test area for these experiments represented a typical boreal managed forest site, with spaced deciduous trees and areas where the ground is visible from aerial images. Ten cubes were selected from the full image block of Vesijako data set (Chapter 6), to perform the DSM generation of an area with size of 60 m x 55 m. To investigate the impact of the developed procedure using hyperspectral classification, two experimental cases were configured in the following experiments. In case 1, the HVLL was used and in case 2, HVLLC was applied (7.2.5). Rectified windows (7.2.2), adaptive window size and shape (7.2.3) and multiple bands (7.2.4) were used in the two cases, and multiple band matching processing was configured to use three bands. These bands were the same used to estimate the EOPs using PhotoScan software (Chapter 6). The full sets of bands were not used because of the high computational costs and because low geometric improvement which would be expected with more bands. These experiments are based on Oliveira et al. (2016a).

The algorithm was configured hierarchically using four resolution levels. Three band from each cube were used to perform the image matching. The HVLLC was used only in the full resolution images, considering the previous levels resulted from HVLL. When using HVLLC, the matching parameters were different for each class. Window size, for instance, started from 7x7 pixels for classes “tree” and “tree top”; 9x9 pixels for class “ground-vegetation” and 15x15 pixels for class “ground-shadow”. The size of window is higher for shadow area due to the homogeneous. The class “ground-vegetation” was in some cases associated as part of class “tree”, thus the vertical line length was assumed one meter higher for the minimum height ($\Delta Zmin$) than for the class “ground-shadow”. These parameters were selected based on experimental tests and the previous knowledge of the area. In HVLL, the size of correlation window started from 7x7 pixels for all points.

The study area selected from the full Vesijako block was cropped from the whole PhotoScan DSM, in order to compare the results produced. Figure 45 shows the DSM

selected from PhotoScan and Figure 46 shows its oblique view. The points are colored by height, from blue to red representing the variation from minimum to maximum height, respectively.

Figure 45: Nadir view of PhotoScan DSM colored by height of Vesijako test site.

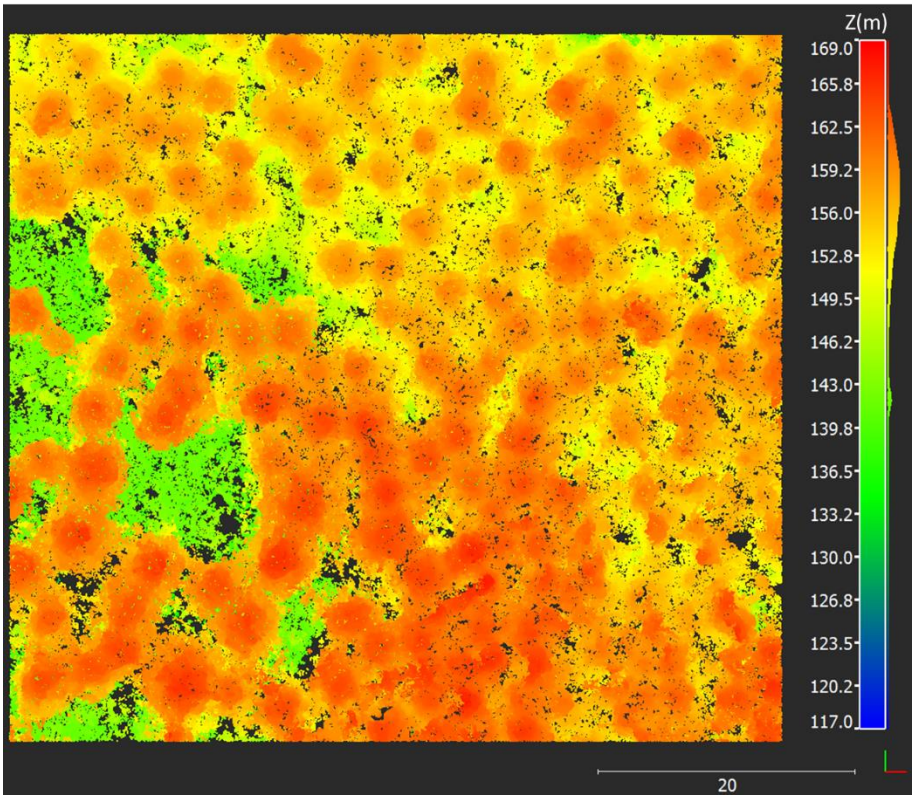

Figure 46: Oblique view of PhotoScan DSM colored by height of Vesijako test site.

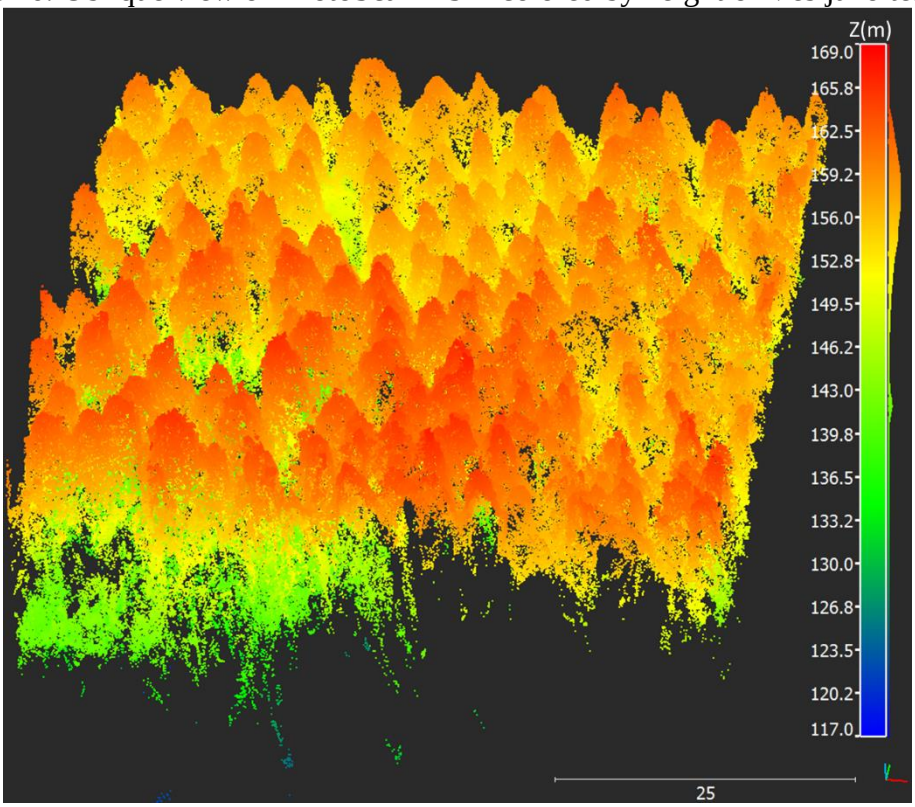

The DSM resulting from HVLL is presented in Figure 47 (nadir view) and Figure 48 (oblique view). Figure 49 shows the DSM colored with DN values of band 615.5 nm. Visual analysis of the PhotoScan and HVLL DSMs indicates proper quality of the vegetation 3D reconstruction, but the HVLL DSM had more spurious points in the covered area than the PhotoScan DSM, which presented more spurious points beneath the ground. Some gaps over the canopy occurred because of the lack of overlaps or no correspondences. It can be noted that, at the ground level, PhotoScan performed well only in large clearance areas.

Figure 47: Nadir view of Vesijako test site DSM, generated with HVLL. Points are colored by height.

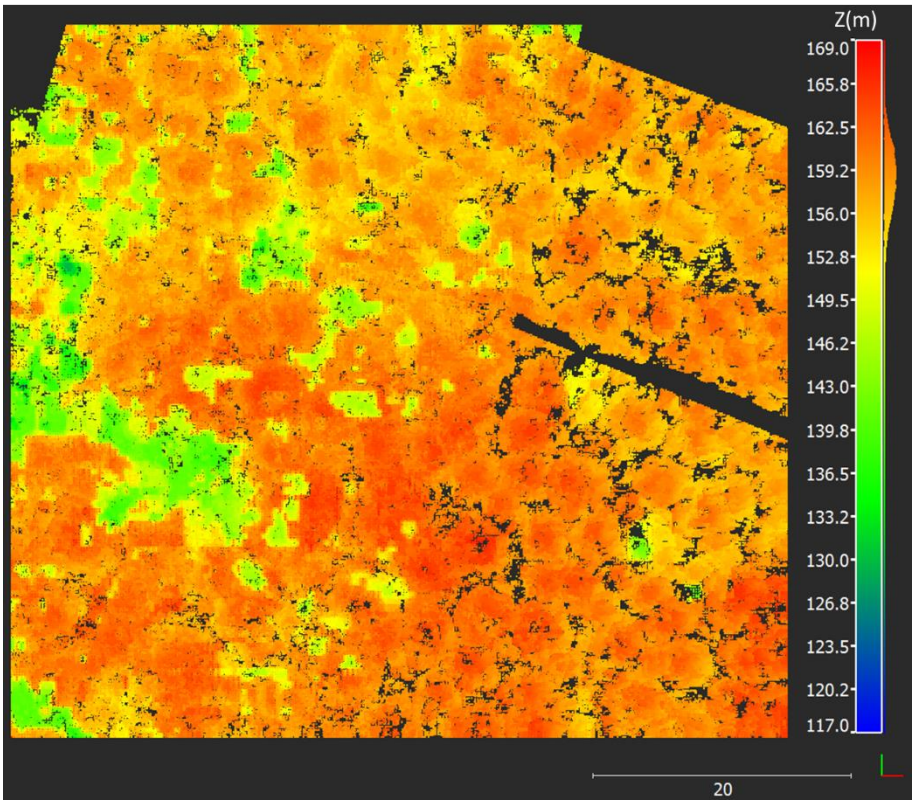

Figure 48: Oblique view of Vesijako test site DSM, generated with HVLL. Points are colored by height.

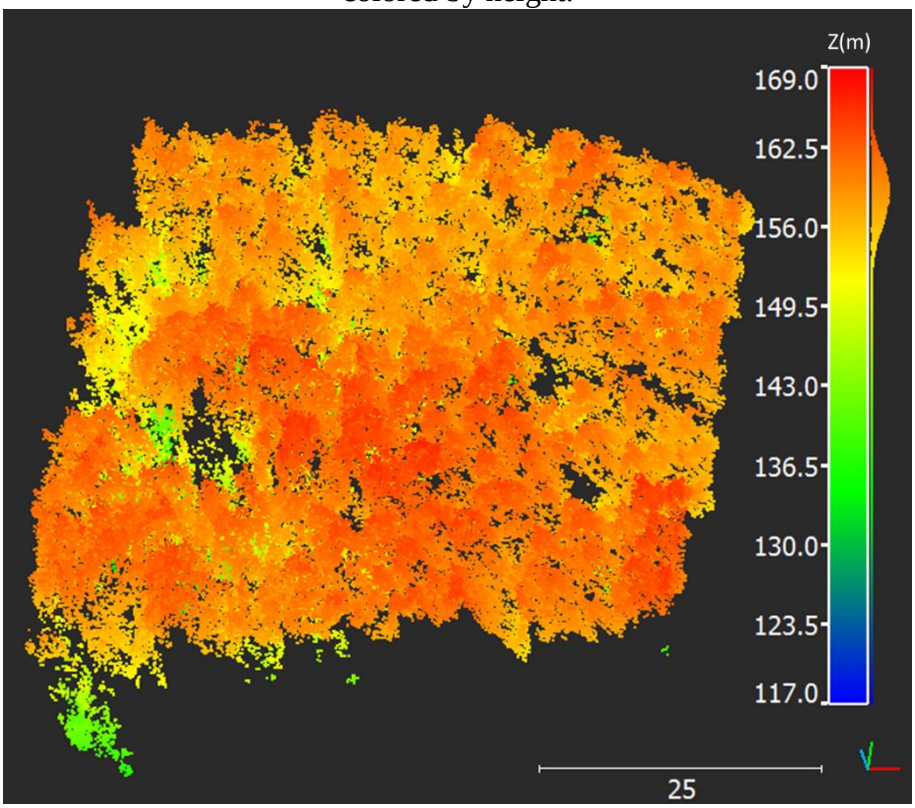

Figure 49: Oblique view of Vesijako test site DSM, generated with HVLL. Points are colored by band 617.5 nm.

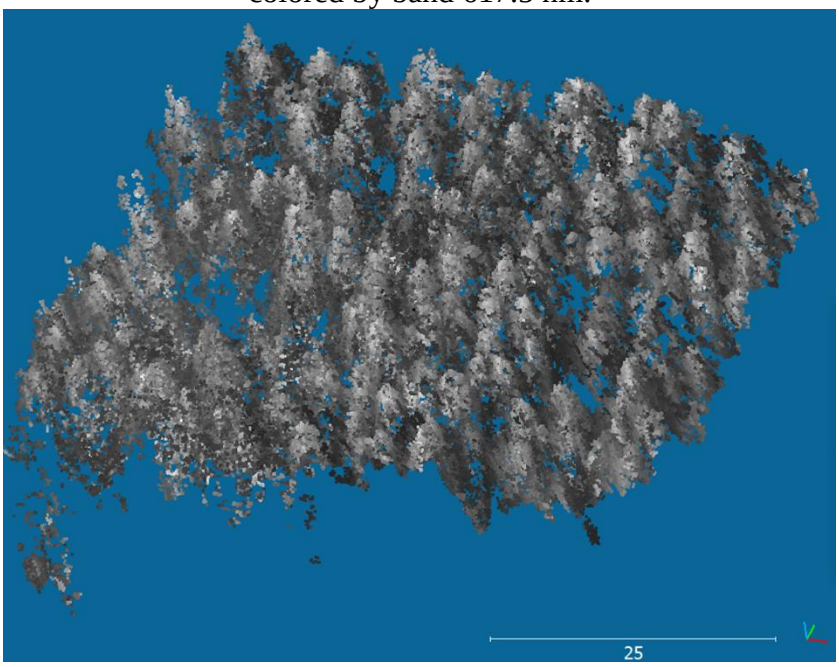

The discrepancies of the PhotoScan and HVLL DSMs were computed using CloudCompare software (Figure 50), module “Cloud-to-cloud Distance” configured to use a local modelling strategy, which is based on the least-squares fitting. The algorithm searches the nearest point in the reference DSM, and then a local model is adjusted on the point and its neighbors. The discrepancies from each point of the compared DSM to its nearest point in the reference cloud is the discrepancy to this model (CloudCompare, 2017). The mathematical model used was a quadratic function with six parameters.

Figure 51 shows the histogram of the discrepancies. From a total of 250753 points, most of differences (84.53%) were smaller than 0.5 m. The average and standard deviation of the difference in height values are equal to 0.30 m and 0.38 m, respectively, which is an acceptable result for a GSD of 9 cm.

Figure 50: Discrepancies between Photoscan DSM and HVLL DSM (Vesijako study area). Points are colored by differences in height. (a) Oblique and (b) Nadir views.

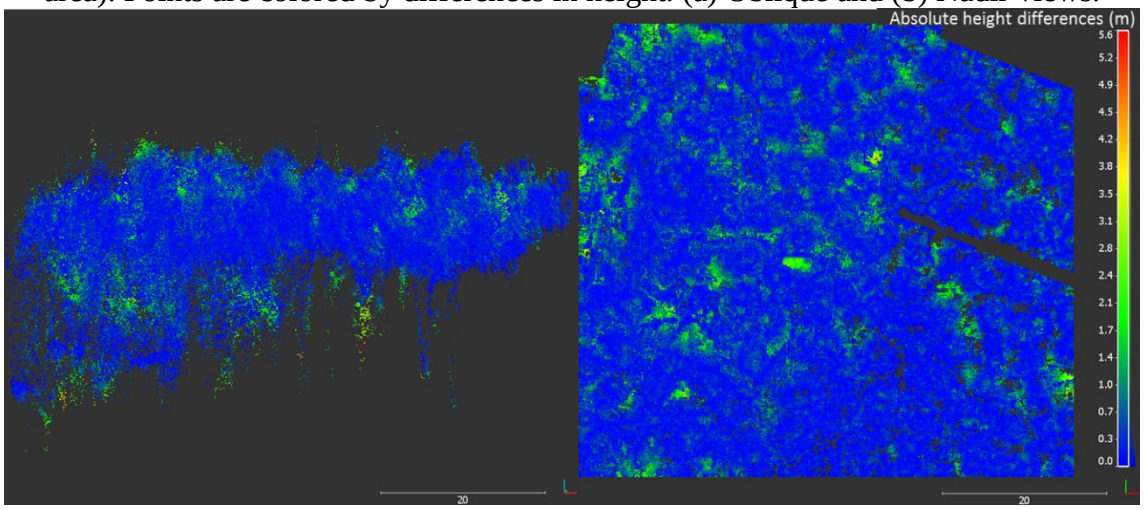

(a) (b)

Figure 51: Histogram of the discrepancies between Photoscan DSM and HVLL DSM (Vesijako study area).

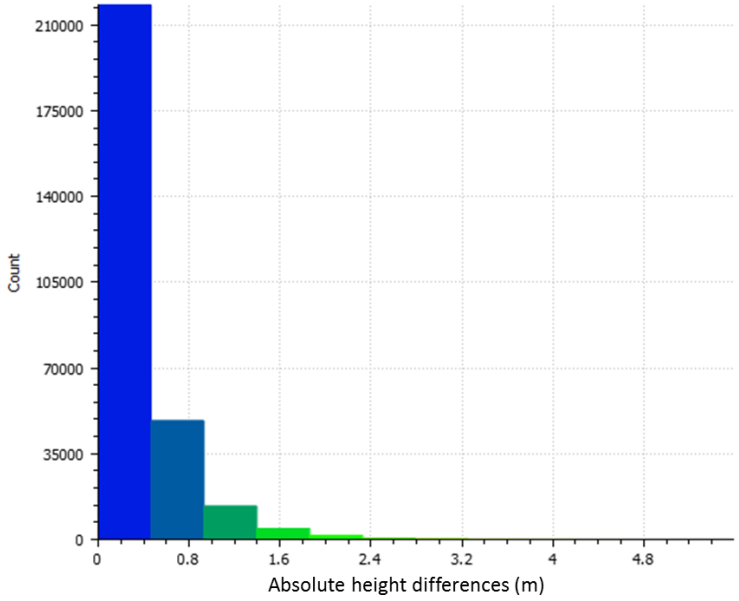

Now, using the method HVLLC (section 7.2.5), the cubes were firstly co-registered taking one of the bands with estimated EOPs as reference and using 2D transformation function. The co-registered cubes were classified using the k-means method, with 10 iterations, 0.95 convergence threshold, and four classes defined based on the forest characteristics (ground-shadow, ground-vegetation, top of the trees and area between top and ground). Figure 52 (a) presents a co-registered band composition. Results of classification with k-means algorithm are presented in Figure 52 (b).

Figure 52: Results of (a) FPI image (RGB composition) of a co-registered cube; (b) Classified cube using k-means.

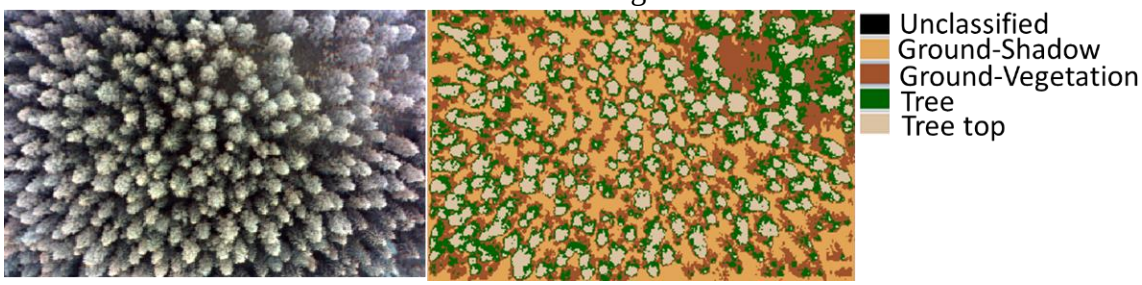

(a) (b)

The HVLLC DSM is shown in Figure 53 (nadir view) and Figure 54 (oblique view) colored by height. The constraints applied to the search space based on the reference classes generated more points at the ground level.

Figure 53: Nadir view of DSM of test site Vesijako, generated with HVLLC. Points are colored by height.

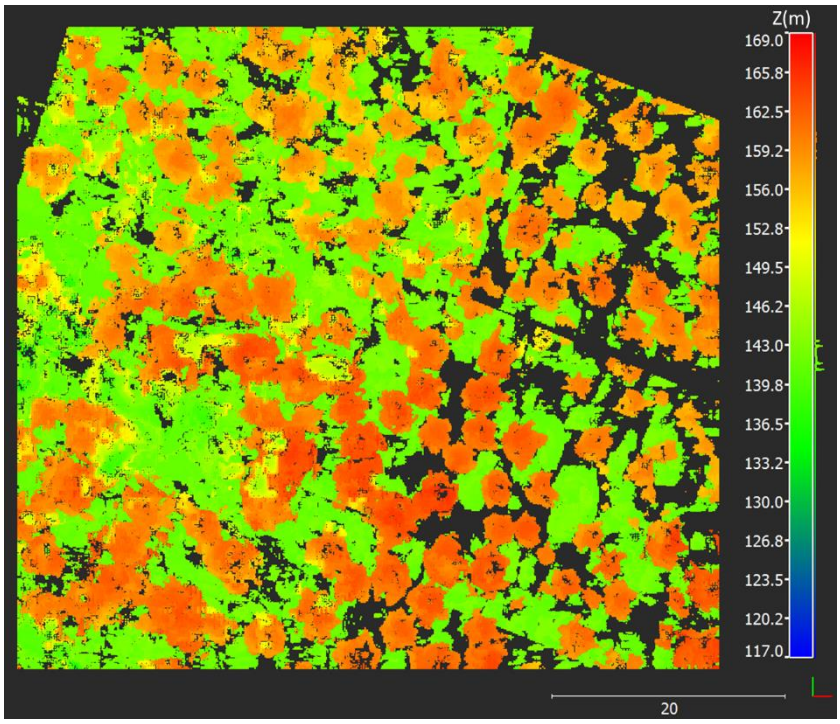

Figure 54: Oblique view of DSM of test site Vesijako, generated with HVLLC. Points are colored by height.

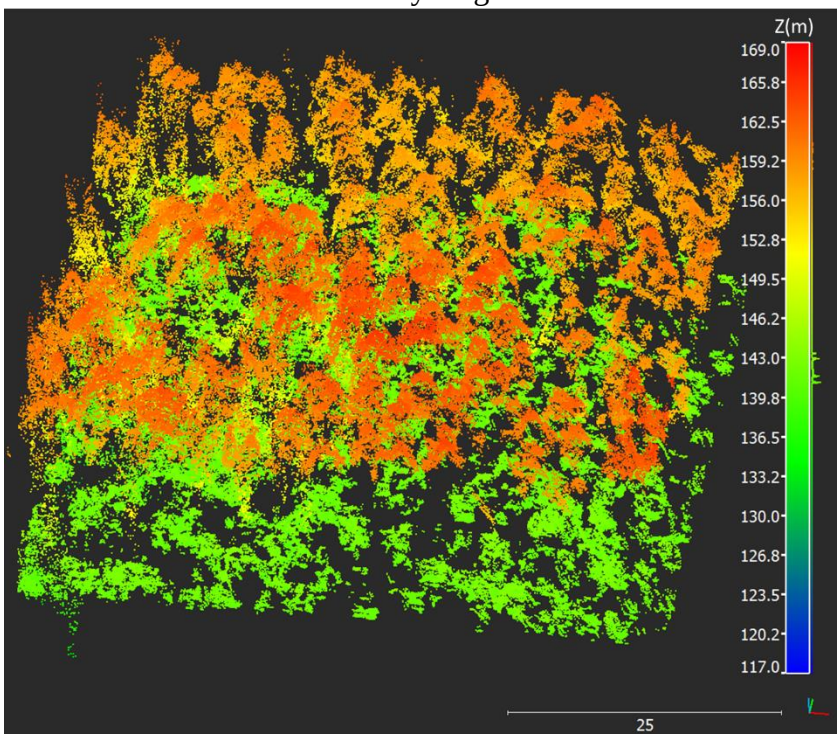

The discrepancies computed between the HVLLC DSM and the PhotoScan DSM are presented in Figure 55 and the histogram of the differences in 249229 points is presented in Figure 56. The average and standard deviation of the height differences are equal to 0.54 m and 0.74 m, respectively. The highest differences were located in the points estimated as ground in the proposed method.

Comparing the DSMs generated using HVLL and HVLLC, the average obtained for the height differences was 0.76 m and the standard deviation 1.38 m (Figure 57). Figure 58 shows the histogram of the differences. Based on the highest difference values location, it can be noticed that the use of reference classes estimated more points in the ground points. Considering the average and standard deviation, the result from HVLLC was more correlated with PhotoScan, since PhotoScan estimated more points in the open areas than the HVLL.

Figure 55: Discrepancies between Photoscan DSM and HVLLC DSM (Vesijako study area). (a) Oblique and (b) Nadir views. Points are colored by differences in height.

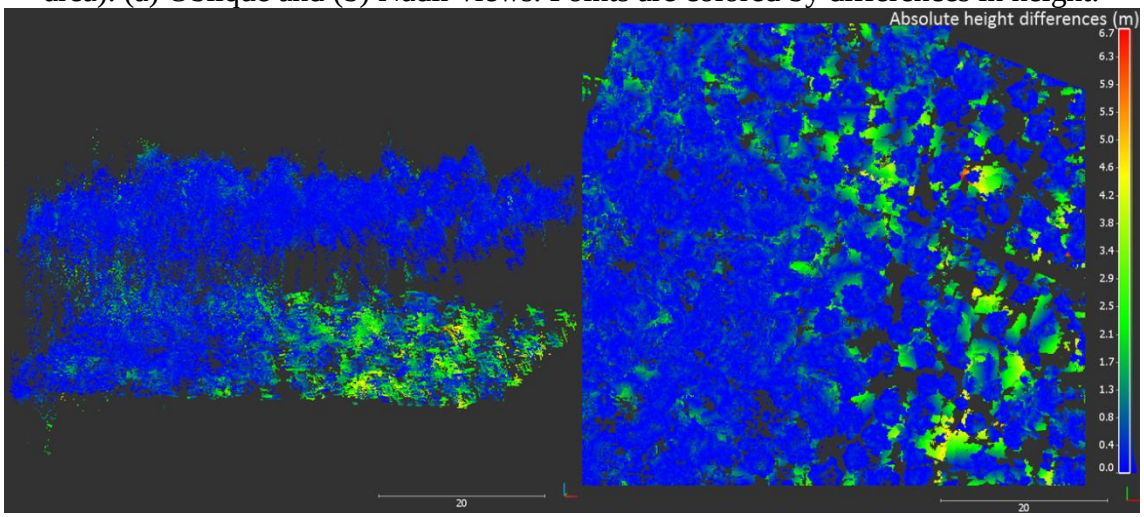

(a) (b)

Figure 56: Histogram of the discrepancies between Photoscan and HVLLC DSM (Vesijako study area).

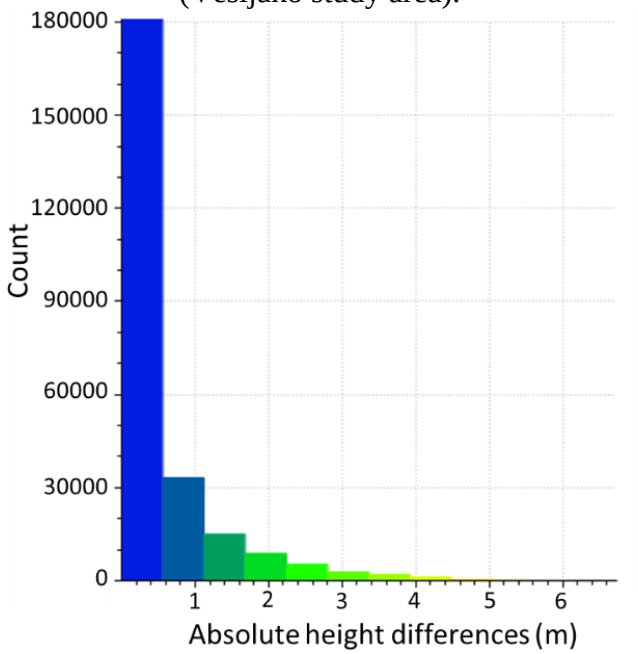

Figure 57: Discrepancies between the HVLL and HVLLC DSM (Vesijako study area). (a) Oblique and (b) Nadir views. Points are colored by differences in height.

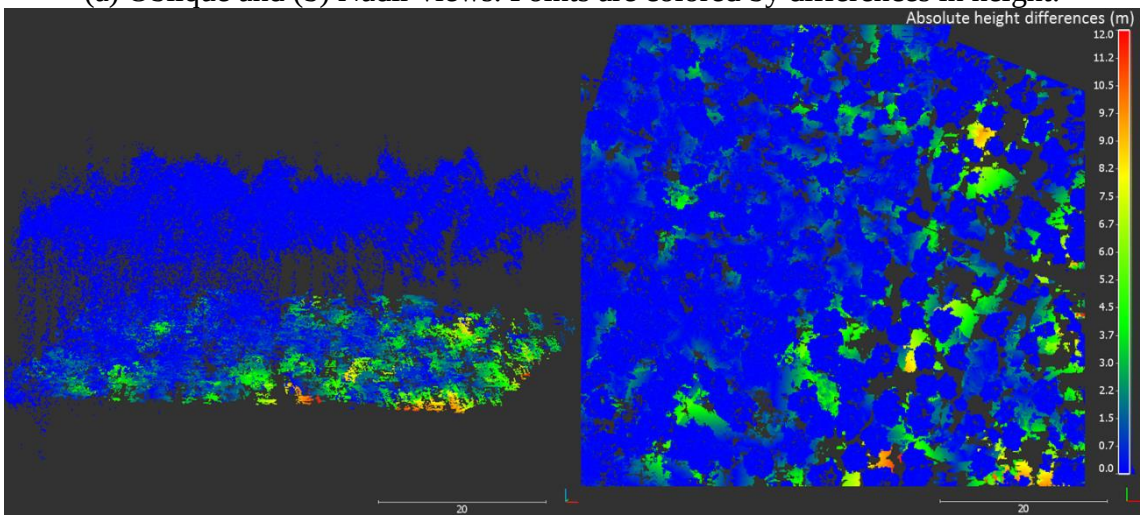

Figure 58: Histogram of the discrepancies between the HVLL and HVLLC DSM (Vesijako study area).

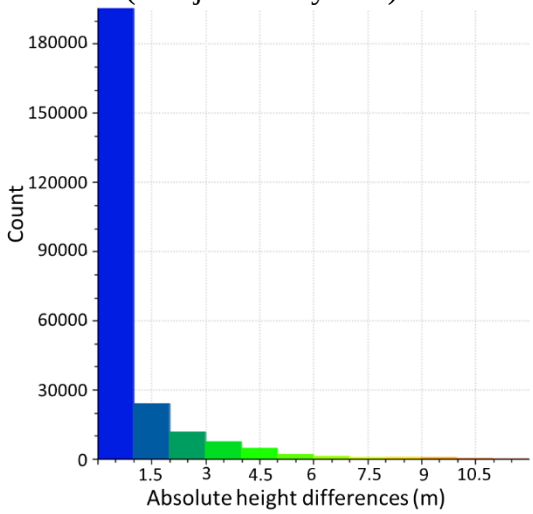

Figure 59 shows profiles extracted from the HVLL and HVLLC DSMs. ALS ground points and PhotoScan DSM profile are also shown. Comparing the HVLL and HVLLC, more points were generated in gap areas with the use of reference classes. However, since forest gaps are usually more homogenous and have lower dynamic range and are observed as shadows (and reduced amount of illumination), there are still false matches and the points are varying in the vertical range given as *a priori* value for the class, which is expected in vegetation.

Figure 59: Two profiles extracted (1 m of width) from HVLL, HVLLC, ALS ground points and PhotoScan DSM of Vesijako study area.

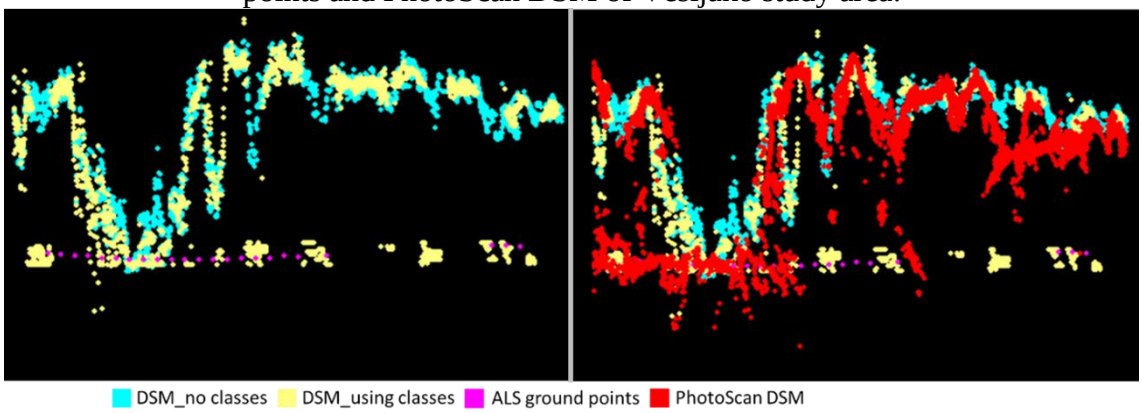

Figure 60 shows the HVLLC points classified with the reference classes from image classification process. This result can be used as a priori classification of the data to extract ground and non-ground points.

Figure 60: HVLLC DSM of Vesijako classified using image pixel classes.

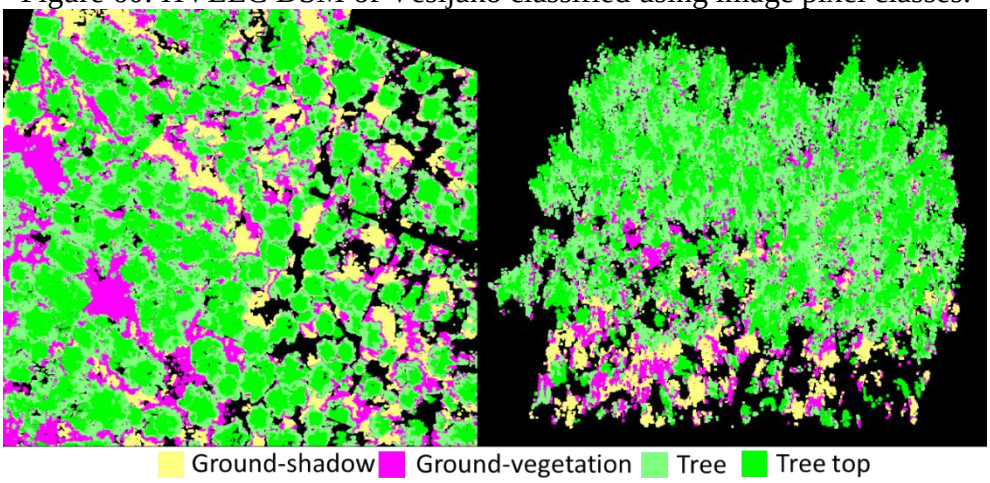

A sample of ALS ground points was used to evaluate the ground points of the DSMs generated from image matching. Considering the difference of time between the ALS and image data acquisition, the ground points more stable to the changes than the point of trees. Thus, only ground points were used in this experimental assessment.

The ALS data was classified to obtain only ground points, using LAStools software, with default parameters. A sample of 87 points was collected over open areas in the ALS classified as ground points. The sample was used to compute the difference of height for the DSMs generated using HVLL and HVLLC, and the DSM generated using PhotoScan. The differences were calculated using CloudCompare cloud-to-

distance tool. The model “least square plane” was selected. In addition, the tool *Lascontrol* from LasTools software was used to compute the differences. The *Lascontrol* module generates a TIN using the DSM to be compared and interpolates the height of the reference points on this TIN. Table 6 shows the average and standard deviation of the height differences computed using CloudCompare and *Lascontrol*.

Table 14: Average and standard deviation of differences between ALS ground sample points and Photoscan DSM, HVLL and HVLLC.

DSM	PhotoScan		HVLL		HVLLC	
	Ave(m)	Std(m)	Ave(m)	Std(m)	Ave(m)	Std(m)
CloudCompare	0.869	0.865	1.723	1.886	0.203	0.187
LasControl	8.317	6.115	12.581	5.319	0.209	2.031

It can be noted that, at the ground level, HVLLC was the most similar with the ALS data. PhotoScan was good in large areas without trees, as can be observed visually in Figure 45. The statistics computed using *Lascontrol* seems to be more compatible with the profiles in Figure 59. In any cases, HVLLC performed better than the conventional HVLL. The use of reference classes showed potential to guide the image matching method implemented.

7.2.2 Using Hyperspectral 2D Frame Images for multiangular spectral DSM generation in tropical dense forest

The study area of this section is located in the Ponte Branca forest fragment and the data set used was PB1 (Plot 6), which characterizes a dense tropical forest area. In the following experiments, the objective is to generate a dense forest model with 3D geometry and multiangular spectral data features, resulting in a HDSM, using the lightweight hyperspectral 2D frame camera.

A set of twelve cubes from the PB1 full block was used for the experiments and the HDSM was generated over an area of 60 m x 45 m. A mosaic of PB1 test site generated using RGB images, from the Sony Nex 7 camera, is presented in Figure 61.

Figure 61: Mosaic of PB1 test site generated from RGB images of Sony Nex 7.

A DSM of the entire block was generated with the PB1 FPI image data using PhotoScan software (Figure 43), as mentioned in Section 6.4, and the selected area was extracted from this DSM to compare with the results. Figure 62 shows the DSM selected from PhotoScan and Figure 63 shows its oblique view. The points are colored by height, from blue to red representing the variation from minimum to maximum values, respectively.

Figure 62: Nadir view of PhotoScan DSM colored by height (Ponte Branca study area).

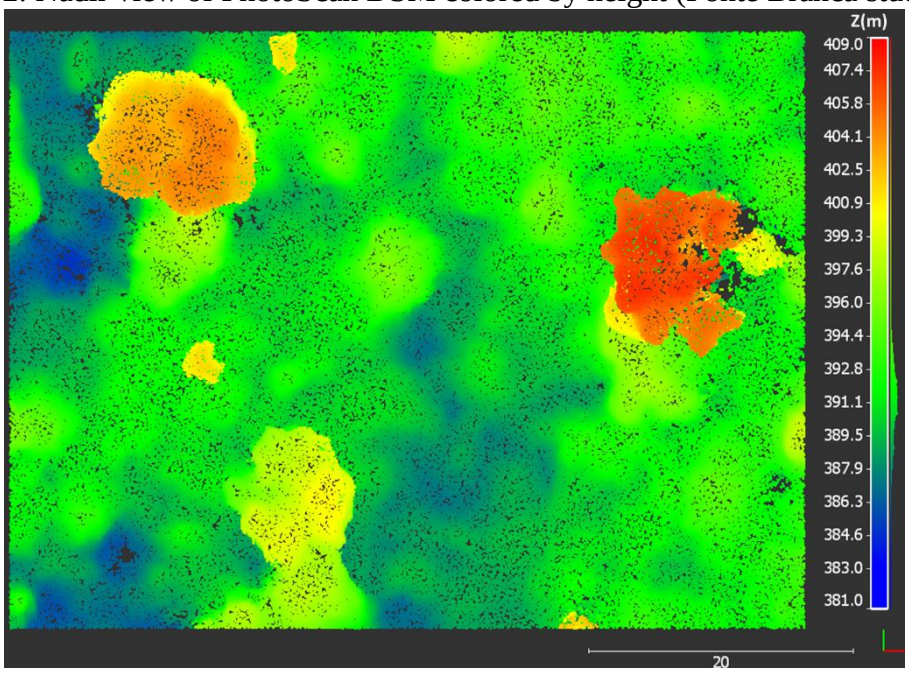

Figure 63: Oblique view of PhotoScan DSM colored by height (Ponte Branca area).

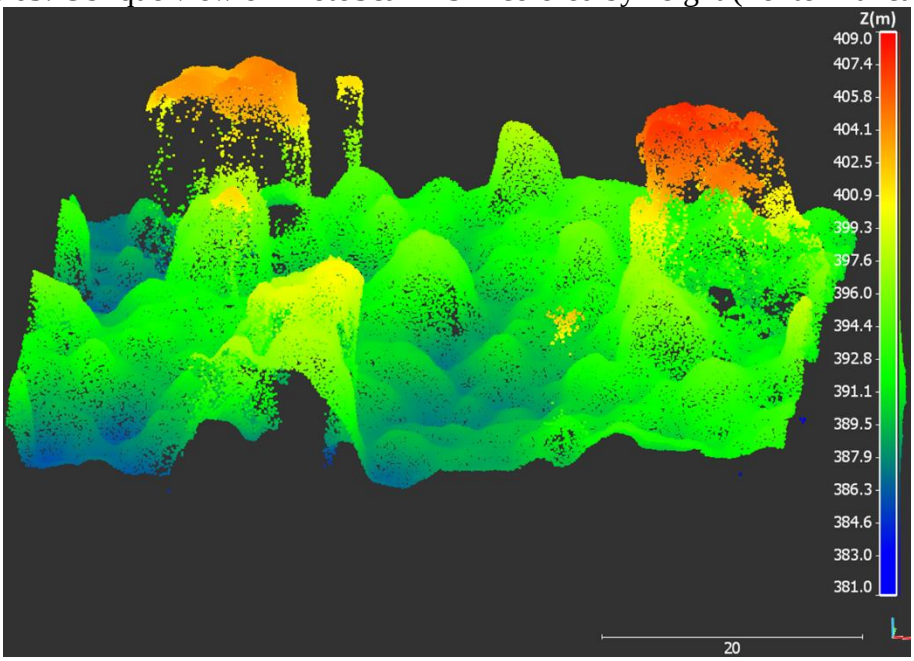

The IOPs of sensor 1 and sensor 2 estimated in Chapter 4 (experiment "Calib S1S2") and the EOPs of the four bands estimated in Chapter 6, with CMC, were used.

The matching method was implemented using rectified windows (7.2.2) and adaptive window size and shape (7.2.3). The multiple bands technique (7.2.4) was also used and configured with four bands.

The DSM resulting from the matching techniques is presented in Figure 64 and Figure 65 (oblique view). Visually, PhotoScan DSM and the developed in-house software DSM appears to have high quality in the 3D reconstruction of the canopy vegetation. In some areas of canopy, the matching did not find correspondence. Most cases happened with the proposed method in object discontinuities as a result of occlusions and shadows. It can be observed that the DSM resulting from the proposed method was able to recover the shape of trees with less smoothing than PhotoScan.

Figure 64: Nadir view of DSM generated with HVLL (Ponte Branca study area). Points colored by height. (a) Nadir and (b) oblique views.

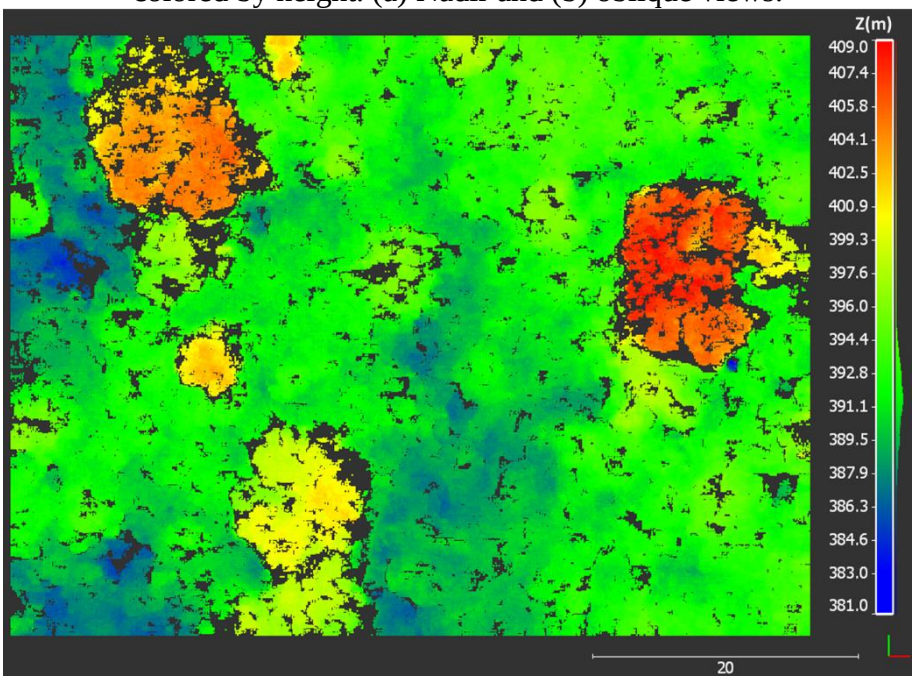

Figure 65: Oblique view of DSM generated HVLL (Ponte Branca study area). Points are colored by height. (a) Nadir and (b) oblique views.

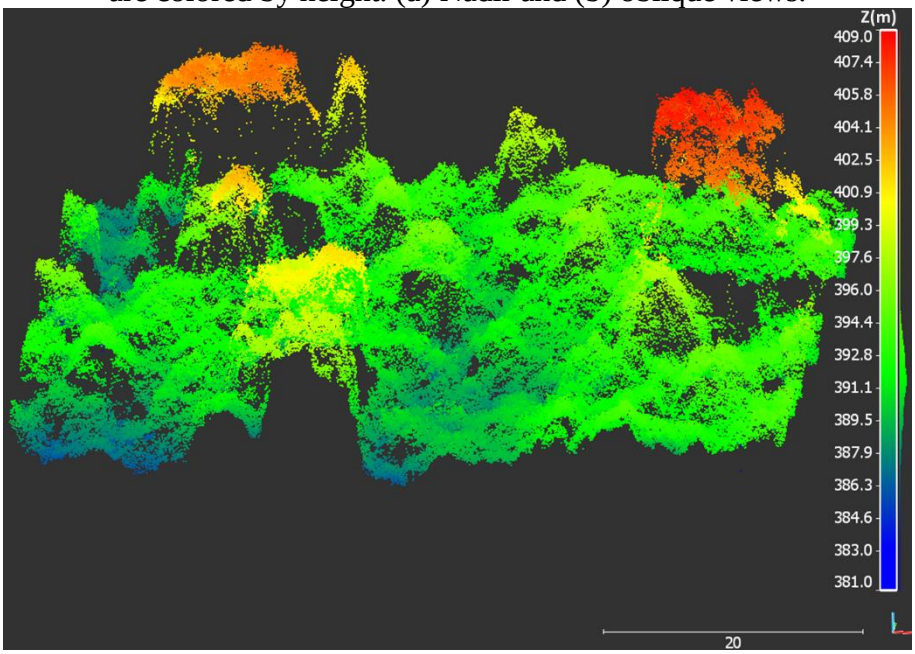

Figure 66 presents the resulting discrepancies computed using CloudCompare software (“Cloud-to-distance” tool). Additionally, Figure 67 shows the histogram of the discrepancies. From a total of 200423 points, most of differences (71%) were smaller than 0.6 m. It is worth noting that some differences from the two software can be also

related to the difference in the EOPs and IOPs of image. The average and standard deviation of the difference in height values are equal to 0.42m and 0.29m.

Figure 66: Discrepancies between Photoscan DSM and HVLL DSM (Ponte Branca study area). Points are colored by height differences. (a) Nadir and (b) oblique views.

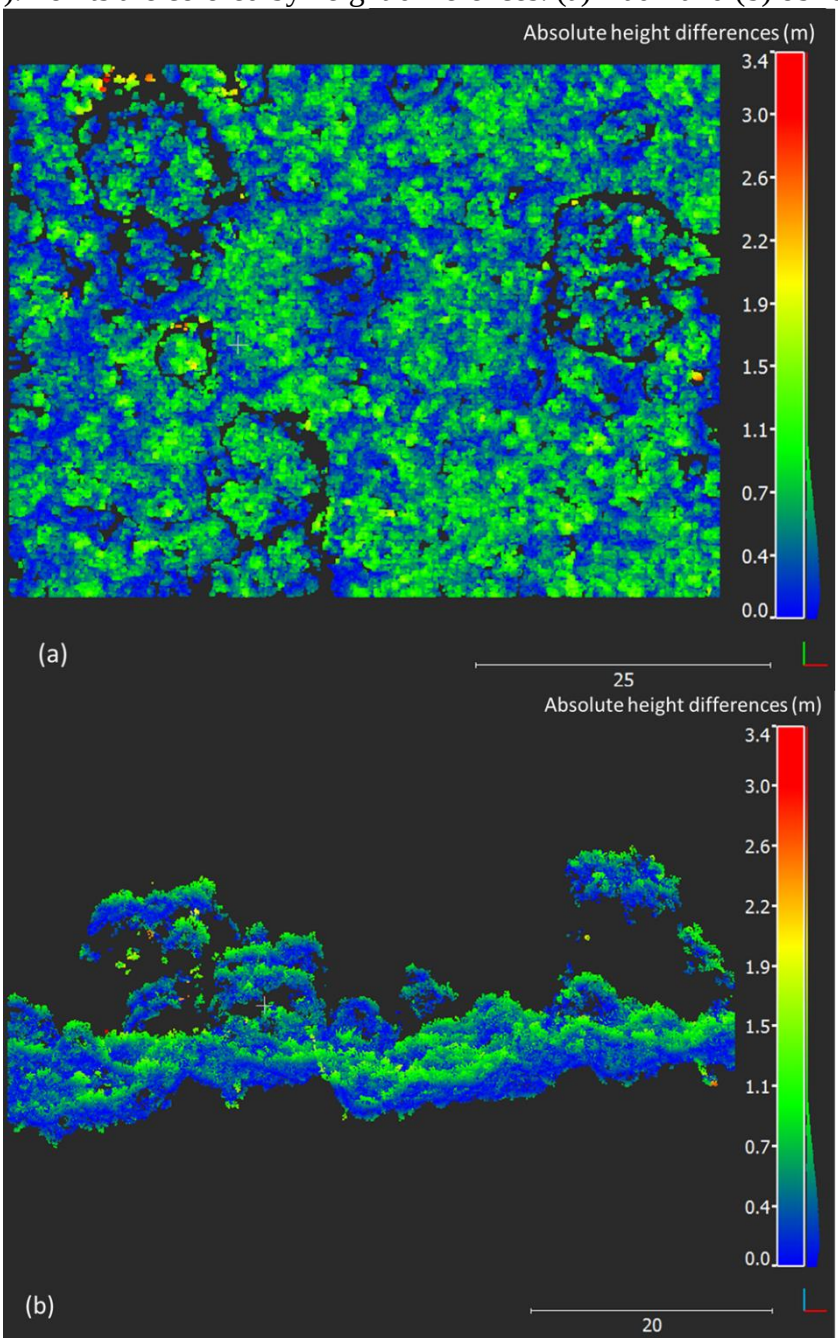

Figure 67: Histogram of the discrepancies between Photoscan DSM and HVLL DSM (Ponte Branca study area).

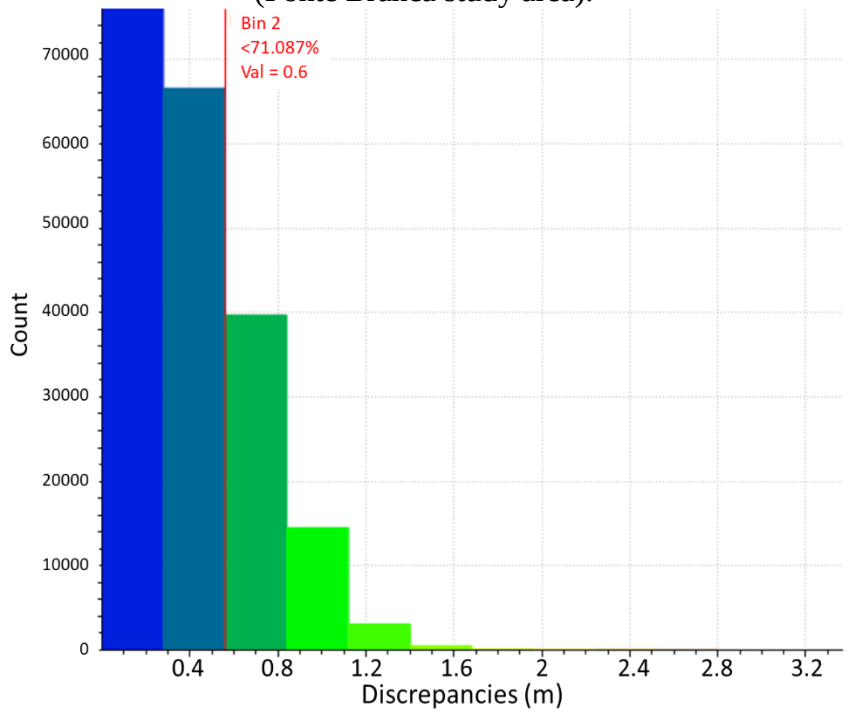

Figure 68 presents the two DSMs after the interpolation to a grid with 0.10 cm of sampling distance. It is observed that the DSM generated with HVLL shows higher mean elevations than the PhotoScan DSM and more details of the canopy structure.

Figure 68: DSMs with grid resolution of 10 cm (a) PhotoScan and (b) HVLL (Ponte Branca study area).

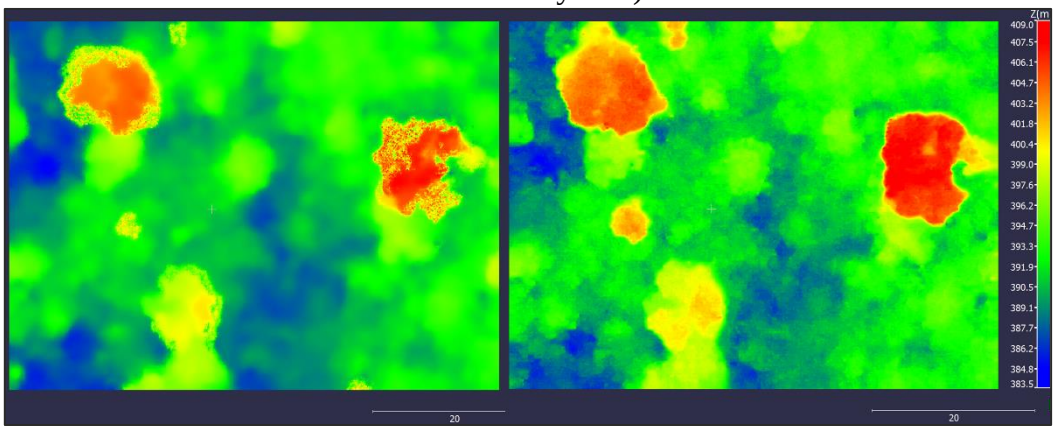

(a) (b)

Figure 69 compares profiles extracted from PhotoScan DSM and HVLL DSM. As it can be seen, the profile extracted are nearly similar to the canopy shape.

Figure 69: Two profiles extracted with buffers width 1 m and 10 m from PhotoScan DSM (yellow) and HVLL DSM (blue) (Ponte Branca study area).

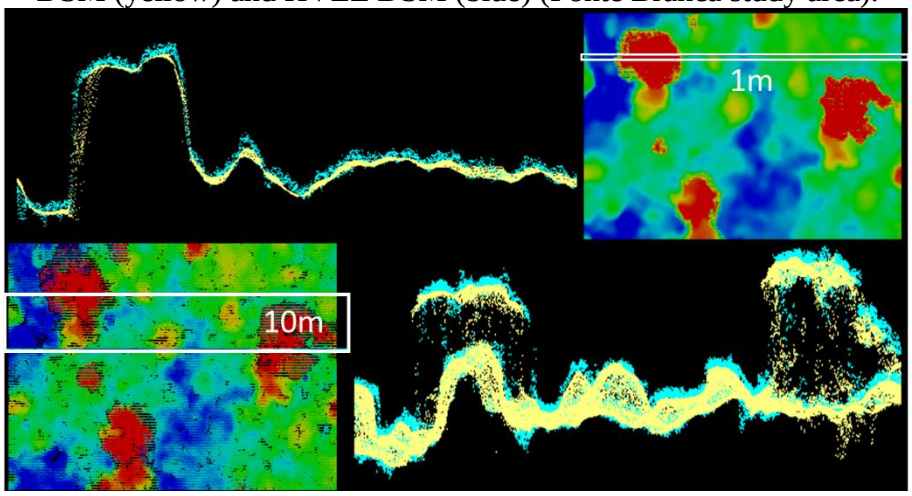

In addition, since HVLL method is being used, the spectral information of each band was assigned to each point of the DSM. Figure 70 shows the HDSM colored by (a) the band 506.2 nm (first band of the cube acquisition), (b) band 819.7 nm (last band of the cube acquisition) and Figure 70 (c) shows the band composition: R(819.7 nm), G(628.7 nm), B(506.2 nm). The spectral information for each point can be also used to compute vegetation indices, such as NDVI. The index can be used as scalar fields for visualization or further analyses of this type of data. In this case, it is appropriated to transform the DN values of the cubes to reflectance values and then input the data in the proposed software for the HDSM generation.

Figure 70: HDSM colored by (a) the band 506.2 nm (first band of the cube acquisition), (b) band 819.7 nm (last band of the cube acquisition) and (c) band composition R(819.7 nm) G(628.7 nm)B(506.2 nm).

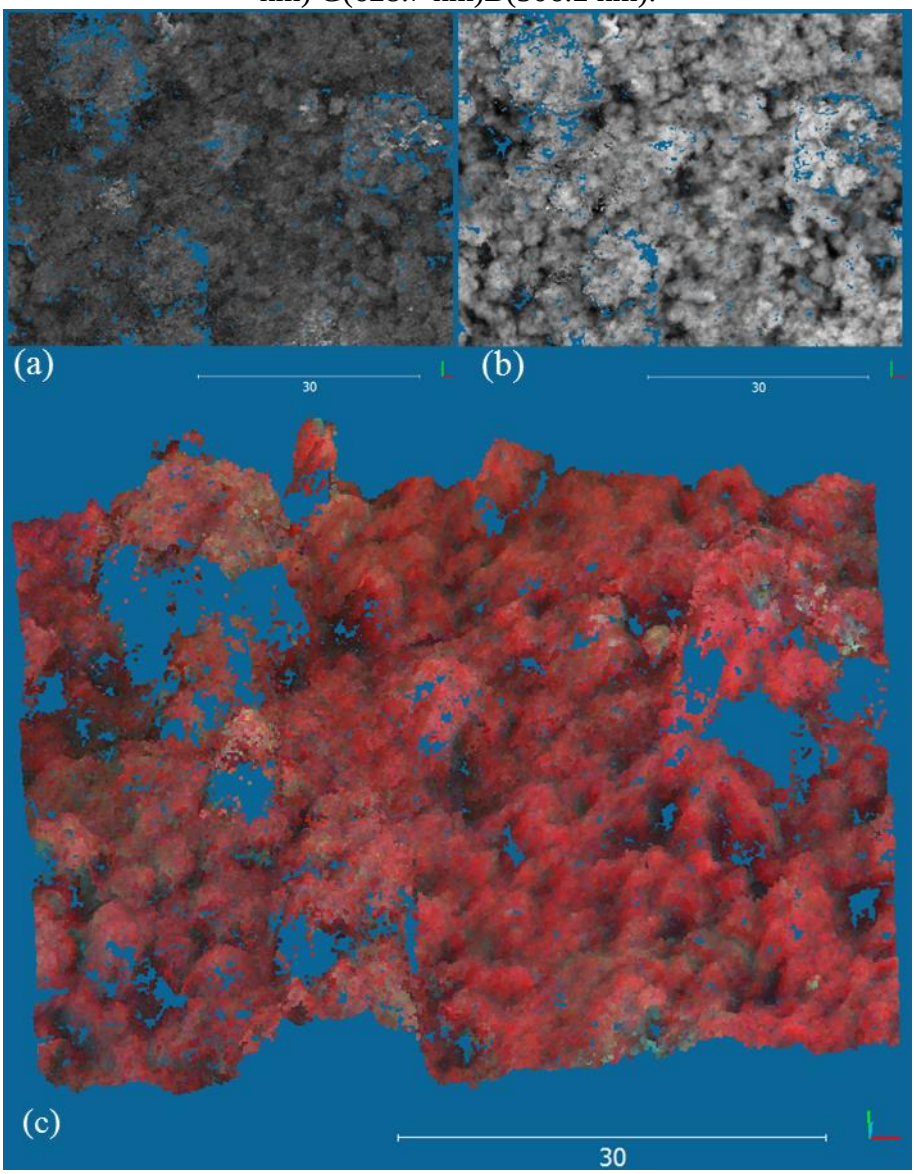

Figure 71 shows one example of the variation in the azimuth and zenith viewing angles for the same point, in four bands of six cubes. As it can be seen, the points have slightly different geometry angles within the same cubes. This feature is important to be considered because it affect the DN values, and consequently the mosaicking process. For these analyses, the Sun geometry of the same day and time of the image data acquisition need also to be used (not represented in Figure 71). Figure 72 presents an example of the output text file with the data recorded in the HDSM.

Figure 71: Sensor azimuth and zenith angles of four spectral bands and six cube for same point, in Ponte Branca data.

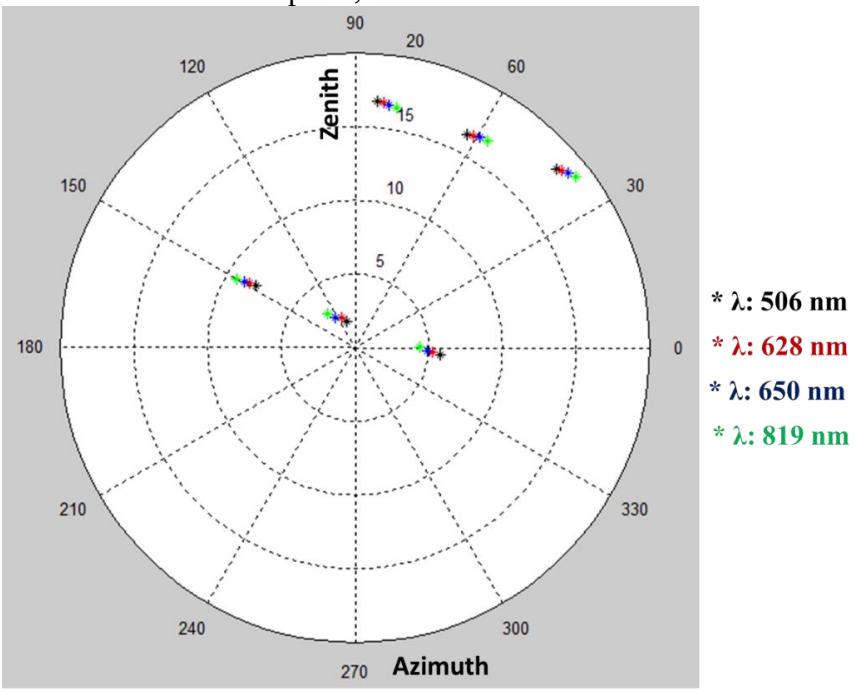

Figure 72: Part of the HDSM output text file.

```
X. Y. Z, Cc. NumCubes. Class. CubeName. AzB1, ZenB1, AzB10, ZenB10, AzB11,
ZenB11, AzB25, ZenB25, DN1, DN10, DN11, DN25
344875.000 7519500.000 389.3329 0.9470 2 0 K00173DAT 122.597282 5.735663
125.989304 5.484842 129.505600 5.264017 135.418228 5.016572 4.278976
3.309737 3.976473 24.620440 K00174DAT 193.175705 5.533515 196.748520
5.762021 200.077164 6.056356 203.548248 6.469501 3.814161 2.972876 3.078206
24.394224
344875.100 7519500.000 389.2429 0.9315 2 0 K00173DAT 122.262215 5.710983
125.652176 5.458342 129.169846 5.235671 135.097809 4.985379 4.723152
3.612087 3.705220 24.751850 K00174DAT 193.270187 5.491635 196.863251
5.720637 200.207214 6.015518 203.689682 6.429391 3.395076 3.106091 3.027105
25.516148
344875.200 7519500.000 389.4086 0.9623 2 0 K00173DAT 121.924644 5.696569
125.312180 5.441669 128.830856 5.216768 134.773743 4.963151 4.694726
3.732304 3.582883 26.587080 K00174DAT 193.366013 5.459464 196.979507
5.689379 200.338898 5.985339 203.832718 6.400660 3.289438 3.116102 3.185675
25.835743
344875.300 7519500.000 388.9220 0.9689 3 0 K00173DAT 121.584587 5.656815
124.969299 5.400760 128.488617 5.174588 134.445999 4.918793 4.312815
3.685934 3.298831 25.886801 K00174DAT 193.463196 5.402810 197.097336
5.632603 200.472229 5.928307 203.977386 6.343264 3.133753 3.342669 2.796041
25.951454 K00175DAT 224.302185 10.449356 225.124847 10.798835 226.320831
11.172146 227.088013 11.663441 3.689688 2.637402 2.321346 25.661713
344875.400 7519500.000 388.8466 0.9692 3 0 K00173DAT 121.242027 5.633404
124.623528 5.375494 128.143097 5.147438 134.114548 4.888710 3.466081
4.162565 4.015395 24.463083 K00174DAT 193.561783 5.361698 197.216751
5.592033 200.607239 5.888334 204.123734 6.304080 3.419827 2.547957 2.900983
24.762119 K00175DAT 224.453979 10.416359 225.273651 10.766139 226.467331
11.139941 227.229889 11.631474 3.022143 2.754370 2.722960 22.287992
344875.500 7519500.000 389.1413 0.9349 2 0 K00173DAT 120.896965 5.624535
124.274849 5.364124 127.794266 5.133615 133.779327 4.871254 2.554057
3.232709 3.576057 23.247948 K00174DAT 193.661789 5.334251 197.337799
5.565732 200.743958 5.863401 204.271759 6.280981 3.354735 2.398423 2.714763
22.907896
```

However, since forest gaps usually have poorer dynamic range and lower image quality due to the presence of shadows (reduced amount of illumination), there are still missing matches as is highlighted (red circles) in Figure 73.

Figure 73: Areas of .gaps (a) RGB mosaic and (b) HVLL DSM colored by band 819.7 nm.

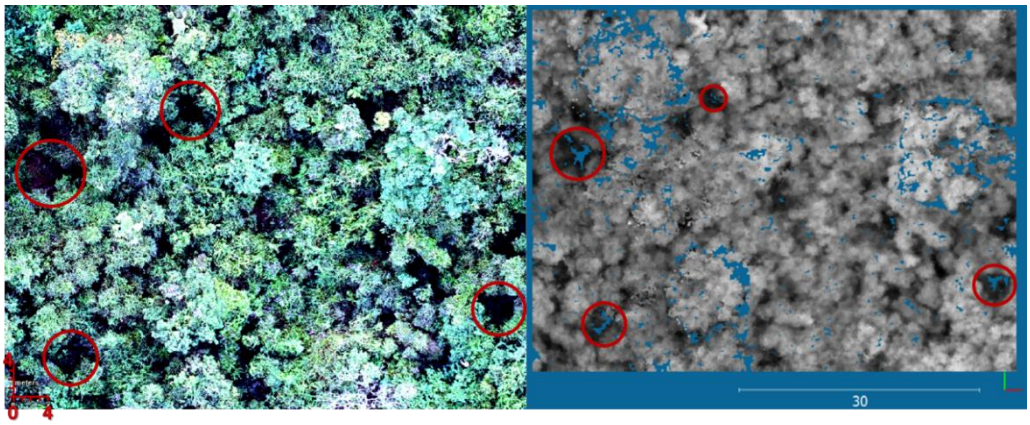

(a) (b)

Aiming to improve the determination of points in such areas and also labeling these points, the HVLLC (section 7.2.5) was used. The twelve cubes were first coregistered using 2D transformation. Then, registered cubes were classified using the k-means method. Four classes were considered suitable for this type of forest scenario, and only the class representing shadow areas was used in this application. Figure 74 shows a band composite of two registered cube and its classification using k-means.

Figure 74: Results of (a) FPI image (RGB composition) of a co-registered cube; (b) Classified cube using k-means.

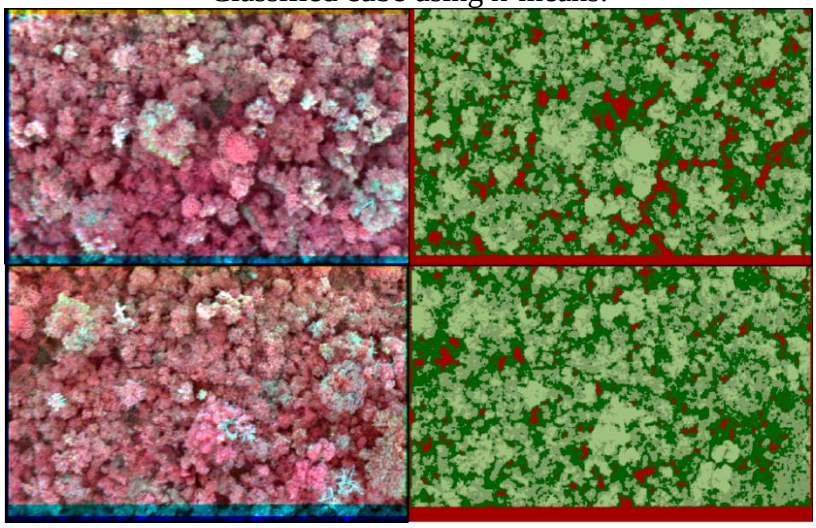

(a) (b)

The DSMs generated using HVLLC is presented in Figure 75 and in Figure 76 (oblique view), colored by height. The constraint applied to the matching based on the object classification have produced more points at the ground level. The HVLLC DSM was compared with Photoscan, and with the HVLL DSM using CloudCompare. The discrepancies computed between PhotoScan and HVLLC DSMs are presented in Figure 77 and the histogram of the 224343 point differences is presented in Figure 78. The average and standard deviation of the height differences were equal to 0.61 m and 1.02 m, respectively. The discrepancies between HVLL and HVLLC DSMs obtained average of height discrepancies equal to 0.08 m and standard deviation equal to 0.54 m (Figure 79). Figure 80 shows the histogram of the differences. For both analyses, PhotoScan-HVLLC and HVLL-HVLLC, the highest difference values were located in gap areas. The use of HVLLC compared with HVLL have not considerable changed points over the canopy, since only one class was used in in this type of forest.

Figure 75: Nadir view of Ponte Branca study area DSM, generated with HVLLC. Points are colored by height.

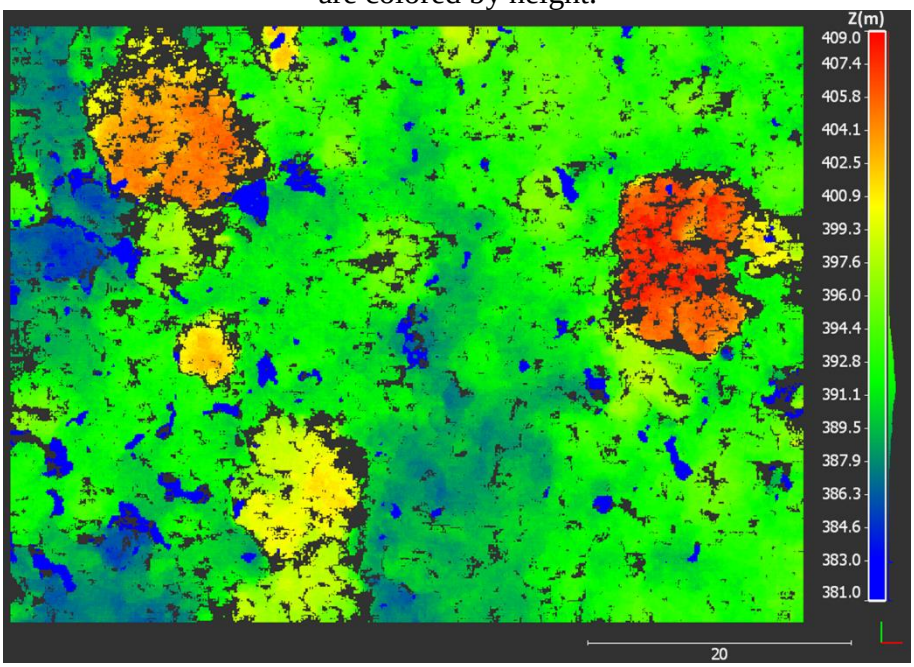

Figure 76: Oblique view of Ponte Branca study area DSM, generated with HVLLC. Points are colored by height.

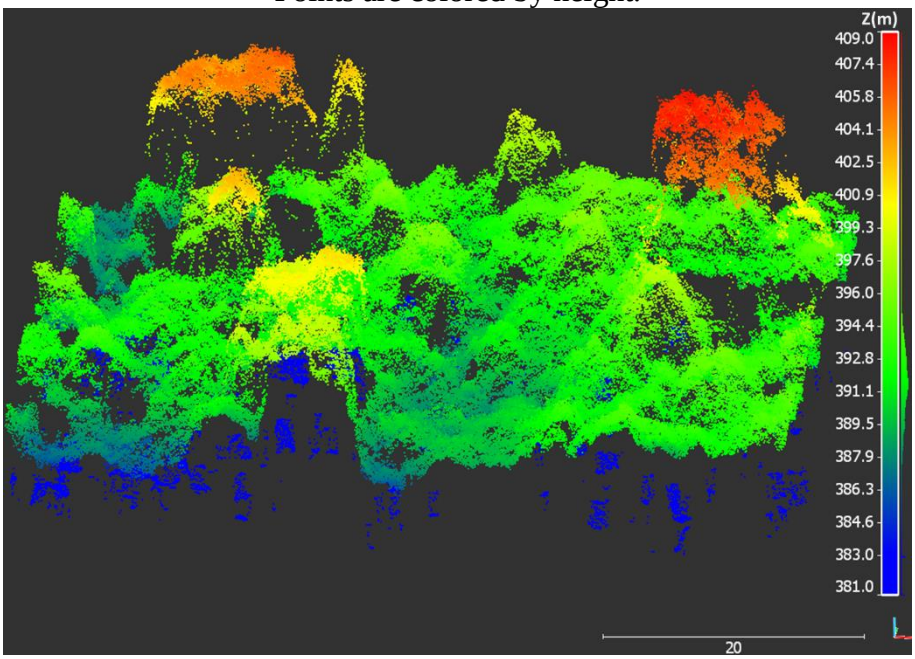

Figure 77: Discrepancies between Photoscan DSM and HVLLC DSM (Ponte Branca study area). Points are colored by height differences.

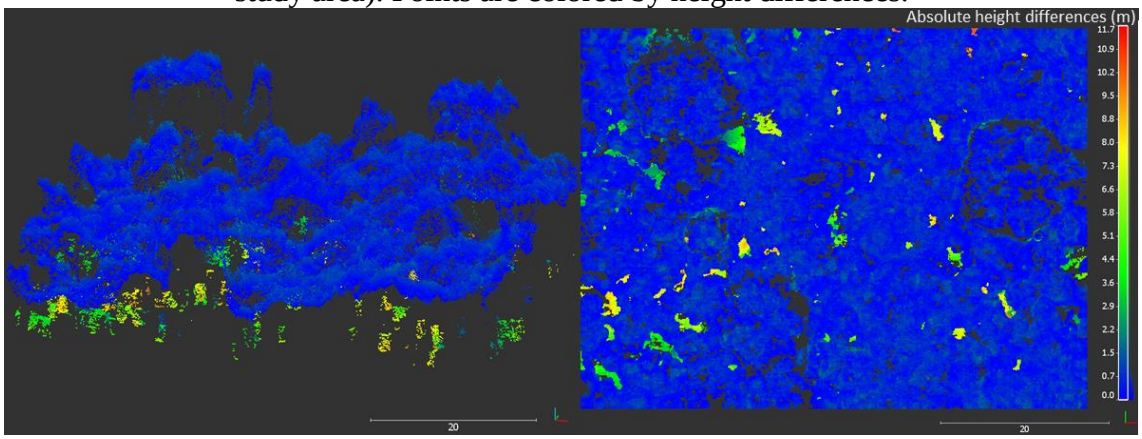

Figure 78: Histogram of the discrepancies between Photoscan DSM and HVLLC DSM (Ponte Branca study area).

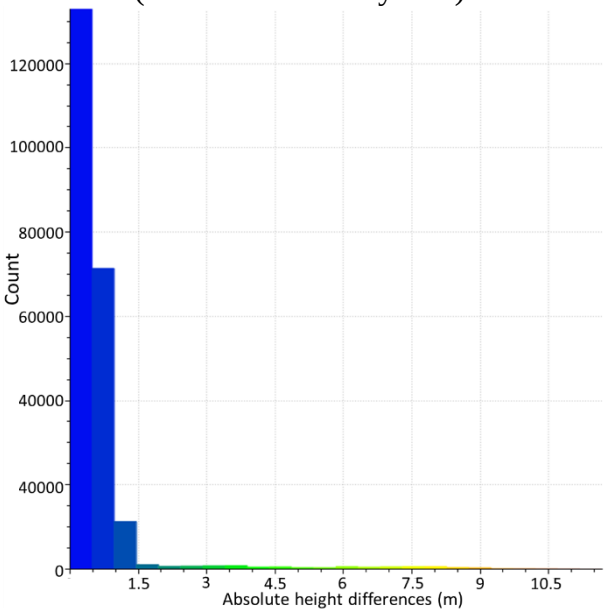

Figure 79: Discrepancies between the proposed methods HVLL and HVLLC (Ponte Branca study area). Points are colored by absolute height differences.

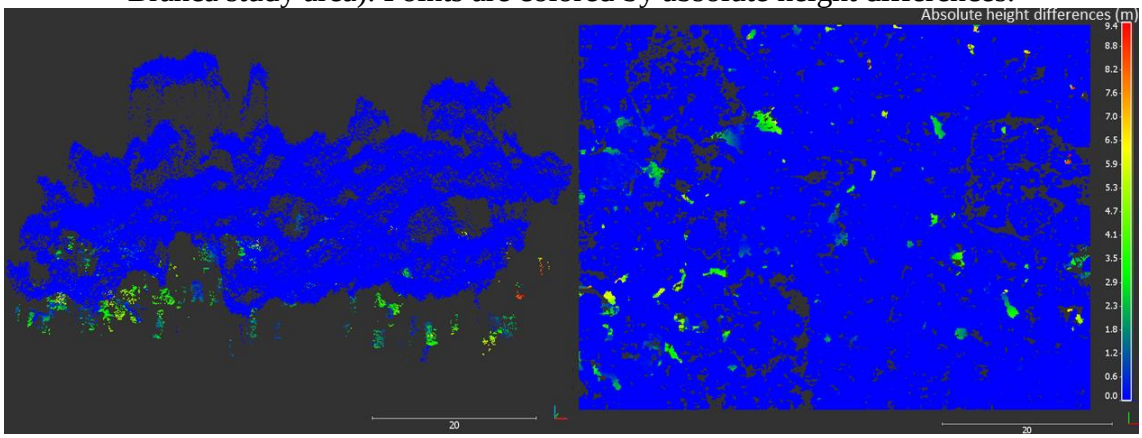

Figure 80: Histogram of the discrepancies between HVLL and HVLLC DSM (Ponte Branca study area).

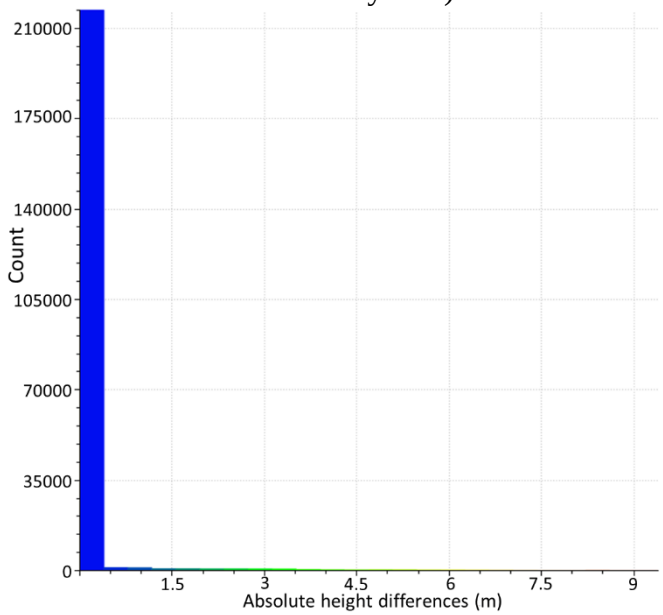

In Figure 81, the HVLLC points are colored by the pixel image class. The HVLLC method increased the number of points in areas of gaps with shadows. It is difficult to determine the quality of the estimated height in these areas, since no accurate reference data is available. However, these areas were labeled, which can be useful to locate gaps in forest and quantifies them or also compute their sizes. The spatial distribution and size of gaps, whether induced by management or by natural causes, generally regulates the below-canopy supply and spatial distribution of solar energy, water and nutrients (KOUKOULAS and BLACKBUM, 2004; GETZIN et al., 2014).

Figure 81: Nadir (a) and oblique (b) view of Ponte branca study area DSM, generated with HVLLC. Points are colored by class. Green indicates high vegetation and brown indicates possible gaps.

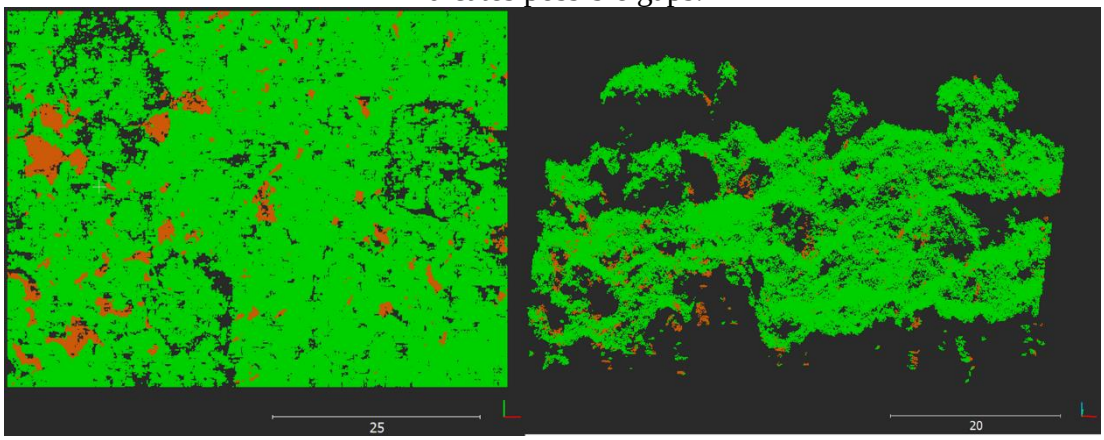

(a) (b)

7.3 Discussions and conclusions

The study of the DSM generation in forest areas, using dense image matching applied to hyperspectral 2D frame images acquired by small-format RPAS was described. Experiments were performed using two forest areas, having different structural characteristics for the DSM generation process. The first area was in a boreal forest, which has tall trees with relatively similar heights, but large variation of depth between each tree since there were gaps with bare soil. The second area was in a tropical forest presenting dense canopy area, with some high trees of large crowns, high diversity of species, and rare areas with (or any) visible bare soil. The objective of selecting these areas was to verify how the implemented method behaved with respect to these major issues for the image dense matching methods.

The visual analysis of the results confirmed that the proposed methods have potential to generate suitable DSMs in complex areas, such as forests. The DSM generated using HVLL provided more spurious points than the DSM of the commercial software, which had more smoothed points due to the use of regularization functions.

Regarding the introduction of image classification information, HVLLC, the results showed that the classes enabled to guide the algorithm in determining the matching parameters with better quality for points over bare soil. Furthermore, the image classification can provide initial classification for the 3D points of the DSM. The HVLLC DSM generated in boreal forest had similar quality to the ALS data. On the other hand, it has also spurious points due to classification errors and homogenous texture. Feasible classification methods for different cases need to be elaborated. Furthermore, a good *a priori* knowledge of the area is required to input the suitable image matching parameter.

The development of a all-in-one matching methods providing both 3D object surface and spectral information was described and showed that the method can provide powerful object characterizing tool that are useful in wide variety of earth measurement problems. Quantitative geometrical analysis of the DSM in tropical area could not be performed because reliable reference data was not available.

8. OVERALL CONCLUSIONS

8.1 Summary

In this thesis, an integrated method for generation of multiangular hyperspectral data and digital surface models (HDSMs) from hyperspectral 2D frame images was developed and assessed. The developed method can be used for various multi- and hyperspectral 2D sensors, with registered or non-registered bands. The novel miniaturized hyperspectral 2D frame cameras are highly interesting in remote sensing applications, as they are low-cost, light-weight, provide high spatial resolution, and most importantly, they collect spectral bands with 2D frame geometry. This last feature allows stereo measurements and thus the generation of HDSMs directly from the same sensor data. The proposed process generates the hyperspectral 3D data in a simultaneous and rigorous process.

The hyperspectral camera used in this study is based on tunable FPI technology, which does not acquire bands of cubes at the same exposure time. Consequently, position and attitude angles of the bands vary along the cube. Due to these camera features, the main steps of the photogrammetric processing chain to achieve the objective of generating HDSMs using FPI cameras were adapted and assessed.

A comprehensive analysis of the geometric calibration of this kind of a Fabry-Pérot interferometer (FPI)-based hyperspectral frame camera was performed and described (Chapter 4). The primary objective of this part of the study was to investigate the determination of the IOPs of the FPI-based hyperspectral frame camera, using bundle adjustment with a self-calibration procedure and to investigate the behavior of the IOPs for different air gaps of the interferometer. The main conclusions were:

- Self-calibrating bundle adjustment with the Conrad-Brown distortion model was suitable to the accurate estimation of IOPs of the FPI camera model with two CMOS sensors;

- The IOPs of different bands (consequently, different air gaps) in the same CMOS sensor did not change significantly, showing that one set of IOPs can be used for each band. However, the IOPs for each sensor were substantially different, thus it was concluded that it is more appropriate to determine different IOPs for each sensor;
- The estimated IOPs (in Chapter 4) were assessed using images captured from a mobile RPAS platform and the results showed that the laboratory parameters were suitable for the BBA.

A band co-registration procedure is required for the utilization of the hyperspectral data cubes from the FPI hyperspectral 2D frame cameras onboard a moving platform. Thus, an evaluation of different 2D geometric transformations for the co-registration of the FPI camera's spectral bands was carried out (Chapter 5). In the experiment using simulated flat area and no flat area, the best transformation function was the second order polynomial 2D transformation, which presented image coordinate RMSEs varying from 0.3 to 0.4 pixels in flat areas and from 1.88 to 3.6 pixels in areas with 30% of depth variation. The RMSE for real scenarios can expect to be higher. Thus, it was concluded that the band registration using 2D transformations is not suitable mainly due to the relief displacement effects. Possible operational solutions to reduce this problem, when using 2D transformations for band co-registration, is using low flight speed depending on the object height variations or to adjust the GSD to meet the registration accuracy (TOMMASELLI et al., 2015). 3D transformation function using 3D surface model was the most indicated to perform the HDSM generation, as investigated in Chapter 6, subsection 6.4.1. However, the quality of the band co-registration using 2D map functions was considered sufficient for the initial image classification process of the FPI cubes.

This study also assessed the determination of the FPI image EOPs for complex forest areas, with limited access and without open areas to set GCPs. The Brazilian forest was a good example of this challenging, where GCPs were only surveyed outside the forest and they were concentrated in the beginning of the strip. Besides, the limited flight time due to the RPAS operational configurations and the plot area distance from the border of the forest resulted in image blocks with one or two strips (Chapter 6). Thus, combining GNSS of the exposure stations data was significantly important in Brazilian forest areas. The use of more than one band increases the overlaps and

generate more reference bands for the cube 3D registration. The results showed that EOPs could be accurate estimated using SfM with self-calibration.

Additional analysis to assess the quality of the estimated EOPs of the remaining bands were performed using linear interpolation and 3D band matching technique proposed by Honkavaara et al. (2017). The EOP estimated by linear interpolation generated RMSEs of the check points image coordinates up to seven pixels, while for the 3D band matching technique the RMSEs were smaller than one pixel. The results also showed the importance of selecting suitable reference bands. Mainly, the spatial distance between the bands needs to be taking into account.

After having investigated and assessed the geometric processing of the FPI camera data, the main objective was to study, implement and evaluate a methodology for generation of HDSM, using object space matching approach with multiple bands and using adaptive parameters based on image classification data.

The VLL method was used to reduce the search space in the process of image matching, from the object space to the image space and it was named hyperspectral VLL (HVLL). Correlation coefficient score was suitable even with the spectral differences between the bands, and it was used in the image matching process considering spectral bands of different cubes and between bands of the same cube (if more than one band is set up to be used).

The hyperspectral data was used to obtain classes from the hyperspectral cube classification. These classes were used to adapt the image matching parameters (hyperspectral VLL classes - HVLLC), taking into account the characteristics of each class to change, for instance, the correlation coefficient threshold. The HVLLC technique provided the estimation of more points in ground areas, which usually are in the gaps of the canopy. A disadvantage of HVLLC process is the requirement of prior knowledge about the area (for example, information of tree average heights). In the execution of the experiments, empirical tuning must be performed, in order to achieve the best parameters, varying the window size for each class, the acceptance threshold values and the size of the search space in the height.

This study demonstrated and implemented an integrated approach to generate multiangular hyperspectral 3D surface model, which contain for each point: 3D coordinates, spectrum data of the cubes used in the height estimation and viewing angle geometry of the cubes used in the height estimation. The advantage of the integrated process, as developed and suggested in this study, is to provide in the same process the

main data used for remote sensing investigations, avoiding the use of different software packages, which can have implemented incompatible models for the data process and not always provide a documental explanation about the algorithms. The point in the object space is being properly projected to the corresponding spectral bands. The method implemented applies the information of the images that have sufficient matching score to project the spectral data and to compute the viewing angles. As a result, occlusion errors are reduced when recovering the spectral data to the point. The method also recovers the multiangular geometry by computing the viewing azimuth angle and viewing zenith angle of the ground points and multiple camera positions. This information is fundamental to the study and correction of reflectance effects caused by the viewing angular dependency and providing more features to the vegetation characterization (BURKART et al., 2015; ROOSJEN et al., 2017).

The HDSM generated was geometrically compatible to the DSM generated using a commercial software and better in some cases. ALS data was not available for additional geometrical quality analyses of Brazilian data and the Finnish ALS data was acquired two years before the FPI image data. The processing chain showed to be suitable for the HDSM generation of the boreal forest (Vesijako) area and the tropical Atlantic forest area (Ponte Branca).

The current method proposed and the results showed to be suitable for the generation of 3D data connected with multiple spectrum and multiangular information. This data has a great potential in remote sensing researches, although this was just the start of other issues that need to be addressed. The method implemented is object space based, thus the projection of the point to the image space gives a good approximation of the point location; however, errors in the image orientations can affect the quality or increase the search space. The use of a search in the epipolar lines, as well as, considering the exterior orientation parameters quality can reduce these drawbacks. Other methods to improve the point-image visibility/occlusion verification is still a topic to be studied and implemented. A disadvantage of using a regular grid is that only one point can be estimated per planimetric grid position. Adaptation of this method could be done by using irregular grids or multiple cells for each grid point.

In contrast to image space-based DSM generation methods, for instance in PhotoScan, the HVLL method can be considered simpler since it is object space-based and therefore the point's 3D coordinates are directly obtained without extra computations required in the image space based algorithms, such as disparity map

fusion and point cloud merging steps. However, the use of optimizations and parallel processing techniques to increase the computing speed is recommended. Besides, a study to compress the large amount of data in the HDSMs (increasing with the size of the area, the overlaps and the number of bands), combined with the use of standards for the outputs, will be performed, which ease further use in other applications.

Quality assessment of the resulting HDSM using spectral reference data provided from other sensors is also an important task in order to use this data for analysis, such as estimation of vegetation parameters or vegetation classification.

8.2 Conclusion

This study described an approach to simultaneously generate 3D information integrated with multiple spectral and viewing angle geometry, using dense image matching applied to hyperspectral 2D frame images acquired by small UAVs. Furthermore, a technique to improve the tuning of matching parameters based on reference classes from the classification of the hyperspectral images was proposed. Experiments were performed using UAV-borne image data sets captured using tuneable filter based sensor from a dense tropical forest in Brazil and a sparser boreal forest in Finland. The results show that the proposed technique can be used to generate 3D information compatible with the accuracy of mainstream commercial software. Furthermore, advantages of the proposed method include simultaneous calculation of multiangular hyperspectral data and better quality for points in forest gaps. The 3D hyperspectral data from the RPAS remote sensing system can provide insights and data for several types of forest studies, such as successional stage, biomass estimation, species classification and monitoring of biodiversity and health, and is especially valuable in studies regarding the preservation of the tropical forest fragments. This low-cost and lightweight system can be easily used for temporal data acquisition by providing data with very high spatial and temporal resolutions. Consequently, the development of an all-in-one matching method providing both 3D object surface and multiangular spectral information directly from hyperspectral images is a powerful object characterizing tool that will be useful in a wide variety of earth measurement problems.

REFERENCES

AASEN, H.; BURKART, A.; BOLTEN, A.; BARETH, G. Generating 3D hyperspectral information with lightweight UAV snapshot cameras for vegetation monitoring: From camera calibration to quality assurance. **ISPRS Journal of Photogrammetry and Remote Sensing**, v. 108, p. 245–259, 2015.

ABDEL-HAKIM, A. E.; FARAG, A. A. CSIFT: A SIFT Descriptor with Color Invariant Characteristics. In: Computer Society Conference on Computer Vision and Pattern Recognition. **Proceedings….** 2006, v. 2, p. 1978-1983.

ACKERMANN, F. Digital image correlation: Performance and potential application in photogrammetry. **The Photogrammetric Record**. v. 11, n. 64, p. 429-439, 1984.

AGISOFT PHOTOSCAN, Available: < http://www.agisoft.com/ >. Access: May 10th, 2017.

ALONZO, M.; BOOKHAGEN, B.; ROBERTS, D. A. Urban tree species mapping using hyperspectral and LiDAR data fusion. **Remote Sensing of Environment**, v. 148, p. 70–83, 2014.

ASPRS, Web site. Available: <https://www.asprs.org/committee-general/laser-las-file-format-exchange-activities.html>. Access: Jan 19th, 2017.

AVBELJ, J.; IWASZCZUK, D.; MÜLLER, R.; REINARTZ, P.; STILLA, U. Coregistration refinement of hyperspectral images and DSM: An object-based approach using spectral information. **ISPRS Journal of Photogrammetry and Remote Sensing**, v. 100, p. 23–34, 2015.

BALTSAVIAS, E.; GRUEN, A.; EISENBEISS, H.; ZHANG, L.; WASER, L. T. High- quality image matching and automated generation of 3D tree models. **International Journal of Remote Sensing**, v. 29, n. 5, p. 1243–1259, 2008. doi.org/10.1080/01431160701736513.

BARBOSA, J. M.; MELENDEZ-PASTOR, I.; NAVARRO-PEDREÑO, J.; BITENCOURT, M. D. Remotely sensed biomass over steep slopes: An evaluation among successional stands of the Atlantic Forest, Brazil. **ISPRS Journal of Photogrammetry and Remote Sensing**, v. 88, p. 91–100, 2014.

BAY, H.; ESS, A.; TUYTELAARS, T.; VAN GOOL, L. Speeded-Up Robust Features (SURF). **Computer Vision and Image Understanding**, v. 110, n. 3, p. 346–359, 2008.

BERGEN, K. M.; GOETZ, S. J.; DUBAYAH, R. O.; HENEBRY, G. M.; HUNSAKER, C. T.; IMHOFF, M. L.; NELSON, R. F.; PARKER, G. G.; RADELOFF, V. C. Remote sensing of vegetation 3-D structure for biodiversity and habitat: Review and implications for LiDAR and radar spaceborne missions. **Journal of Geophysical Research: Biogeosciences**, v. 114, n. G2, 2009.

BERVEGLIERI, A.; TOMMASELLI, A. M. G.; IMAI, N. N.; RIBEIRO, E. A. W.; GUIMARÃES, R. B.; HONKAVAARA, E. Identification of Successional Stages and Cover Changes of Tropical Forest Based on Digital Surface Model Analysis. **IEEE**

Journal of Selected Topics in Applied Earth Observations and Remote Sensing, v. 9, n. 12, p. 5385–5397, 2016.

BETHMANN, F.; LUHMANN, T. Least-squares matching with advanced geometric transformation models. **Photogrammetrie-Fernerkundung-Geoinformation**, v. 2011, n. 2, p. 57–69, 2011.

BIRCHFIELD, S.; TOMASI, C. Depth Discontinuities by Pixel-to-Pixel Stereo. **International Journal of Computer Vision**, v. 35, n. 3, p. 269–293, 1999. <http://dx.doi.org/10.1023/A:1008160311296>.

BLEYER, M.; GELAUTZ, M. A layered stereo matching algorithm using image segmentation and global visibility constraints. **ISPRS Journal of Photogrammetry and Remote Sensing**, v. 59, n. 3, p. 128–150, 2005.

BROCKELBANK, D. C.; YANG, Y. H. An experimental investigation in the use of color in computational stereopsis. **IEEE Transactions on Systems, Man and Cybernetics**, v. 19, n. 6, p. 1365-1383, 1989.

BROWN, D. C. Close-Range Camera Calibration, **Photogrammetric Engineering**, v. 37, n. 8, p. 855–866, 1971.

BROWN, L. G. A Survey of Image Registration Techniques. **ACM Computing Surveys**, v. 24, p. 325–376, 1992.

BURKART, A.; AASEN, H.; ALONSO, L.; MENZ, G.; BARETH, G.; RASCHER, U. Angular Dependency of Hyperspectral Measurements over Wheat Characterized by a Novel UAV Based Goniometer. **Remote Sensing**, v. 7, n. 1, p. 725–746, 12 jan. 2015.

BÜTTNER, A.; RÖSER, H.-P. Hyperspectral Remote Sensing with the UAS Stuttgarter Adler–System Setup, Calibration and First Results. **Photogrammetrie-Fernerkundung-Geoinformation**, v. 2014, n. 4, p. 265–274, 2014.

CALONDER, M.; LEPETIT, V.; STRECHA, C.; FUA, P. Brief: Binary robust independent elementary features. **Computer Vision–ECCV** 2010, p. 778–792, 2010.

CARVALHO, O. A.; MENESES, P. R. Spectral correlation mapper (SCM): an improvement on the spectral angle mapper (SAM). In: Summaries of the 9th JPL Airborne Earth Science Workshop, **JPL Publication** 00-18. Pasadena, CA: JPL Publication, 2000.

CHAN, S.; WONG, Y.; DANIEL, J. Dense stereo correspondence based on recursive adaptive size multi-windowing. In:Image and Vision Computing, 2003, New Zealand. **Proceedings...**, New Zealand: IVC, 2003. v. 1. p. 256-260.

CHAMBON, S.; CROUZIL, A. Colour correlation-based matching. **International Journal of Robotics and Automation**, v. 20, n. 2, p. 78-85, 2005.

CLARKE, T.A., FRYER, J.G. The Development of Camera Calibration Methods and Models, **Photogrammetric Record**, v. 16, n. 91, . p. 51–66, 1998.

CLARK, M. L.; ROBERTS, D. A.; CLARK, D. B. Hyperspectral discrimination of tropical rain forest tree species at leaf to crown scales. **Remote sensing of environment**, v. 96, n. 3, p. 375–398, 2005.

CLARK, M. L.; ROBERTS, D. A.; EWEL, J. J.; CLARK, D. B. Estimation of tropical rain forest aboveground biomass with small-footprint lidar and hyperspectral sensors. **Remote Sensing of Environment**, v. 115, n. 11, p. 2931–2942, 2011.

CloudCompare. Available: < http://www.cloudcompare.org/doc/wiki/index.php?title=Distances_Computation> Access: May 8th, 2017.

COLOMINA, I.; MOLINA, P. Unmanned aerial systems for photogrammetry and remote sensing: A review. **ISPRS Journal of Photogrammetry and Remote Sensing**, v. 92, p. 79–97, 2014.

CRAMER, M.; STALLMANN, D. On the use of GPS/inertial exterior orientation parameters in Airborne Photogrammetry. In OEEPE-Workshop Integrated Sensor Orientation. **Proceedings…**2001.

CRAMER, M.; STALLMANN, D.; HAALA, N. Direct georeferencing using GPS/inertial exterior orientations for photogrammetric applications. In: International Archives of Photogrammetry and Remote Sensing, **Proceedings...**2000.

CUBERT. Available: < http://cubert-gmbh.com/> Access: Jan 9th, 2017.

DALPONTE, M.; BRUZZONE, L.; GIANELLE, D. Fusion of Hyperspectral and LIDAR Remote Sensing Data for Classification of Complex Forest Areas. **IEEE Transactions on Geoscience and Remote Sensing**, v. 46, n. 5, p. 1416–1427, 2008.

DORADO-MUNOZ, L. P.; VELEZ-REYES, M.; MUKHERJEE, A.; ROYSAM, B. A Vector SIFT Detector for Interest Point Detection in Hyperspectral Imagery. **IEEE Transactions on Geoscience and Remote Sensing**, v. 50, n. 11, p. 4521–4533, 2012.

EL-SHEIMY, N.; VALEO, C.; HABIB, A. **Digital terrain modeling: acquisition, manipulation, and applications.** Artech House, 2005. 257p.

ELTNER, A.; SCHNEIDER, D. Analysis of Different Methods for 3D Reconstruction of Natural Surfaces from Parallel-Axes UAV Images. **The Photogrammetric Record**, v. 30, n. 151, p. 279–299, 2015.

FOOKES, C.; MAEDER, A.; SRIDHARAN, S.; COOK, J. Multi-spectral stereo image matching using mutual information. In: 2nd International Symposium on 3D Data Processing, Visualization and Transmission, 2004. **Proceedings...** 2004.

FORSTNER, W. On the geometric precision of digital correlation. In ISPRS, 1982, Helsinki. **International Archives of Photogrammetry.** Helsinki: ISPRS, v. 24, n. 3, p. 176–189, 1982.

FRASER, C.S. Innovations in Automation for Vision Metrology Systems, **Photogrammetric Record**, v. 15, n. 90. p. 901–911, 1997a.

FRASER, C.S. Digital camera self-calibration, **ISPRS Journal of Photogrammetry and Remote Sensing**, v. 52, 149–159, 1997b.

FRASER, C.S. Automatic camera calibration in close range photogrammetry. **Photogrammetric Engineering and Remote Sensing**, v. 79, n. 4, p. 381–388, 2013.

FUSIELLO, A.; ROBERTO, V.; TRUCCO, E. Efficient Stereo with Multiple Windowing. In: Computer Vision and Pattern Recognition (CVPR '97), Washington, DC, USA: **Proceedings of the IEEE Computer Society**, 1997.

GRANSHAW, S.I. Bundle Adjustment Methods in Engineering Photogrammetry. **Photogrammetric Record**, v. 10, n. 56. p. 181–207, 1980.

GARRIDO-JURADO, S.; MUÑOZ-SALINAS, R., MADRID-CUEVAS, F. J., MARÍN-JIMÉNEZ, M. J., 2014. Automatic generation and detection of highly reliable fiducial markers under occlusion. **Pattern Recognition**, 2014, v. 47, n. 6. p. 2280–2292.

GEHRIG, S. K.; EBERLI, F.; MEYER, T. A Real-Time Low-Power Stereo Vision Engine Using Semi-Global Matching. (M. Fritz, B. Schiele, J. H. Piater, Eds.) In: Computer Vision Systems, **Proceedings...** Springer Berlin Heidelberg, 13 out. 2009.

GETZIN, S.; NUSKE, S. R.; WIEGAND, K. Using Unmanned Aerial Vehicles (UAV) to Quantify Spatial Gap Patterns in Forests**. Remote Sensing**, v. 6, n. 8, 2014.

GOETZ, A. F. H. Three decades of hyperspectral remote sensing of the Earth: A personal view. **Remote Sensing of Environment, Imaging Spectroscopy Special Issue**. v. 113, Supplement 1, p. S5–S16, set. 2009.

GOETZ, A. F. H.; VANE, G.; SOLOMON, J. E.; ROCK, B. N. Imaging Spectrometry for Earth Remote Sensing. **Science**, v. 228, n. 4704, p. 1147–1153, 1985.

GRUEN, A. Adaptive least squares correlation: a powerful image matching technique. **South African Journal of Photogrammetry, Remote Sensing and Cartography**, v. 14, n. 3, p. 175–187, 1985.

GRUEN, A. Development and Status of Image Matching in Photogrammetry. **The Photogrammetric Record**, v. 27, n. 137, p. 36–57, 2012. doi.org/10.1111/j.1477-9730.2011.00671.x.

GRUEN, A.; BALTSAVIAS, E. P. Geometrically constrained multiphoto matching. **Photogrammetric engineering and remote sensing**, v. 54, n. 5, p. 633–641, 1988.

GRUEN, A.; STALLMANN, D. High Accuracy Edge Matching with an Extension of the MPGC-Matching Algorithm. In: LINKWITZ, K.; EISELE, V.; MÖNICKE, H.-J. (Ed.). **Applications of Geodesy to Engineering. International Association of Geodesy Symposia**. Springer Berlin Heidelberg, 1993. p. 339–350.

GU, Z.; SU, X.; LIU, Y.; ZHANG, Q. Local stereo matching with adaptive support-weight, rank transform and disparity calibration. **Pattern Recognition Letters**, v. 29, n. 9, p. 1230–1235, 2008.

GUPTA, N., 2008. Hyperspectral imager development at Army research laboratory. **Proceeding of the SPIE Infrared Technology and Applications XXXIV**, 6940: 69401P–69401P. doi:10.1117/12.777110.

HAALA, N. Comeback of digital image matching. In: Photogrammetric Week 2009. **Proceedings...** 2009. p. 289-301.

HAALA, N. Multiray photogrammetry and dense image matching. In: Photogrammetric Week 2011. **Proceedings...** 2011. p. 185-195.

HAALA, N. The Landscape of Dense Image Matching Algorithms. In: Photogrammetric Week 2013. **Proceedings...** 2013.

HAALA, N.; ROTHERMEL, M. Dense Multi-Stereo Matching for High Quality Digital Elevation Models. **Photogrammetrie - Fernerkundung - Geoinformation**, v. 2012, n. 4, p. 331-343, 2012.

HABIB, A.; MORGAN, M., LEE, Y. Bundle Adjustment with Self–Calibration Using Straight Lines. **Photogrammetric Record**, v. 17, n. 100, p. 635–650, 2002.

HABIB, A; MORGAN M. Stability analysis and geometric calibration of off-the-shelf digital cameras. **Photogrammetric Engineering & Remote Sensing**, v. 71, n. 6, p. 733-41, 2005.

HABIB, A., PULLIVELLI, A.; MITISHITA, E.; GHANMA, M.; KIM, E. M. Stability analysis of low-cost digital cameras for aerial mapping using different georeferencing techniques. **Photogrammetric Record**, v. 21, n. 113, p. 29–43, 2006.

HABIB, A.; DETCHEV, I.; KWAK, E. Stability Analysis for a Multi-Camera Photogrammetric System. **Sensors**, v. 14, n. 8, p. 15084–15112, 2014.

HABOUDANE, D.; MILLER, J. R.; PATTEY, E.; ZARCO-TEJADA, P. J.; STRACHAN, I. B. Hyperspectral vegetation indices and novel algorithms for predicting green LAI of crop canopies: Modeling and validation in the context of precision agriculture. **Remote Sensing of Environment**, v. 90, n. 3, p. 337–352, 2004.

HAGGRÉN, H.; HEIKKILÄ, J. Calibration of Close-Range Photogrammetric Stations Using a Free Network Bundle Adjustment. **The Photogrammetric Journal of Finland**, v. 11, n. 2, p. 21–31, 1989.

HAJJDIAB, H.; GHAZAL, M.; FAROK, H.; HOWARI, F. Multispectral Image Matching Technique. **International Journal of Applied Physics and Mathematics**. v. 2, n. 5, p. 388-391, 2012.

HAKALA, T.; NEVALAINEN, O.; KAASALAINEN, S.; MÄKIPÄÄ, R. Multispectral LiDAR time series of pine canopy chlorophyll content. **Biogeosciences**, v. 12, P. 1629-1634, 2015. https://dx.doi.org/10.5194/bg-12-1629-2015.

HARRIS, C.; STEPHENS, M. A combined corner and edge detector. In: In Proc. of Fourth Alvey Vision Conference, **Proceedings...**1988.

HARTLEY, R. I. Theory and Practice of Projective Rectification. **International Journal of Computer Vision**, v. 35, n. 2, p. 115–127, 1999. doi.org/10.1023/A:1008115206617.

HATTORI, S., AKIMOTO, K., FRASER, C., IMOTO, H., 2002. Automated Procedures with Coded Targets in Industrial Vision Metrology. **Photogrammetric Engineering and Remote Sensing**, 2002, v. 68, n. 5, p. 441–446.

HEADWALL. Available: <http://www.headwallphotonics.com/spectral-imaging/hyperspectral/nano-hyperspec> Access: Jan 9th, 2017.

HEIKKILÄ, J. Geometric Camera Calibration Using Circular Control Points. **IEEE Transactions on Pattern Analysis and Machine Intelligence**, 2000, v. 22, n. 10, p. 1066–1077.

HIRSCHMÜLLER, H.; BUDER, M.; ERNST, I. Memory efficient semi-global matching. **ISPRS Annals of the Photogrammetry, Remote Sensing and Spatial Information Sciences**, 2012. n. 3, p. 371–376.

HIRSCHMÜLLER, H. Accurate and efficient stereo processing by semi-global matching and mutual information. In: 2005 IEEE Computer Society Conference on Computer Vision and Pattern Recognition (CVPR'05), **Proceedings...** CVPR'05. 2005.

HIRSCHMÜLLER, H. Stereo Processing by Semiglobal Matching and Mutual Information. **IEEE Transactions on Pattern Analysis and Machine Intelligence**, v. 30, n. 2, p. 328–341, 2008.

HONKAVAARA, E.; ESKELINEN, M. A.; PÖLÖNEN, I.; SAARI, H.; OJANEN, H.; MANNILA, R.; HOLMLUND, C.; HAKALA, T.; LITKEY, P.; ROSNELL, T.; VILJANEN, N.; PULKKANEN, M. Remote Sensing of 3-D Geometry and Surface Moisture of a Peat Production Area Using Hyperspectral Frame Cameras in Visible to Short-Wave Infrared Spectral Ranges Onboard a Small Unmanned Airborne Vehicle (UAV). **IEEE Transactions on Geoscience and Remote Sensing**, v. 54, n. 9, p. 5440–5454, set. 2016.

HONKAVAARA, E.; KAIVOSOJA, J.; MÄKYNEN, J.; PELLIKKA, I.; PESONEN, L.; SAARI, H.; SALO, H.; HAKALA, T.; MARKLELIN, L.; ROSNELL, T. Hyperspectral reflectance signatures and point clouds for precision agriculture by light weight UAV imaging system. **ISPRS Annals of Photogrammetry, Remote Sensing and Spatial Information Sciences**, v. I-7, p. 353–358, 2012.

HONKAVAARA, E.; MARKELIN, L.; ROSNELL, T.; NURMINEN, K. Influence of solar elevation in radiometric and geometric performance of multispectral photogrammetry. **ISPRS Journal of Photogrammetry and Remote Sensing**, v. 67, p. 13-26, 2012b.

HONKAVAARA, E.; SAARI, H.; KAIVOSOJA, J.; PÖLÖNEN, I.; HAKALA, T.; LITKEY, P.; MÄKYNEN, J.; PESONEN, L. Processing and Assessment of Spectrometric, Stereoscopic Imagery Collected Using a Lightweight UAV Spectral Camera for Precision Agriculture. **Remote Sensing**, v. 5, n. 10, p. 5006–5039, 2013.

HONKAVAARA, E.; ROSNELL, T.; OLIVEIRA, R.A; TOMMASELLI, A.M.G. Band registration of tuneable frame format hyperspectral UAV imagers in complex scenes. **ISPRS Journal of Photogrammetry and Remote Sensing**, 2017.

HYYPPÄ, J.; HYYPPÄ, H.; LECKIE, D.; GOUGEON, F.; YU, X.; MALTAMO, M. Review of methods of small- footprint airborne laser scanning for extracting forest inventory data in boreal forests. **International Journal of Remote Sensing**, v. 29, n. 5, p. 1339–1366, mar. 2008. doi.org/10.1080/01431160701736489.

HYYPPÄ, J.; YU, X.; HYYPPÄ, H.; VASTARANTA, M.; HOLOPAINEN, M.; KUKKO, A.; KAARTINEN, H.; JAAKKOLA, A.; VAAJA, M.; KOSKINEN, J.; ALHO, P. Advances in forest inventory using airborne laser scanning. **Remote Sensing**, v. 4, p. 1190–1207, 2012.

IMEC. Available: < https://www.imec-int.com> Access: Jan 9th, 2017.

JACQUEMOUD, S.; BARET, F.; ANDRIEU, B.; DANSON, F.; JAGGARD, K. Extraction of vegetation biophysical parameters by inversion of the PROSPECT+ SAIL models on sugar beet canopy reflectance data. Application to TM and AVIRIS sensors. **Remote sensing of environment**, v. 52, n. 3, p. 163–172, 1995.

JENSEN, J. R. **Sensoriamento remoto do ambiente: uma perspectiva em recursos terrestres.** Tradução da 2 ed. por (pesquisadores do INPE): José Carlos N. Epiphanio (coordenador); Antonio R. Formaggio; Athos R. Santos; Bernardo F. T. Rudorff; Cláudia M. Almeida; Lênio S. Galvão. São José dos Campos: Parêntese. 2009. 672 p.

JENSEN, J. R.; SCHILL, S. R. Bidirectional Reflectance Distribution Function (BRDF) Characteristics of Smooth Cordgrass (Spartina alterniflora) Obtained Using a Sandmeier Field Goniometer. **Geocarto International**, v. 15, n. 2, p. 23–30, 2000. doi/abs/10.1080/10106049908542149.

KANADE, T.; OKUTOMI, M. A stereo matching algorithm with an adaptive window: Theory and experiments. In: IEEE Internarional Conference on Robotics and Automation, 1991, California. **Proceedings…** ICRA: California, 1991. p. 1088-1095.

KANKARE, V.; HOLOPAINEN, M; VASTARANTA, M.; PUTTONEN, E.; YU, X.; HYYPPÄ, J.; VAAJA, M.; HYYPPÄ, H.; ALHO, P. Individual tree biomass estimation using terrestrial laser scanning. **ISPRS Journal of Photogrammetry and Remote Sensing**, v. 75, p. 64-75, 2013.

KE, Y.; SUKTHANKAR, R. PCA-SIFT: a more distinctive representation for local image descriptors. In: IEEE Computer Society Conference on Computer Vision and Pattern Recognition, 2004. **Proceedings of the CVPR** 2004.

KENEFICK, J. F., GYER, M. S., HARP, B. F., 1972. Analytical Self-Calibration. **Photogrammetric Engineering**, 38, 1117–1126.

KOCH, B. Status and future of laser scanning, synthetic aperture radar and hyperspectral remote sensing data for forest biomass assessment. **ISPRS Centenary Celebration Issue**, v. 65, n. 6, p. 581–590, Nov. 2010.

KORPELA, I.; HEIKKINEN, V.; HONKAVAARA, E.; ROHRBACH, F.; TOKOLA, T. Variation and directional anisotropy of reflectance at the crown scale - Implications for tree species classification in digital aerial images. **Remote Sensing of Environment**, v. 115, n. 8, p. 2062-2074, 2011.

KOSCHAN, A. Dense Stereo Correspondence Using Polychromatic Block Matching. In: Proc. of the 5th Int. Conf. on Computer Analysis of Images and Patterns CAIP'93, **Proceedings...**1993.

KOUKOULAS, S.; BLACKBURN, G. A.. Quantifying the spatial properties of forest canopy gaps using LiDAR imagery and GIS. International Journal of Remote Sensing, v. 25, n. 15, p.3049-3072, 2004

KRAUS, K. **Photogrammetry:** geometry from images and laser scans. Walter de Gruyter, 2007.

KRUSE, F. A.; LEFKOFF, A. B.; BOARDMAN, J. B.; HEIDEBRECHT, K. B.; SHAPIRO, A. T.; BARLOON, P. J.; GOETZ, A. F. H. The Spectral Image Processing System (SIPS) – Interactive Visualization and Analysis of Imaging Spectrometer Data: **Remote Sensing of Environment**, Special issue on AVIRIS, 1993, v. 44, p. 145 - 163.

LAPRAY, P. J., WANG, X., THOMAS, J. B., GOUTON, P., 2014. Multispectral filter arrays: Recent advances and practical implementation. **Sensors**, 14(11): 21626–21659.

LASTools. Available <https://rapidlasso.com/lastools/>. Access: Jan. 19th, 2017.

LEE, D.; YOM, J.; SHIN, S. W.; OH, J.; PARK, K. Automatic Building Reconstruction withSatellite Images and Digital Maps. **ETRI Journal**, v. 33. n. 4. p. 537-546, dez. 2011.

LEUTENEGGER, S.; CHLI, M.; SIEGWART, R. Y. BRISK: Binary Robust invariant scalable keypoints. In: 2011 International Conference on Computer Vision, **Proceedings...**2011.

LI, Z.; ZHU, Q.; GOLD, C. **Digital terrain modeling:** principles and methodology. CRC Press, 2005. 323p.

LOWE, D. G. Object recognition from local scale-invariant features. In: IEEE International Conference on Computer Vision, 1999, **Proceedings...** 1999.

LOWE, D. G. Distinctive Image Features from Scale-Invariant Keypoints. **International Journal of Computer Vision**, v. 60, n. 2, p. 91–110, 1 nov. 2004.

MA, W.; WEN, Z.; WU, Y.; JIAO, L.; GONG, M.; ZHENG, Y.; LIU, L. Remote Sensing Image Registration With Modified SIFT and Enhanced Feature Matching. **IEEE Geoscience and Remote Sensing Letters**, v. 14, n. 1, p. 3–7, jan. 2017.

MAAS, H.-G. Automatic DEM generation by multi-image feature based matching. In: International Archives of Photogrammetry and Remote Sensing, Viena. **Proceedings...** Viena: 1996.

MÄKYNEN, J.; HOLMLUND, C.; SAARI, H.; OJALA, K.; ANTILA, T. Unmanned aerial vehicle (UAV) operated megapixel spectral camera. In: Electro-Optical Remote Sensing, Photonic Technologies, and Applications. **Proceedings SPIE**, 2011. v. 8186. p. 81860Y-1-81860Y-9.

MATIKAINEN, L.; KARILA, K.; HYYPPÄ, J.; LITKEY, P.; PUTTONEN, E.; AHOKAS, E. Object-based analysis of multispectral airborne laser scanner data for land cover classification and map updating. **ISPRS Journal of Photogrammetry and Remote Sensing**, v. 128, p. 298-313, 2017. https://dx.doi.org/10.1016/j.isprsjprs.2017.04.005.

MENESES, P.R., ALMEIDA, T. de. **Introdução ao Processamento de Imagens de Sensoriamento Remoto**. 1 ed. Brasília: UnB/CNPq, v.1, 2012.

MERCHANT, D. C. Analytical Photogrammetry: Theory and Practice. Notes Revised from Earlier Edition Printed in 1973, Ohio State University: Columbus, USA., 1976.

MIKHAIL, E. M., BETHEL, J. S. MCGLONE, J. C. **Introduction to Modern Photogrammetry.** Inc. New York: John Wiley & Sons, 2001, 479p.

MIKOLAJCZYK, K.; SCHMID, C. A performance evaluation of local descriptors. **IEEE Transactions on Pattern Analysis and Machine Intelligence**, v. 27, n. 10, p. 1615–1630, out. 2005.

MONTESINOS, P. et al. Matching color uncalibrated images using differential invariants. **Image and Vision Computing**, v. 18, n. 9, p. 659-671, 2000.

MUHLMANN, K.; MAIER, D.; HESSER, J.; MÄNNER, R. Calculating dense disparity maps from color stereo images, an efficient implementation. In: IEEE Workshop on Stereo and Multi-Baseline Vision, 2001, Washington, USA. **Proceedings...** Washington: SMBV, 2001. p. 30-36.

MUKHERJEE, A.; VELEZ-REYES, M.; ROYSAM, B. Interest points for hyperspectral image data. **IEEE Transactions on Geoscience and Remote Sensing**, v. 47, n. 3, p. 748-760, 2009.

NAESSET, E. Determination of mean tree height of forest stands using airborne laser scanner data. **ISPRS Journal of Photogrammetry and Remote Sensing**, v. 52, n. 2, pp. 49-56, 1997.

NÄSI, R.; HONKAVAARA, E.; LYYTIKÄINEN-SAARENMAA, P.; BLOMQVIST, M.; LITKEY, P.; HAKALA, T.; VILJANEN, N.; KANTOLA, T.; TANHUANPÄÄ, T.; HOLOPAINEN, M. Using UAV-Based Photogrammetry and Hyperspectral Imaging for Mapping Bark Beetle Damage at Tree-Level. **Remote Sensing**, v. 7, n. 11, p. 15467–15493, 18 nov. 2015.

NEVALAINEN, O.; HAKALA, T.; SUOMALAINEN, J.; MÄKIPÄÄ, R.; PELTONIEMI, M.; KROOKS, A.; KAASALAINEN, S. Fast and nondestructive method for leaf level chlorophyll estimation using hyperspectral LiDAR**. Agricultural and forest meteorology**, v. 198, p. 250-258, 2014.

NEVALAINEN, O.; HONKAVAARA, E.; TUOMINEN, S.; VILJANEN, N.; HAKALA, T.; YU, X.; HYYPPÄ, J.; SAARI, H.; PÖLÖNEN, I.; IMAI, N. N.; TOMMASELLI, M. A. Individual Tree Detection and Classification with UAV-Based Photogrammetric Point Clouds and Hyperspectral Imaging. **Remote Sensing**, v. 9, n. 3, 2017.

OLIVEIRA, R. A.; BERVEGLIERI, A.; TOMMASELLI, A. M.; HONKAVAARA, E. Potential of dense matching for DSM generation in tropical forests using UAV images. In: ISPRS Geospatial Week 2015, La Grande Motte, France. **Proceedings**...2015.

OLIVEIRA, R. A. Geração de Modelos Digital de Superfície utilizando múltiplas imagens. 2013a. 133f. Dissertação (Mestrado em Ciências Cartográficas) - Faculdade de Ciências e Tecnologia, Universidade Estadual Paulista, Presidente Prudente.

OLIVEIRA, R. A.; TOMMASELLI, A. M. G. Assessment of digital surface model generated with multi-image. In: Latin American Remote Sensing Week, 2013, Santiago. Latin American Remote Sensing Week, 2013b.

OLIVEIRA, R. A.; TOMMASELLI, A. M. G. Avaliação de uma técnica para geração de modelos digitais de superfície utilizando múltiplas imagens. **Boletim de Ciências Geodésicas** (Online), v. 20, p. 257-278, 2014a.

OLIVEIRA, R. A.; TOMMASELLI, A. M. G.; HONKAVAARA, E.; HYYPPA, J.; IMAI, N. N.; HAKALA, T.; JAAKKOLA, A. Avaliação do corregistro de imagens coletadas por uma câmara hiperespectral de quadro. In: XXVI Congresso Brasileiro de Cartografia V Congresso Brasileiro de Geoprocessamento XXV Exposicarta, 2014, Gramado. **Proceedings of XXVI CBC**, 2014b.

OLIVEIRA, R. A.; TOMMASELLI, A. M. G.; HONKAVAARA, E. Using Hyperspectral Frame Images from Unmanned Airborne Vehicle for Detailed Measurement of Boreal Forest 3D Structure. IOP Conference Series: Earth and Environmental Science, v. 44, n. 4, p. 042029, 2016a. Available on: <http://stacks.iop.org/1755-1315/44/i=4/a=042029>.

OLIVEIRA, R. A.; TOMMASELLI, A. M. G.; HONKAVAARA, E. Geometric calibration of a hyperspectral frame camera. **The Photogrammetric Record**, v. 31, n. 4, p. 325, 347, 2016b.

PAPARODITIS, N.; POLIDORI, L. DSM quality: internal and external validation. In: EGELS, Y.; KASSER, M. Digital Photogrammetry. 1. ed. New York: Taylor & Francis, 2002. 351p.

PEDUZZI, A.; WYNNE, R.H.; THOMAS, V.A.; NELSON, R.F.; REIS, J.J.; SANFORD, M. Combined use of airborne lidar and DBInSAR data to estimate LAI in temperate mixed forests. **Remote Sensing**, v. 4, p. 1758–1780, 2012.

PERSSON, H; WALLERMAN, J.; OLSSON, H. ; FRANSSON, J.E.S. Estimating biomass and height using DSM from satellite data and DEM from high-resolution laser scanning data. In: IEEE International Geoscience and Remote Sensing Symposium, 2012, Munich. **Proceedings…** Munich: IGARSS, 2012. p. 1649-1651.

PIERROT-DESEILLIGNY, M.; PAPARODITIS, N. A multiresolution and optimization-based image matching approach: An application to surface reconstruction from spot5-hrs stereo imagery. In: ISPRS Conference Topographic Mapping From Space (With Special Emphasis on Small Satellites). **Proceedings of the ISPRS**, 2006.

PINTO, F.; MÜLLER-LINOW, M.; SCHICKLING, A.; CENDRERO-MATEO, P. M.; BALLVORA, A.; RASCHER, U. Multiangular Observation of Canopy Sun-Induced Chlorophyll Fluorescence by Combining Imaging Spectroscopy and Stereoscopy. **Remote Sensing**, v. 9, n. 5, 2017.

POLI, D. A rigorous model for spaceborne linear array sensors. **Photogrammetric Engineering & Remote Sensing**, v. 73, n. 2, p. 187–196, 2007.

POLIDORIO, A. M.; IMAI, N. N.; TOMMASELLI, A. M. G.; FLORES, F. C.; FRANCO, C. Realce do grau de artificialidade de feições em imagens aéreas coloridas. Curitiba, CPGCG/UFPR: **Série em Ciências Geodésicas**, v. 3, p. 277–291, 2003.

RABUS, B.; MICHAEL, E.; ACHIM, R.; RICHARD, B. The shuttle radar topography mission – a new class of digital elevation models acquired by spaceborne radar. **ISPRS journal of photogrammetry and remote sensing**, v. 57, n. 4, pp. 241-262, 2003.

REMONDINO, F.; EL-HAKIM, S. Image-Based 3D Modelling: A Review. The **Photogrammetric Record**, v. 21, n. 115, p. 269–291, 2006. doi:10.1111/j.1477-9730.2006.00383.x/abstract.

REMONDINO, F.; SPERA, M. G.; NOCERINO, E.; MENNA, F.; NEX, F. State of the Art in High Density Image Matching. **The Photogrammetric Record**, v. 29, n. 146, p. 144–166, 2014. doi: 10.1111/phor.12063/abstract.

RICHARDS, J. A.; JIA, X. **Remote sensing digital image analysis** - An Introdution. Berlin et al.: Springer, 2006. ed. 4, 439p.

RIKOLA. Available: <http://senop.fi/en/optronics-hyperspectral> Access: May 9th, 2017.

ROOSJEN, P. P.; SUOMALAINEN, M. J.; BARTHOLOMEUS, M. H.; KOOISTRA, L.; CLEVERS, G. J. Mapping Reflectance Anisotropy of a Potato Canopy Using Aerial Images Acquired with an Unmanned Aerial Vehicle**. Remote Sensing**, v. 9, n. 5, 2017.

RUBLEE, E.; RABAUD, V.; KONOLIGE, K.; BRADSKI, G. ORB: An efficient alternative to SIFT or SURF. In: 2011 International Conference on Computer Vision, **Proceedings...**,2011.

RUY, R. da S.; TOMMASELLI, A. M. G.; GALO, M.; HASEGAWA, J. K.; REIS, T. T. Evaluation of Bundle Block Adjustment with Additional Parameters Using Images Acquired by SAAPI System. In: 6th International Symposium on Mobile Mapping Technology. **Proceedings of the 6th ISMMT**. Presidente Prudente: UNESP, 2009.

SAARI, H.; AALLOS, V.-V.; AKUJÄRVI, A.; ANTILA, T.; HOLMLUND, C.; KANTOJÄRVI, U.; MÄKYNEN, J.; OLLILA, J. Novel miniaturized hyperspectral sensor for UAV and space applications. **Proceedings...,** 2009. doi.org/10.1117/12.830284.

SADEGHI, Y.; ST-ONGE, B.; LEBLON, B.; SIMARD, M. Canopy height model (CHM) derived from a TanDEM-X InSAR DSM and an airborne Lidar DTM in boreal forest. **IEEE Journal of Selected Topics in Applied Earth Observations and Remote Sensing**, v. 9, n. 1, pp.381-397, 2016. doi.org/10.1109/JSTARS.2015.2512230.

SCHAEPMAN, M. E. **Imaging spectrometers.** In: Warner, T.A.; Duane Nellis, M.; Foody, G. (Eds). The SAGE Handbook of Remote Sensing, London: SAGE, 2009. p. 166-178

SCHARSTEIN, D.; SZELISKI, R. A Taxonomy and Evaluation of Dense Two-Frame Stereo Correspondence Algorithms. **International Journal of Computer Vision**, v. 47, n. 1, p. 7–42, 2002. doi.org/10.1023/A:1014573219977>.

SCHENK, T. **Digital Photogrammetry**. Ohio: Terra Science, 1999. v. 1, 428 p.

SCHOWENGERDT, R. A. **Remote Sensing:** Models and Methods for Image Processing. Academic Press, 2006. 3. ed. 560p.

SEITZ, S. M.; CURLESS, B.; DIEBEL, J.; SCHARSTEIN, D.; SZELISKI, R. A Comparison and Evaluation of Multi-View Stereo Reconstruction Algorithms. In: Proceedings of the 2006 IEEE Computer Society Conference on Computer Vision and Pattern Recognition - Volume 1, Washington, DC, USA**. Proceedings...** Washington, DC, USA: IEEE Computer Society, 2006. doi.org/10.1109/CVPR.2006.19.

SHAW, G. A.; BURKE, H. K. Spectral imaging for remote sensing. **Lincoln Laboratory Journal**, v. 14, n. 1, p. 3–28, 2003.

SHORTIS, M.R., SEAGER, J.W., ROBSON, S., HARVEY, E.S., 2003. Automatic Recognition of Coded Targets Based on a Hough Transform and Segment Matching, **Proceedings of SPIE Videometrics VII**, 5013, 7 pages.

SILVA, P. H. A.; TOMMASELLI, A. M. G.; GALO, M.; COSTA, E. Um estudo sobre o uso do modelo de cor RGB no processo de correspondência por correlação. **Boletim de Ciências Geodésicas**, v.13, n.1, 2007.

SILVA, S. L. A.; TOMMASELLI, A. M. G; ARTERO, A. O. Utilização de alvos codificados do tipo aruco na automação do processo de calibração de câmaras. **Boletim de Ciências Geodésicas** (Online), v. 20, p. 626-646, 2014.

SIMA, A. A., BUCKLEY, S. J., KURZ, T. H., SCHNEIDER, D., 2014. Semi- Automated Registration Of Close- Range Hyperspectral Scans Using Oriented Digital Camera Imagery And A 3D Model. **Photogrammetric Record**, v. 29, n.145. p. 10–29.

SUOMALAINEN, J.; ANDERS, N.; IQBAL, S.; ROERINK, G.; FRANKE, J.; WENTING, P.; HÜNNIGER, D.; BARTHOLOMEUS, H.; BECKER, R.; KOOISTRA, L. A lightweight hyperspectral mapping system and photogrammetric processing chain for unmanned aerial vehicles. **Remote Sensing**, v. 6, n. 11, p. 11013–11030, 2014.

SZELISKI, R. **Computer Vision:** Algorithms and Applications. Springer, 2010.

TAO, H.; SAWHNEY, H. S. Global matching criterion and color segmentation based stereo. In: 5th IEEE Workshop on Applications of Computer Vision, 2000. **Proceedings...** 2000.

TOMMASELLI, A. M. G.; HASEGAWA, J. K.; GALO, M. Desenvolvimento de uma biblioteca de funções e classes para Fotogrametria. In: Congresso Brasileiro de Cartografia, 21, 2003, Belo Horizonte. **Proceedings of** XXI Congresso Brasileiro de Cartografia, 2003.

TOMMASELLI, A. M.; MEDEIROS, N. G. Determination of the indirect orientation of orbital pushbroom images using control straight lines. **The Photogrammetric Record**, v. 25, n. 130, p. 159–179, 2010.

TOMMASELLI, A.M.G., GALO, M., DE MORAES, M.V.A., MARCATO, J., CALDEIRA, C.R.T., LOPES, R.F. Generating Virtual Images from Oblique Frames. **Remote Sensing**, 2013, v. 5, n, 4, p. 1875–1893.

TOMMASELLI, A. M., OLIVEIRA, R. A., NAGAI, L. Y., IMAI, N. N., MIYOSHI, G. T., HONKAVAARA, E. and HAKALA, T. Assessment of bands coregistration of a light-weight spectral frame camera for UAV. In: ISPRS Geospatial Week 2015, La Grande Motte, France. **Proceedings...**2015.

VAKALOPOULOU, M.; KARANTZALOS, K. Automatic Descriptor-Based Co-Registration of Frame Hyperspectral Data. **Remote Sensing**, v. 6, n. 4, p. 3409–3426, 2014.

VANE, G.; GREEN, R. O.; CHRIEN, T. G.; ENMARK, H. T.; HANSEN, E. G.; PORTER, W. M. The airborne visible/infrared imaging spectrometer (AVIRIS). **Airbone Imaging Spectrometry**, v. 44, n. 2, p. 127–143, 1993.

VOSSELMAN, G.; SESTER, M.; MAYER, H. Basic computer vision techniques. In: **Manual of Photogrammetry**. 5. Ed. Falls Church, USA: ASP, 2004. p. 455-504.

VAUHKONEN, J.; HOLOPAINEN, M.; KANKARE, V.; VASTARANTA, M.; VIITALA, R. Geometrically explicit description of forest canopy based on 3D triangulations of airborne laser scanning data. **Remote Sensing of Environment**, v. 173, p. 248-257, 2016.

WEI, G.; SHALEI, S.; BO, Z.; SHUO, S.; FAQUAN, L.; XUEWU, C. Multi-wavelength canopy LiDAR for remote sensing of vegetation: Design and system performance. **ISPRS Journal of Photogrammetry and Remote Sensing**, v. 69, p. 1-9, 2012.

WENZEL, K.; ROTHERMEL, M.; FRITSCH, D.; HAALA, N. Image acquisition and model selection for multi-view stereo. **Int. Arch. Photogramm. Remote Sens. Spatial Inf. Sci**, v. 40, p. 251-258, 2013.

ZHANG, L. **Automatic Digital Surface Model (DSM) Generation from Linear Array Images**. 2005. Ph. D. Dissertation, n. 88, Institute of Geodesy and Photogrammetry, ETH Zurich, Switzerland. Available: <http://e-collection.library.ethz.ch/view/eth:28126>. Access: Jul 10th, 2014.

ZHANG, Y.; ZHANG, Y.; MO, D.; ZHANG, Y.; LI, X. Direct Digital Surface Model Generation by Semi-Global Vertical Line Locus Matching. **Remote Sensing**, v. 9, n. 3, 2017.

ZHENG, H.; ZHOU, X.; CHENG, T.; YAO, X.; TIAN, Y.; CAO, W.; ZHU, Y. Evaluation of a UAV-based hyperspectral frame camera for monitoring the leaf nitrogen concentration in rice. In: 2016 IEEE International Geoscience and Remote Sensing Symposium (IGARSS), **Proceedings of IGARSS**, 2016.

ZITOVÁ, B.; FLUSSER, J. Image registration methods: a survey. **Image and Vision Computing**, v. 21, n. 11, p. 977–1000, 2003.